UNIVERSITY OF CALIFORNIA,
IRVINE

Measuring protein secretion from single cells at single molecule resolution using quantum dots and imaging

DISSERTATION

submitted in partial satisfaction of the requirements
for the degree of

DOCTOR OF PHILOSOPHY

in Biomedical Engineering

by

Vanessa Herrera

Dissertation Committee:
Assistant Professor Jered B. Haun, Chair
Associate Professor Wendy F. Liu
Assistant Professor Michelle Digman

2019

DEDICATION

To

My family for their unconditional support, advice, and love.

Para mis papas:
Gracias por apoyarme en todo lo que hago, por estar siempre para mi y conmigo en cada etapa de mi vida. Gracias por darme consejo, motivación y, sobre todo, amor incondicional. Sin ustedes, ninguno de mis logros hubiera sido posible.

Para mi hermana:
Gracias por hacerme reír como nadie más puede hacerlo, por ayudarme en cualquier cosa que te pido y por estar siempre presente en mi vida.

My soon-to-be husband for being always there for me.

Thank you for your encouragement, patience, support, guidance, and love; for motivating and helping me every step of the way. Gracias por ser quién eres y por hacerme la mujer más feliz del mundo.

My friends for making my graduate experience one of the most exciting times of my life.

TABLE OF CONTENTS

LIST OF FIGURES

LIST OF EQUATIONS

LIST OF TABLES

ACKNOWLEDGMENTS

I would like to express the deepest appreciation to my advisor and committee chair, Dr. Jered B. Haun for all his guidance and mentorship in every step of my research. Your endless help and support throughout my graduate work has made me a better researcher. Thank you for your motivation, patience, and encouragement for all these years.

I would like to thank my committee members, Dr. Wendy F. Liu and Dr. Michelle Digman for providing me with their insight and expertise on my projects. I am grateful to all their advice and guidance.

My sincerest gratitude to all members of the Haun lab, past and present. I would like to specially thank Maha Rahim for mentoring me from the beginning to the end, for her advice, help, and friendship. I would also like to thank Xiaolong Qiu, Jeremy Lombardo, Hinesh Patel, and Louis Mejia for their help at various stages of my work; and my undergraduate students Lisa Nguyen and Carol Chen.

Special thanks to Joseph Hsu from the Wendy lab for his invaluable help in performing single cell experiments.

I would like to acknowledge the Royal Society of Chemistry for providing me with permissions to include copyrighted materials as part of my dissertation.

Lastly, I would like to extend my gratitude to the Center for Advanced Design & Manufacturing of Integrated Microfluidics (CADMIM), NSF Graduate Research Fellowship Program, and the University of California, Irvine for their funding support.

CURRICULUM VITAE

Vanessa Herrera

Ph.D. in Biomedical Engineering **2019**
University of California, Irvine

M.S. in Biomedical Engineering **2016**
University of California, Irvine

B.S. in Bioengineering: Biotechnology **2013**
University of California, San Diego

JOURNAL PUBLICATIONS

Herrera, V., Hsu, J., Rahim, M.K., Chen, C., Nguyen, L., Liu, W.F., Haun, J.B. Pushing the limits of detection for proteins secreted from single cells using quantum dots. *Analyst*. **2019**

Mendez, N., **Herrera, V.,** Trogler, W., Kummel, A. Encapsulation of adenovirus serotype 5 in anionic lecithin liposomes using a bead-based immunoprecipitation technique enhances transfection efficiency. *Biomaterials*. **2014,** *35 (35),* 9554-61.

PODIUM PRESENTATIONS

2018 Biomedical Engineering Society Annual Meeting, **V. Herrera**, J. Hsu, M. Rahim, W. Liu, J. Haun, "Measuring protein secretion from single cells at single molecule resolution using quantum dots," Podium Presentation, Atlanta, GA, October 2018

2018 NanoEngineering in Biology and Medicine (NEMB) Conference, **V. Herrera**, J. Hsu, M. Rahim, W. Liu, J. Haun, "Measuring protein secretion from single cells at single molecule resolution using quantum dots," Podium Presentation, Los Angeles, CA, July 2018

2018 UC Systemwide Bioengineering Symposium, **V. Herrera**, J. Hsu, M. Rahim, W. Liu, J. Haun, "Measuring protein secretion from single cells at single molecule resolution using quantum dots," Podium Presentation, Riverside, CA, June 2018

2017 UC Systemwide Bioengineering Symposium, **V. Herrera**, J. Hsu, M. Rahim, W. Liu, J. Haun, "Ultrasensitive Detection of Secreted Proteins from Single Cells Using

Quantum Dots," Podium Presentation, Los Angeles, CA, July 2017

2016 BMES Annual Meeting, **V. Herrera**, T. Luu, M. Rahim, F. McWhorter, W. Liu, J. Haun "Ultrasensitive Detection of Secreted Proteins from Single Cells Using Chemically-Amplified Quantum Dots," Podium Presentation, Minneapolis, MN, October 2016

SELECTED POSTER PRESENTATIONS

2017 Biomedical Engineering Society Annual Meeting, **V. Herrera**, J. Hsu, M. Rahim, W. Liu, J. Haun, "Ultrasensitive Detection of Secreted Proteins from Single Cells Using Quantum Dots," Poster Presentation, Phoenix, AZ, October 2018

2015 Biomedical Engineering Society Annual Meeting, **V. Herrera**, J. Hsu, M. Rahim, W. Liu, J. Haun, "Ultrasensitive Detection of Secreted Proteins from Single Cells Using Quantum Dots," Poster Presentation, Tampa, FL, October 2015

ABSTRACT OF THE DISSERTATION

Measuring protein secretion from single cells at single molecule resolution using quantum dots and imaging

By

Vanessa Herrera

Doctor of Philosophy in Biomedical Engineering

University of California, Irvine, 2019

Professor Jered B. Haun, Chair

Single cell analysis methods are becoming increasingly important since understanding how individual cells process information and respond to stimuli could lead to greater insight into cell heterogeneity. Soluble proteins play a critical role in controlling cell population behavior, but directly monitoring cell secretion is technically challenging. The goal of this work is to develop an extremely sensitive detection platform with multiplexing capabilities to quantify secreted proteins from single cells.

Single cell microarrays have been developed that assess protein secretion from isolated single cells, but this platform is currently limited by low detection sensitivity in the ng/ml range (~60 pM) for most proteins. Thus, increasing detection sensitivity would significantly improve this analysis technique by enabling interrogation at earlier time points or in response to more subtle activation factors. Nanomaterial probes have been shown to provide remarkable detection capabilities in cell-based detection applications;

especially luminescent quantum dots (QD), with their bright and photostable signals. In this work, we used QD in a sandwich immunoassay to detect secreted soluble cytokines at the single cell level.

Using the QD-based detection method, the detection sensitivity was improved to 60 aM; 10^6-fold more sensitive compared to immunofluorescence detection. In single cell experiments, the QD-based platform increased the number of single cells that could be interrogated for TNF-α protein by 3-fold relative to a traditional organic fluorophore, improving detection threshold from 30 pM or 10,000 TNF-α molecules down to only 5 fM or 2 molecules. Furthermore, multiplexing capabilities were adapted to the QD-based platform by using different colored QD to evaluate simultaneous protein secretion of up to 4 proteins (TNF-α, MCP-1, IL-10, and TGF-β). In single cell experiments, we were able to determine and quantify the type of proteins secreted from each single cell, and consequently, classify the cells as expressing pro-inflammatory or pro-healing characteristics. Additionally, the phasor approach to fluorescence lifetime imaging microscopy (FLIM) was used to assess and correct QD homoquenching.

CHAPTER 1: Introduction

1.1 Macrophage polarization

Macrophages are phagocytic cells that originate from stem cells in the hematopoietic system. In the embryonic development, the first active tissue-specific phagocytic cells are formed in the yolk sac, where they regenerate through self-renewal. In grown adults, circulating monocytes generated from the bone marrow are differentiated into macrophages to replenish their tissue abundance, mostly when injuries are present. Macrophages participate in many of the basic organic processes in the human body, such as cell and tissue development, metabolic regulation, tissue homeostasis, and pathogenic defense[1]. Macrophage strong influence in the maintenance of homeostasis makes them responsible for the potential initiation and progression of many pathophysiological diseases, such as autoimmune, obesity, cardiovascular, and cancer. It is believed that skewed macrophage activation towards a phenotype participates and influences the development and progression of the disease[2].

Macrophages get activated and change their functional phenotype when exposed to specific microenvironmental signals coming from the local tissue environment, this process is commonly known as macrophage polarization[3]. Cell and tissue damage, pathogen products, and activated lymphocytes, are some of the many cues macrophages respond to by differentiating into specific cell phenotypes. In the most simplistic schematic, macrophages are commonly classified into two states: M1 (classically activated) and M2 (alternatively activated) macrophages. M1 activation is characterized by pro-inflammatory functions: it's initiated by the presence of type 1 T

helper (Th1) cells and interferon-γ (IFN-γ) cytokines as well as bacterial endotoxin lipopolysaccharide (LPS) and it's typified by high secretion of tumor necrosis factor-α (TNF-α), interleukin-12 (IL-12), and interleukin-23 (IL-23) cytokines that propagate the inflammatory response down-stream; furthermore, reactive nitrogen and oxygen intermediate products are generated to help fight pathogen infection. In contrast, M2 stimulation encourages tissue repair and inhibits inflammation by the abundant secretion of IL-10 and low production of IL-12. The M2 activation can be further divided into at least three subsets, M2a, M2b, and M2c, due to their specific functions. M2a macrophages are involved in type 2 T helper (Th2) immune responses, such as parasite control, and are profibrotic whereas M2b are considered immunoregulatory macrophages. Both M2a and M2b macrophages secrete growth factors that assist angiogenesis and tissue regeneration. On the other hand, M2c macrophages are defined as being anti-inflammatory and participate in tissue repair and remodeling[3–5].

Unfortunately, this model lacks complete understanding of macrophage polarization due to the complex nature of macrophage development, differentiation, and maturation in both homeostasis and immune responses. The main limitations can be summarized as follows: the source of the stimuli, i.e. from cytokines, is usually ignored and the M1 and M2 activations are not isolated in tissues, and most likely, coexist with one another depending on the balance of activatory and inhibitory signals and the tissue environment. Recent studies have shown that M1 and M2 macrophages have indeed distinct differences but also have overlapping effects that have yet not been clearly described and need a more dynamic interpretation of the activation process[6].

In order to better understand macrophage activation and its heterogeneity, studies at the population level as well as at the single cell level are needed. Single cell experiments could potentially facilitate the identification of key factors (i.e. soluble proteins) that influence macrophage polarization, and also, determine and explain cell-fate decisions involved in macrophage related diseases[7].

1.2 Cellular heterogeneity and single cell analysis

Cellular heterogeneity is defined as the cell-to-cell variability found in any given cell population. Single cell analysis methods are techniques used to study these individual cell differences; these methods are becoming increasingly important since understanding how individual cells process information and respond to stimuli could lead to greater insight into cell heterogeneity and population behavior. It has been reported that single cells in the same cell population express genes stochastically leading to unique cell phenotype and cell behavior; specifically, differences in cell division, receptor expression, and protein secretion, as some of many examples, have been recently shown[8–11]. Additionally, single cell sequencing and expression profiling of immune and tumor cell populations have shown that individual cells from the same population process information and respond to stimuli in unique ways. These subset populations can express diverse surface biomarkers at unique concentrations, differentiate only when specific activation factors are present, and carry out reactions at specific response time rates[12–15].

Soluble proteins such as cytokines and growth factors play a critical role in controlling the behavior of cell populations within tissues; especially in the immune

system, where cell-to-cell communication and interaction is extremely important to deliver specific coordinated responses for a certain cellular event. Specifically, single cell analysis are of special interest in immunology mainly because of two reasons: 1. the immune system is comprised of many sensitive biological processes (i.e. cell differentiation and specialization) that could be better discerned and explained by studying single cells individually and 2. immune responses and macrophage activation are most likely being elicited by only a limited number of specific cells that could potentially be identified and isolated for further studies[7].

1.3 Soluble protein secretion from single cells

One area that needs additional research is detection and quantification of soluble proteins secreted from single cells. Soluble proteins, i.e. cytokines, chemokines and growth factors, are primordial for cell-to-cell communication and interaction in immune responses. Furthermore, these effector proteins are essential in macrophage activation, differentiation, and communication with both immune and non-immune cells in the body. Current bulk assays measuring secreted protein concentration are only able to deliver an average response from the whole cell population, masking the behavior of individual cells. Population assays prevent the identification of interesting cells that might be responsible for initiation and subsequent progression of immune responses. Also, detection of rare cells (expression in the heterogeneous population <0.01%) within a population is becoming increasingly important in many areas; in the immune system, identification of antigen-specific lymphocytes and hematopoietic stem cells are of vital importance to study key regulatory pathways in both steady-state and during disease

progression[13]. Moreover, sensitive and selective immunoassays for the detection and quantification of secreted products from macrophages are desirable due to their influence in disease diagnosis and management.

Defining the type and concentration of these driver cells can lead to a better understanding of population behavior in healthy or diseased systems, but directly monitoring cell secretion is technically challenging. Conventional bulk assays, such as enzyme-linked immunosorbent assay (ELISA), can only provide population averages that mask unique cell-to-cell single cell behaviors[9]. In bulk assays, distinguishing if the measurements come from a pronounced effect from a small number of cells or a minor effect from almost all cells in the population is unfeasible. Thus, analyzing cells individually within a population is necessary to understand cell population behavior and dynamics. Enzyme-Linked ImmunoSpot (ELISPOT) addresses this issue to a degree, but results are not quantitative and proteins cannot be correlated to the cell that secreted them. Immunofluorescence imaging, flow cytometry, and single cell transcript sequencing can measure the protein content, but these technologies do not assess the act of protein secretion and/or magnitude, multiplexing capacities are limited, and don't take into account the paracrine signaling effect on neighboring cells when cultured as a bulk. Thus, better techniques for the detection of secreted products from single cells from the immune system are strongly needed.

To address these issues, single cell microfabricated arrays have been developed that isolate single cells and their secreted products in nanoliter microwells[16]. The microwells are then covered with a glass slide containing immobilized capture antibodies to detect proteins secreted from single cells, retaining the original spatial

distribution of the array. Afterwards, the glass slide is removed, and protein concentration quantified by immunofluorescence (Figure 1.1). Using this technique, single cell secretion has been monitored for B and T lymphocytes, primary and circulating tumor cells, and macrophages in engineered adhesive contexts[17–19]. While this technology has already provided valuable insights into secretion heterogeneity, the detection is limited to sensitivities in the ng/ml range or 60 pM, orders of magnitude lower than ELISA. Thus, increasing detection sensitivity would significantly improve this already powerful analysis technique by enabling interrogation at earlier time points or assessing cell responses to subtle activation factors.

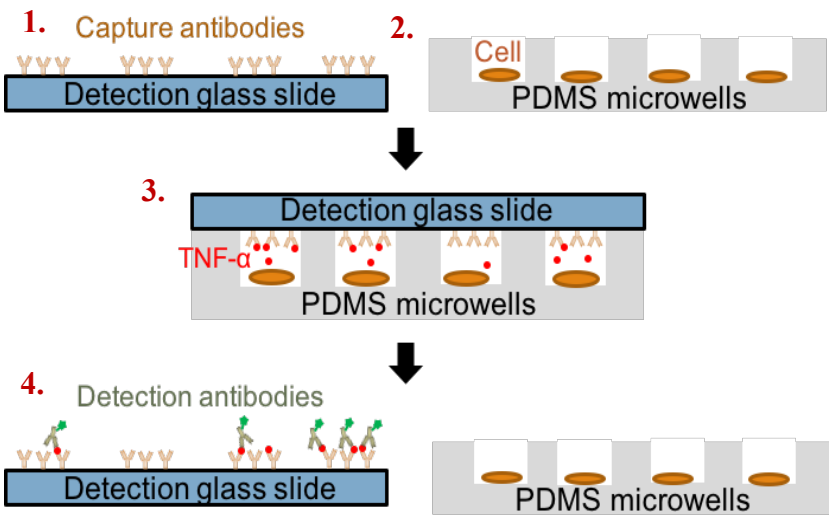

Figure 1.1. Schematic of microwell array detection. 1. Detection glass slide contains immobilized capture antibodies for protein of interest. 2. Cells are deposited in PDMS microwells. 3. Detection glass slide is placed in contact with microwells and incubated. 4. The two components are separated, microwells are placed in medium and detection glass slide is analyzed by fluorescence immunoassay[16].

1.4 Adapting multiplexing capabilities

Multiplexing assays allow for the simultaneous detection of multiple analytes at once. Secreted proteins, such as cytokines, chemokines, and growth factors, dictate the behavior of cells and mediate cell-to-cell paracrine and autocrine signaling in healthy and diseased tissues. Specially in the immune system, where these secreted proteins

facilitate the systematic cellular response to a biological event[20]. Cells in the immune system can express polyfunctionality, which is known as the secretion of two or more effector proteins from the same cell[21]. Understanding the secretomic signature of cells in different microenvironments can lead to great discoveries in cell development and disease treatment. Thus, developing a multiplex detection technology that can interrogate several cytokines of interest simultaneously from single cells is of crucial importance not only for understanding the biological nature of cell population behavior, but also to monitor disease diagnosis and treatment.

In macrophage polarization, more than one soluble protein is responsible for the initiation and propagation of macrophage differentiation, as well as immune response progression. Furthermore, specific cytokines stimulate macrophage cells to activate in distinct states, such as M1 or M2 phenotypes, and identifying the kind of proteins and the protein amount secreted by these activated cells can help confirm their polarization state. Therefore, adapting multiplexing capabilities is of great importance since concurrent detection of proteins secreted from stimulated single cells can offer valuable new insight into the mechanism of cell population behavior in the immune system[20,22].

1.5 Nanoparticle probes for single cell analysis

Molecular imaging encompasses the visualization and quantification of biological processes *in vivo* at the cellular and molecular level[2]. Nanoparticles, molecules that have a diameter ranging from 1-100 nm, have significantly increased sensitivity and specificity of diagnostic imaging due to their unique physicochemical properties, such as characteristic physical signals, compositional tunability, and chemical and physical

robustness. These attributes offer distinct advantages in molecular imaging that have directly resulted in improved detection of cellular targets under numerous modalities[2,23–25].

Semiconductor quantum dots (QD) are a class of inherent fluorescent nanoparticles (ranging from 2-10 nm in diameter) that possess distinctive optical and electrical properties[26]. QD have size-dependent emission wavelengths where the bigger the nanocrystal results in a red shift in QD emission. They provide several advantages compared to organic fluorophores, such as longer fluorescence lifetimes (>10 ns), extreme brightness, and photostability that readily enables single particle detection, imaging, and tracking[25,27,28]. Quantum dots have two great properties that makes them excellent probes for multiplexing detection: 1. Broad absorption bands that allow multiple quantum dots to be excited with a single light source and 2. narrow emission bands that minimize signal crossover[29]. Furthermore, biomolecules can be conjugated to the surface of nanomaterial probes for the efficient multivalent adhesion to molecular targets.

Bioorthogonal chemistries, reactions inside living systems that occur without interfering with innate biochemical processes, can be utilized for nanoparticle probe's conjugation purposes. These reactions are fast and offer control and flexibility for investigating biomolecule targets (i.e. soluble proteins) with nanomaterial probes (i.e. QD)[30]. Bioorthogonal cycloaddition between trans-cyclooctene (TCO) and tetrazine (Tz) has been characterized for the direct conjugation of antibodies and nanoparticles[31]. The biomarker of interest is first targeted with a TCO-modified monoclonal antibody, followed by reaction with Tz-modified nanoparticles, resulting in >10-fold signal

enhancement over traditional nanoparticle immunoconjugates (ICs). It is believed that the signal increase can be a consequence of the possibility that multiple nanoparticles were attached to a single antibody due to the very small footprint given by the cycloaddition product. Recently, the robustness and sensitivity of the TCO/Tz conjugation was improved by using a hydrophilic polyethylene glycol (PEG) linker to unmask the buried hydrophobic TCO moieties within antibodies after bioconjugation; allowing for an even greater signal enhancement[32]. Based on these benefits, monoclonal antibodies conjugated to QD via TCO/Tz bioorthogonal chemistries can be utilized to improve the detection of secreted proteins from single cells.

1.6 Fluorescence lifetime imaging microscopy

Fluorescence lifetime is defined as the average time a fluorophore stays in its excited state before returning to its ground state, emitting a photon[33]. The fluorescence lifetime (τ) of molecules can range from picoseconds to hundredths of nanoseconds and it can be explained as the time it takes for fluorescence light emission to decay to 1/e of the initial intensity, as given by the equation:

$$I(t) = I_0 e^{-\frac{t}{\tau}} \quad (1)$$

where I is the intensity, I_0 is the intensity at time zero, and t is the time after the excitation pulse.

Time-domain and frequency-domain are the most common methods to acquire fluorescence lifetime measurements. In the time-domain, a short pulse of light illuminates the sample and the delayed emission photons are collected over time in a histogram[34]. In the frequency-domain method, the excitation light is sinusoidally

modulated, generating a phase-delayed fluorescence emission frequency and a change in amplitude relative to the excitation source[35]. Unfortunately, both methods are really complicated to implement, especially when trying to resolve individual lifetimes from a mixture.

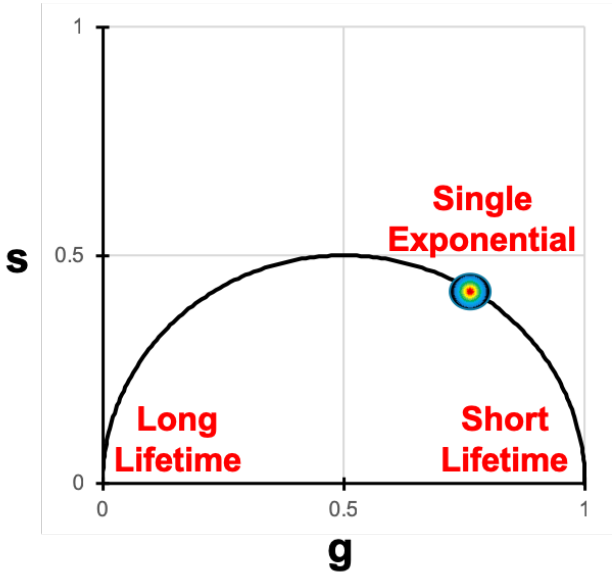

Figure 1.02. Phasor plot of fluorescence lifetime. Schematic of the phasor plot depicting location of clusters that correspond to lifetime decay curves. Longer lifetimes are found on the left and shorter lifetimes are located on the right side of the phasor. Single exponentials are located somewhere along the universal circle, and complex decays within the semicircle.

The phasor approach to fluorescence lifetime imaging microscopy (FLIM) is a simple, rapid, and fit-free method for analyzing lifetime data. This method transforms the histogram of the time delay of each pixel into sine and cosine polar coordinates[36]. The sine and cosine transforms correspond to the *g* and *s* coordinates of the polar plot, referred to as phasor plot, where each pixel of the fluorescence lifetime image corresponds to a unique point on the phasor plot. The following equations correspond to the *g* and *s* coordinates:

$$g_{i,j}(\omega) = \frac{\int_0^\infty I_{i,j}(t)\cos(\omega t)dt}{\int_0^\infty I_{i,g}(t)dt} \quad (2)$$

$$s_{i,j}(\omega) = \frac{\int_0^\infty I_{i,j}(t)\sin(\omega t)dt}{\int_0^\infty I_{i,g}(t)dt} \quad (3)$$

where *i* and *j* refer to the pixel of an image, and ω is the laser repetition angular frequency. The FLIM measurements can also be taken in the frequency domain, where the *g* and *s* coordinates are given by:

$$g_{i,j}(\omega) = m_{i,j}\cos\varphi_{i,j} \quad (4)$$

$$s_{i,j}(\omega) = m_{i,j}\sin\varphi_{i,j} \quad (5)$$

where $m_{i,j}$ refers to the modulation and $\varphi_{i,j}$ to the phase shift of the emission with respect to the excitation.

The phasor approach simplifies lifetime data by replacing complex decay curves with a simple graphical representation. Clusters of pixel values in specific locations on the phasor plot correspond to specific lifetimes from fluorescent species, as can be seen in Figure 1.2[36,37]. Short lifetimes are depicted on the right side of the phasor (closer to coordinates (1,0)) and long lifetimes are found on the left side of the phasor (closer to coordinates (0,0)). Therefore, each fluorescent species has a unique position on the phasor plot that is related to its lifetime. Pixels that contain only a single lifetime will fall somewhere along the universal circle of the phasor plot, whereas pixels that have a mixture of lifetimes will

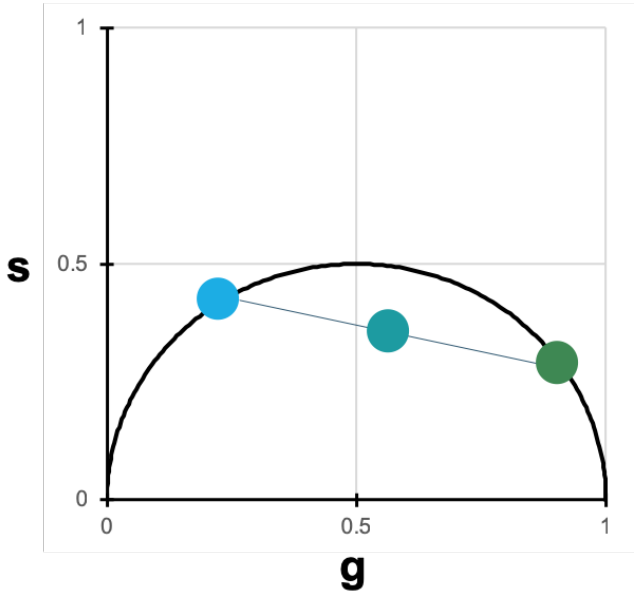

Figure 1.3. Multi-component analysis using the phasor approach. If a pixel contains a mixture of two fluorescent species, the location on the phasor will fall along the line of the two pure species.

appear within the circle. The pixels with a mixture of fluorescent species will appear somewhere along the line of the two pure species (Figure 1.3). The precise location along the line depends on the intensity-weighed fraction of each species present.

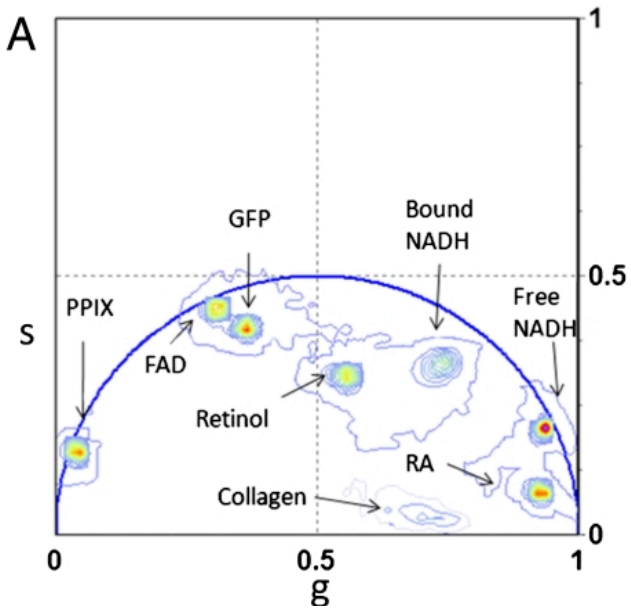

Figure 1.4. Phasor location of pure chemical species in tissue components. Phasor plot depicting the unique location of the fluorescence lifetime for endogenous fluorescent species.

As can be seen from Figure 1.4, this approach has been used to effectively distinguish 10 endogenous fluorescent species[37]. Every point on the phasor can be mapped to a corresponding pixel on the image. Furthermore, the concentration of each fluorescent species can also be measured if the relative brightness of the fluorescent specie is known[38].

1.7 Structure of the dissertation

The goal of this study was to develop an extremely sensitive QD detection platform with multiplexing capabilities to quantify secreted proteins from single cells for unveiling cellular heterogeneity in immune cells. To achieve these goals, QD imaging

and bioorthogonal Tz/TCO chemical amplification (ChemAmp) techniques were used to significantly improve detection of secreted TNF-α in single cell microarrays. Additionally, multiplexing capabilities were incorporated in the protein detection platform by conjugating multi-color QD probes to detection antibodies, allowing for the simultaneous sensitive detection of four secreted proteins (MCP-1, TGF-β, IL-10, and TNF-α) in single cell experiments. Furthermore, the phasor approach for FLIM was employed to assess and correct QD homoquenching.

CHAPTER 2: Ultrasensitive Detection of Secreted Proteins from Single Cells Using Quantum Dots

2.1 Introduction

Interest is rapidly growing to interrogate individual cells within diverse populations to obtain insight into the stochastic and heterogeneous nature of biological systems and to identify rare driver cells.[14,39–44] For example, single cell sequencing and protein expression profiling have shown that individual cells process information and respond to stimuli in unique ways.[45–51] Additionally, single cell analysis methods have been used to assess tumor heterogeneity, inform therapy decisions, and identify cells possessing metastatic or stem-like properties. Soluble proteins such as cytokines and growth factors play a critical role in controlling the behavior of diverse cell populations within tissues, but directly monitoring secretion from individual cells is technically challenging. The gold standard for detecting soluble proteins is the enzyme-linked immunosorbent assay (ELISA), but this is a bulk format that averages results over a population of cells.[52,53] Enzyme-linked immunoSpot (ELISpot) and fluorescence enzyme-linked immunoSpot (FLUOROSpot) address this issue to a degree, but secretion results are not quantitative nor strictly linked to the originating cell. Transcript and protein content can be assessed inside of cells by imaging, flow cytometry, or single cell sequencing, but these methodologies fail to convey direct information about secretion dynamics and/or magnitude. To address these shortcomings, microfabricated arrays have been developed that isolate single cells and their secreted products within sub-picoliter wells.[16] A glass slide containing immobilized capture antibody is used to seal the wells, enabling quantitation of secreted products while maintaining the spatial distribution of

the cell array. Large scale multiplexing (>40) has also been enabled in this format by spatially patterning different capture antibodies into barcodes on the glass detection slide.[54–56] Using this technique, generally termed micro- engraving, single cell secretion has been monitored for B and T lymphocytes, macrophages, neurons, and tumor cells.[18,54,56–60] Recently, we extended this technique to assess macrophages within engineered adhesive contexts using a three component well array.[17] While microengraving has provided valuable insights into secretion heterogeneity, detection has been based on a sandwich immunofluorescence detection scheme that is limited in sensitivity to ~1 ng ml^{-1}, or 10 pM, for most soluble proteins. This corresponds to a minimum of ~3000 molecules secreted per cell for standard microwell sizes,[61] and 30,000 molecules for larger microwells used to barcode capture antibodies.[56] By comparison, the detection threshold of standard ELISAs can routinely reach 100 fM, and has been further reduced to ~200 aM using ultrafast polydopamine deposition and to single molecule levels using digital ELISA.[60–62] However, these are all bulk assays that cannot be applied to single cell secretion studies. Detection of soluble protein as low as ~3 nM was demonstrated using immunofluorescence and a microfluidic microwell chamber platform.[54] This was achieved using a multi-round detection strategy including secondary antibody and avidin/biotin binding, valved microfluidic system, and DNA-based approach to conjugate capture anti- body. Further improvement in detection sensitivity would significantly advance single cell secretion studies by enabling interrogation of earlier time points or evaluation of more subtle activating stimuli, such as physiologically relevant cytokine concentrations and biophysical cues. Furthermore,

achieving these goals using a simple immunoassay format and standard microengraving platform would extend this capability to many more research labs.

Nanomaterial probes offer numerous advantages for molecular diagnostics, including unique detection signals, synthetic versatility, and robustness of chemical and physical properties.[27,63–66] These attributes have dramatically improved detection of biological targets under numerous assay formats and analytical modalities.[24,25] Applications have primarily focused on cell-associated proteins, but attention has also been given to soluble proteins using sandwich immunoassays. In a seminal study, soluble proteins were captured between magnetic beads and gold nanoparticles, the latter of which was conjugated with DNA bio-barcodes.[67] Using this method, prostate-specific antigen was detected at concentrations as low as 30 aM, which remains unmatched to date. Recently, carbon nanotubes were used with dielectrophoretic and hydrodynamic shear force alignment to achieve a detection limit of 100 aM.[68] While these nanotechnology-based methods have advanced the limits of detection for soluble targets, they have all utilized bulk assay formats similar to ELISA. Semiconductor quantum dots (QD) exhibit exceptional luminescence intensity and photostability, which has led to their use in sandwich immunoassays.[25] Using fluorescence microscopy or wave- guides, detection thresholds have consistently been achieved in the high fM range,[69–72] and even extended down as low as 25 fM.[73] While this represents an impressive three orders of magnitude improvement over immunofluorescence using organic fluorophores, no attempt has been made to further advance detection sensitivity by taking advantage of the fact that single QDs can readily be imaged using standard

fluorescence microscopy.[73,74] Moveover, QDs have not been explored in single cell secretion studies using the microengraving technique.

To improve the detection power of nanomaterial probes, we pioneered a novel method to amplify binding to biomarker targets that is based on the catalyst-free bioorthogonal cyclo-addition reaction between trans-cyclooctene (TCO) and tetrazine.[31] This involved tagging the protein of interest with a TCO-modified monoclonal antibody, followed by reaction with tetrazine-modified nanoparticles. Due to the small footprint of the cycloaddition product on a relatively large antibody scaffold, multiple nanoparticles attached to each protein target, which has consistently produced 3 to 10-fold signal enhancement over traditional nanoparticle immunoconjugates (IC).[31,75,76] Recently, we improved the robustness and overall power of our chemical amplification (ChemAmp) technique by increasing the density of reactive TCO moieties on the antibody, which tend to bury within the antibody during bioconjugation procedures.[32] To date, the simple yet powerful ChemAmp technique has been employed to detect protein targets on live and fixed human cells, bacteria, and microvesicles using magnetic nanoparticles and QDs,[30] but it has not been applied to secreted proteins.

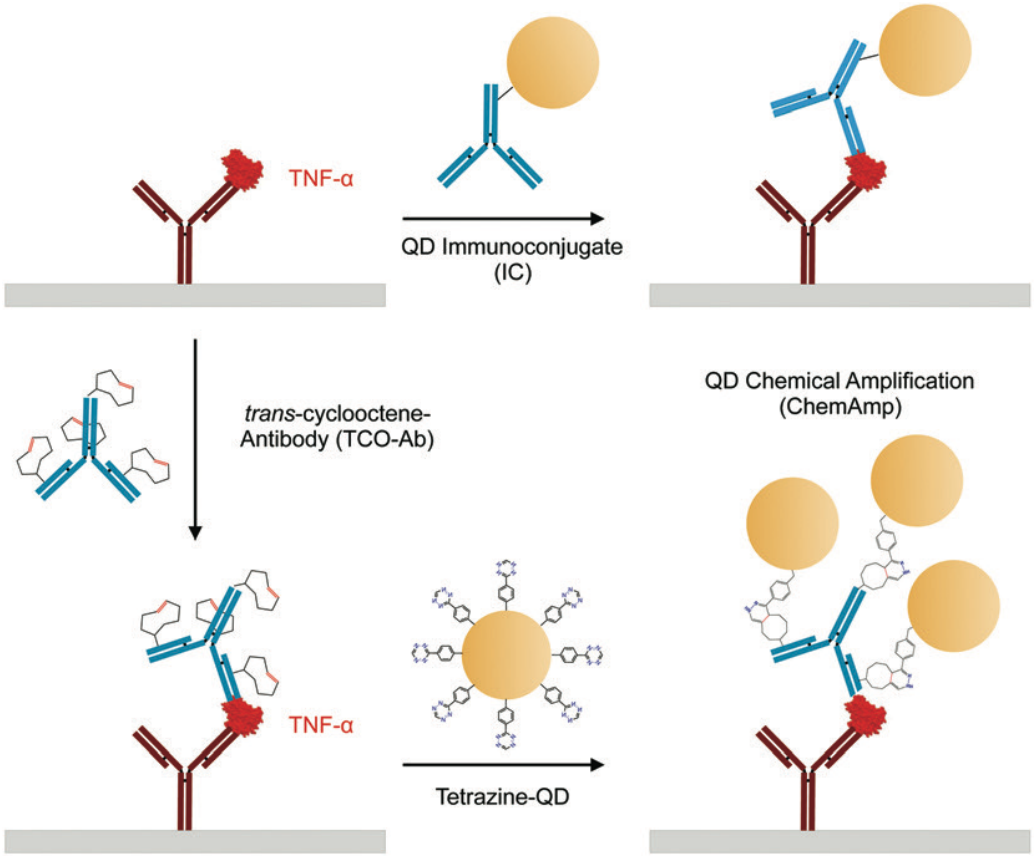

Figure 2.1. Quantum dot (QD)-based immunoassays for detection of TNF-α. Schematic of sandwich detection schemes using anti-TNF-α capture (red) and detection (blue) antibody pair. (Top) Standard immunoconju- gate (IC) format in which the detection antibody is first attached to the QD. (Bottom) Chemical amplification (ChemAmp) technique in which the detection antibody is modified with trans-cyclooctene (TCO), bound to TNF-α, and covalently reacted with tetrazine-modified QDs via bioorthogonal cycloaddition reaction. ChemAmp results in multiple nanoparticles attaching per detection antibody, enhancing detection sensitivity.

In this work, we evaluate the detection sensitivity of QDs for the inflammatory cytokine tumor necrosis factor-α (TNF-α) using various sandwich immunoassay formats (Figure 2.1) and a unique single QD imaging approach. We first optimize the QD sandwich immunoassays in well plates and find that the ChemAmp technique improves detection sensitivity by ~20- fold in comparison to a traditional QD IC and an organic fluorophore, and is comparable in sensitivity to an ELISA. Next we assess the QD IC on glass slides and demonstrate that QD imaging provides a detection threshold of 180 aM. This is >100-fold more sensitive than previously reported QD-based immunoassays

and >5 orders of magnitude more sensitive than organic fluorophores. Using the ChemAmp technique, detection threshold is further decreased to 60 aM, but we observe significant homoquenching between QDs at higher TNF-α concentrations due to elevated QD surface density. Thus, we conclude that the ChemAmp technique is only suit- able for low TNF-α concentration measurements. Using the QD IC, we perform single cell secretion studies using phorbol 12-myristate 13-acetate (PMA) differentiated and lipopolysaccharide (LPS) activated U-937 cells. We find that 3-fold more single cells are detectable compared to an organic fluorophore. This is accomplished by lowering detection threshold from 10 000 to only 2 or 3 molecules of TNF-α captured per micro-well. Thus, we conclude that our QD-based imaging method maximizes detection sensitivity by providing near-single molecule resolution.

2.2 Methods

All chemicals were purchased from Sigma-Aldrich (St Louis, MO) unless otherwise noted. DBCO-amine was purchased from Click Chemistry Tools (Scottsdale, AZ). Heterobifunctional carboxy-$(PEG)_4$-amine, amine-reactive succinimidyl ester (NHS)-azide, NHS-tetramehtylrhodamine (TMR), sulfo-NHS-LC-Biotin, sulfo-SMCC (sulfosuccinimidyl 4-(N-maleimidomethyl)cyclohexane-1-carboxylate), primary amine-terminated quantum dots (Qdot 605 ITK Amino PEG), NeutrAvidin-horseradish peroxidase (Neutravidin-HRP), and Neutravidin were purchased from Thermo Fisher Scientific (Waltham, MA). Recombinant human tumor necrosis factor-α (TNF-α) and matched monoclonal mouse antibodies for human TNF-α sandwich immunoassays ($IgG_1κ$, clones MAb1 and MAb11) were purchased from BioLegend (San Diego, CA).

2.2.1 Protein Conjugations

Anti-TNF-α capture (MAb1) and detection (MAb11) antibodies (Biolegend) were buffer-exchanged into phosphate buffered saline (PBS) using Zeba spin desalting columns (Thermo Scientific) prior to modification. Biotinylated capture antibody was prepared by reacting 250 µg antibody with 5 molar equivalents of sulfo- NHS-LC-Biotin in PBS containing 10% dimethylformamide (DMF) and 0.1 M $NaHCO_3$ (pH 8.4). Detection antibody was similarly modified with either 1000 molar equivalents of NHS-TCO, 50 molar equivalents NHS-azide, or 30 molar equivalents of NHS-TMR fluorescent dye. Neutravidin was modified with maleimide using 10 molar equivalents of sulfo- SMCC. All modified proteins were purified using Zeba spin desalting columns (Thermo Fisher). PEG-TCO modified detection antibody was prepared by reacting azide-modified anti- body with 10 molar equivalents of DBCO-PEG_4-TCO in PBS containing 10% DMF for 4 h at room temperature. PEG-TCO antibody was buffer-exchanged into PBS using Amicon Ultra-4 centrifugal filtration systems with 10 kDa MWCO (EMD Millipore). We note that TCO and PEG-TCO loading conditions were optimized in previous work to provide maximal reactive loading without affecting antibody binding affinity.[30] Antibody concentrations were determined by absorption measurement using a NanoDrop 2000 spectrophotometer. TMR modification level was determined to be ~2 dyes/antibody by absorption measurement. [32]

2.2.2 Preparation of Quantum Dots

Amine-terminated QD were modified with NHS-tetrazine, as described previously.[76] Briefly, 0.8 nmoles of amine-QD (Thermo Fisher) and 500 molar

equivalents of NHS-tetrazine were combined in PBS containing 5% DMF and 0.01 M $NaHCO_3$, reacted for 3 h at room temperature, and tetrazine-QD were purified into PBS using an Ultra-4 centrifugal filter with 100 kDa MWCO. QD immunoconjugates (IC) were prepared by reacting 0.15 nmole tetrazine-QD with 200 µg TCO-modified detection antibody (prepared with 30 molar equivalents TCO-NHS) in 1 ml of PBS containing 1% bovine serum albumin (BSA) (referred to as PBS+) for 3 h at room temperature. QD ICs were purified using Sephacryl S-400 (GE Healthcare) gel filtration media on an AKTA Pure FPLC system (GE Healthcare). Final concentrations were determined by absorption measurements and calibration using the QD stock solution.

2.2.3 Fabrication of PDMS Microwell Arrays

Silicon wafer (University Wafer, MA) were fabricated using SU-8 photolithographic techniques. Briefly, SU-8 50 photoresist (MicroChem, MA) was spin-coated onto a 3″ silicon wafer to get a uniform 80 mm thick layer. After baking at 95 °C for 2 h, the wafer was positioned under a transparency mask containing clear rectangles (90 µm × 90 µm) and was exposed to UV light (AB&M UV Flood Lamp Exposure System), following MicroChem protocol. After 10 minutes of post-exposure bake at 95 °C, the wafer was immersed in SU-8 developer for 5 minutes to wash off unpolymerized photoresist. Cleaned and dried wafer was baked at 200 °C for 30 minutes to allow SU-8 to crosslink completely. PDMS and curing agent (Dow Corning, MI) were mixed in 10:1 ratio and poured onto the silanized silicone master to produce the microwell array. Microwell height was determined to be 43 µm from microscope images taken in cross-

section. Thus, the microwells measured 90 μm × 90 μm × 43 μm, for a volume of ~350 pl. Arrays were then degassed, cured in oven at 65 °C, and sterilized with 70% ethanol.

2.2.4 Preparation of Detection Slides

Glass microscope slides (25 mm × 75 mm) were first cleaned using Piranha solution (3% H_2O_2 and concentrated H_2SO_4 at 1:2 volume ratio) for 30 min, rinsed with double deionized water H_2O (dH_2O), and dried in an oven for 1 h at 100 °C. Slides were then submerged in a solution of 4% (3-mercapto- propyl)trimethoxysilane in 100% ethanol for 1 h, rinsed with ethanol, and dried in the oven for 30 min. Silanized glass slides were stored in a desiccator until use. Prior to experiments with purified TNF-α, a 50 microwell silicon gasket (Grace Bio-Labs, OR) was placed onto the silanized glass slide and 5 μl of PBS containing 1 mg/ml maleimide-modified neutravidin was added to each well. After reacting for 2 h at room temperature, wells were washed with PBS, biotinylated capture antibody was incubated at 10 μg/ml in PBS for 2 h, and wells were blocked with StartingBlock for 15 min at room temperature. Purified TNF-α was then added at concentrations ranging from 500 ag/ml to 1 ng/ml in PBS+ and incubated for 2 h at room temperature. For single cell secretion studies, a 2 cm × 2 cm square region was outlined with a grease pen on silanized detection glass slides, coated with 125 μL of 1 mg/ml maleimide-modified neutravidin for 2 h, rinsed, blocked with 200 μL of PBS+ for 15 min, incubated with 125 μL of biotinylated capture antibody for 2 h at room temperature, and treated with PBS+ for 15 min at room temperature.

2.2.5 U-937 Cell Culture and Differentiation

The pro-monocytic, human myeloid leukemia cell line U-937 was obtained from ATCC (Manassas, VA) and cultured as recommended in RPMI 1640 medium supplemented with 2 mM L-glutamine, 10 nM HEPES, 1 mM sodium pyruvate, 4.5 g/L glucose, 1.5 g/L sodium bicarbonate, and 10% fetal bovine serum (Thermo Fischer Scientific, MA). For single cell experiments, U-937 cells were seeded at density of 500,000/ml in 12-well plates and differentiated with 50 ng/ml PMA for 48 h, followed by 24 h resting time in culture media. On the day of the experiment, the cells were treated with 4% Trypsin EDTA (Thermo Fisher Scientific, MA), and release was augmented with a cell scraper (Fisher Scientific, NH). Differentiated cells were then seeded onto the PDMS microwells by centrifuging at 700 rpm for 5 min and incubated for at least 1 h before stimulation with 100 ng/ml LPS. Detection glass slides were then inverted over the top of the microwells and sealed using an acrylic housing. TNF-α secretion was interrogated for 24 h at 37 °C, followed by imaging cells under bright field using an Olympus IX83 inverted microscope (Olympus, Japan) and a 10× objective (NA 0.3, Olympus) to determine the number of cells present within each microwell.

2.2.6 Detection of TNF-α by ELISA

Monoclonal human anti-TNF-α capture antibody was coated onto flat, non-tissue culture treated 96-well plates (Thermo Fisher Scientific, IL) by incubating at 5 µg/ml in 0.1 M $NaHCO_3$ (pH 9.2) for 2 h. Wells were then treated with StartingBlock (Thermo Fisher Scientific, MA) for 15 min, and 50 µL of purified human TNF-α (1 pg/ml to 2 ng/ml in PBS+) was added for 2 h at room temperature. After washing with PBS+, biotinylated

anti-TNF-α detection antibody was incubated at 5 μg/ml for 30 min, followed by Neutravidin- HRP at 1:500 dilution in PBS+ for another 30 min and a final wash step. Wells were developed by adding 100 μL 1-step Ultra TMB substrate (Thermo Fisher Scientific, IL) and reacting at room temperature for 15 min before quenching with an equal volume of 2 M H_2SO_4. TMB absorbance at 450 nm was quantified using an Infinite 200 PRO Multimode Reader (TECAN, Switzerland). Concentration was calibrated using the purified human TNF-α results and a linear regression.

2.2.7 Detection of TNF-α using a Fluorescent Plate Reader

TNF-α capture was performed as described in the previous section, except black 96-well plates (Corning, NY) were used. Detection procedures were performed by incubating TMR, TCO, or PEG-TCO modified detection antibody at 10 μg/ml in PBS+ for 30 min at room temperature. For TCO and PEG-TCO cases, an additional incubation was performed using 5 to 50 nM Tz-QD in PBS+ for 30 min at room temperature to achieve Chemical Amplification (ChemAmp). TMR and QD intensities were quantified using a Fluoroskan Ascent Microplate Fluorometer (Thermo Fisher Scientific, IL) using the following excitation/emission wave- lengths: 552/575 nm for TMR or 460/590 nm for QDs.

2.2.8 Detection of TNF-α by Fluorescence Imaging

The silicon gasket or PDMS wells were carefully separated from the glass slide, immediately washed with 200 μL ice cold PBS+, and labeled as described for plate assays using TMR-modified detection antibody (10 μg ml^{-1}), QD IC (20 nM), or TCO-

PEG- modified detection antibody (10 μg ml^{-1}) followed by Tz-QD (20 nM) for ChemAmp. After additional washing with ice cold PBS+, a cover slip was mounted in preparation for imaging.

2.2.9 Imaging and Analysis

Glass slides were imaged using an Olympus X83 inverted microscope, TRITC filter set (532–554 nm band-pass exci- tation, 570–613 nm band-pass emission, Olympus) or single- band QD 605 nm filter set (415–455 nm single band exciter, 590–620 nm single band emitter, QD605-C-OFX, Semrock, NY), and 40× oil-immersion objective (NA 1.3, Olympus). Images were captured using an Orca-R2 CCD camera (Hamamatsu Photonics, Japan) and mManager control software for at least five fields of view per sample using 100 ms and 500 ms integration times for TMR and QD, respectively. Under these conditions, single QDs could readily be resolved on control slides. ImageJ software was then used to quantify mean fluorescence intensity. Briefly, control images were used to optimally set thresholds for brightness and contrast for visualizing single QDs in the image, and these settings were then applied to the remaining conditions. Mean fluorescence intensity was then determined using ImageJ and the built-in measure tool. For single cell studies, the complete series of brightfield (cells) or fluorescence (TNF-α) images were stitched together using Fiji software and the Grid/Collection Stitching plug-in and analyzed. Microwell locations were then defined in the stitched fluorescence images by aligning with the stitched bright field images using the built-in mask, selection, and ROI manager tools. Wells containing either zero (empty wells), one (single cell wells), or multiple cells were manually

selected and their ROI stored for later analysis. Afterwards, the defined ROIs for empty and single cell wells were superimposed on the fluorescence images from the detection glass slides and the mean intensity for each ROI was obtained with the built-in multi-measure tool in ImageJ. Matlab was then used to generate mean intensity histograms for single cell and empty well counts. Mean intensity was also determined for the empty wells to determine the limit of detection. We chose to use two standard deviations higher than this mean intensity, which resulted in false positive rates of ~3% for both TMR and QD IC cases. Finally, TNF-α secretion for the positive population was calibrated from intensity measurements obtained using purified TNF-α for both TMR and QD IC, and correction was made for the false-positive rate by removing cells from the low TNF-α concentration range corresponding to 3% of the total population.

2.2.10. Image Processing and Fluorescent Spot Analysis

Matlab (MathWorks, MA) was used to further analyze images based on individual fluorescent spots. Images were first converted to binary using a built-in command (graythresh). Discrete, contiguous fluorescent spots were then identified, and the area and mean intensity of each spot was quantified. Processed images were created to depict the size of each QD spot in black and the average intensity by color-coded outlines based on a heat map. The intensity versus area values were then plotted for control samples to establish a gate for single QDs. For positive TNF-α conditions, spots that deviated from the control distribution in terms of larger size or diminished intensity were considered to be either quenched single QDs or large QD clusters.

2.2.11. Bulk ELISA Experiments

U-937 cells were seeded at densities of 1,000, 2,000, or 5,000 cells per well in 96-well plates and differentiated with 50 ng/ml PMA for 48 h. Following a 24 h resting period in culture media, cells were stimulated with 100 ng/ml LPS and cell supernatant was collected after 3 or 6 h LPS incubation. ELISA experiments were performed on cell supernatants to quantify TNF-α secretion, as described in the main text. Briefly, monoclonal human anti-TNF- α capture antibody (5 μg/ml in 0.1 M $NaHCO_3$, pH 9.2) was incubated in flat, non-tissue culture treated 96-well plates (Thermo Fisher Scientific, IL) for 2 h. Wells were then blocked with StartingBlock (Thermo Fisher Scientific, MA) for 15 min, followed by incubation with 50 μL of cell supernatant for 2 h at room temperature. After washing with PBS+, biotinylated anti-TNF-α detection antibody was incubated (5 μg/ml for 30 min in PBS+), followed by Neutravidin-HRP (1:500 dilution in PBS+) for 30 min. Finally, wells were washed and 100 μL 1-step Ultra TMB substrate (Thermo Fisher Scientific, IL) was added for 15 min before quenching with an equal volume of 2 M H_2SO_4. TMB absorbance at 450 nm was quantified using an Infinite 200 PRO Multimode Reader (TECAN, Switzerland). Concentration was calibrated using the purified human TNF-α results and linear regression.

2.3 Results

2.3.1 Detection of TNF-α by ELISA and Fluorescence in Well Plates

We first evaluated TNF-α detection capacity using bulk assays via ELISA and immunofluorescence using an organic fluorophore or QDs in 96 well microtiter plates.

For all cases, anti-TNF-α capture antibody was physisorbed to the plastic and purified recombinant human TNF-α protein was incubated at concentrations ranging from 1 to 2000 pg ml^{-1}. ELISAs conducted using biotinylated anti-TNF-α detection antibody, Neutravidin-HRP, and TMB substrate yielded a detection threshold of ~5 pg ml^{-1}, or 300 fM (Figure 2.2A). This is consistent with ELISA results in the literature, as well as information provided by the manufacturer. Next we evaluated immunofluorescence-based detection using tetramethyl- rhodamine (TMR)-modified detection antibody and a fluorescence plate reader. Detection sensitivity was orders of magnitude lower than ELISA, with a threshold of ~300 pg ml^{-1}, or 18 pM (Figure 2.2B). Finally, we investigated QD-based immunoassays under different formats: QD pre-conjugated with detection antibody to form an immunoconjugate (QD IC) or modified with tetrazine for chemical amplification (ChemAmp) to trans-cyclooctene (TCO)-modified detection antibody (Figure 2.1). Specifically, ChemAmp was performed using detection anti- body that was modified with TCO and a polyethylene glycol (PEG)-TCO conjugate that we have shown provides higher reactivity.[32] We initially tested different QD concentrations using 500 pg/ml TNF-α, and found that 20 nM was optimal for all cases (Figure 2.2C). This was due to higher background at 50 nM. Thus, 20 nM QD concentration was used for all subsequent studies in this work. QD signal response curves attained at different TNF-α concentrations are presented in Figure 2.2D. ChemAmp using PEG-TCO yielded significantly greater signal at all TNF-α concentrations. Detection thresholds were ~100 pg/ml (6 pM) for the QD IC, ~30 pg/ml (2 pM) for ChemAmp using TCO-modified detection anti- body, and ~3 pg/ml (180 fM) for ChemAmp using PEG-TCO- modified detection antibody. Based on these results, the PEG-TCO format was used for all

subsequent ChemAmp experiments in this work. These findings confirm that attachment of QDs using the tetrazine/TCO cycloaddition chemically amplifies binding to a soluble

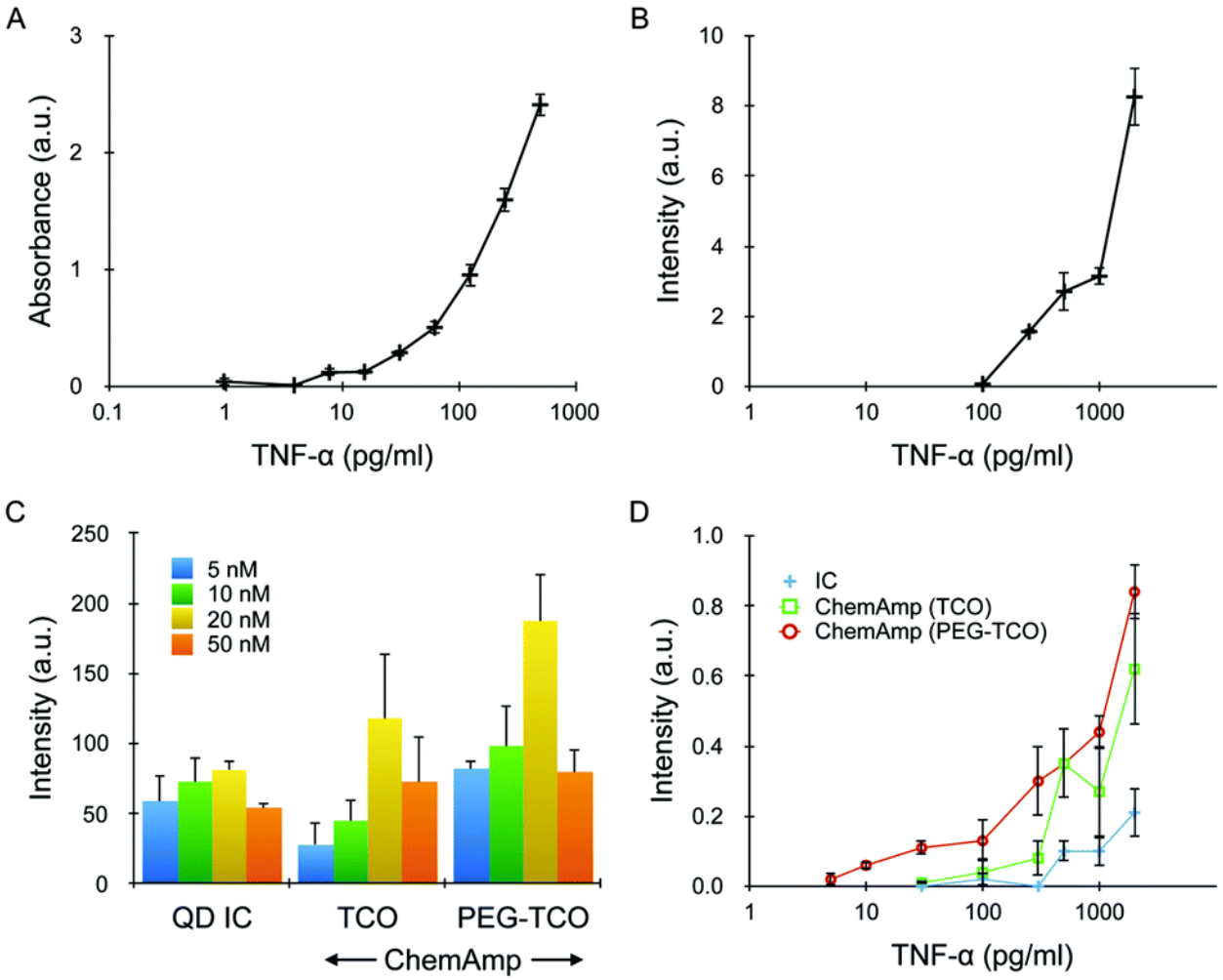

Figure 2.2. TNF-α detection in microtiter plates. (A) ELISA results performed using biotinylated detection antibody, avidin-HRP, and TMB substrate. Detection threshold, defined as the lowest TNF-α concentration at which signal was three standard deviations greater than background, was ~5 pg ml^{-1}, or 300 fM. (B) Standard immunofluorescence assay performed using rhodamine-labeled detection antibody (TMR), with detection threshold at ~300 pg ml^{-1}, or 18 pM. (C) QD results for an IC, as well as the ChemAmp technique using TCO and PEG-TCO modified detection antibodies. TNF-α concentration was 500 pg ml^{-1}, and the maximum signal was obtained at 20 nM QD concentration for all cases. The decrease at 50 nM was due to higher background. (D) QD intensities for all 3 detection formats as a function of TNF-α concentration. Detection thresholds were 100 pg ml^{-1} (6 pM) for the IC, 30 pg ml^{-1} (2 pM) for ChemAmp with TCO-modified detection antibody, and 3 pg ml^{-1} (180 fM) for ChemAmp with PEG-TCO-modified detection antibody. All results were background subtracted using the signal obtained from nonspecific QD binding. Error bars represent the standard error from at least three independent experiments.

protein in sandwich immuno- assays, providing detection sensitivity that is superior to a QD IC. All QD formats provided greater detection sensitivity than the organic fluorophore, and the ChemAmp technique was comparable to an ELISA.

2.3.2 Detection of TNF-α by Imaging

Next, we transitioned to fluorescence imaging in preparation for single cell secretion studies. Glass slides were silanized, covalently reacted with Neutravidin, modified with biotinylated capture antibody, and incubated with purified human TNF-α. Fluorescence signal for TMR was only detectable above 1 ng/ml (60 pM; Figure 2.3). This was significantly less sensitive than the microtiter plate experiments, but consistent with previous microengraving studies.[19,57] We also evaluated QD-based detection for the IC and ChemAmp formats. Images were captured using a QD605 filter cube and sufficient integration time to resolve individual fluorescent spots on control slides, which we presumed were mostly single QDs. Representative images for select TNF-α concentrations are shown in Figure 2.4A, and for all concentrations in the Figure 2.5. After quantifying mean intensity and subtracting the background signal, we found that dynamic range spanned six orders of magnitude in TNF-α concentration for both QD assay formats (Figure 2.4B). The QD IC response curve was monotonic, and surprisingly exhibited higher signal levels than the ChemAmp case at all but the high and low extremes. Three distinct regimes were observed for the ChemAmp case, with signal rising very slowly from baseline up to 8 pg ml^{-1}, decreasing in the range of 10–30 pg ml^{-1}, and finally rising quickly to high TNF-α concentrations. Decreased signal between 10 and 60 pg/ml was highly consistent across all experiments, and can clearly

be seen for the 16 pg/ml image in Figure 2.4Aii. We attribute this to homo-quenching between neighboring QDs, which was confirmed based on image processing of individual fluorescent spots in the next section (Figure 2.6 and 2.7).

Quenching effects were not observed in Figure 2.2 or previous work with cells,[31,32] but likely resulted here due to the planar geometry of the glass substrates and higher overall capture antibody density. Another factor that may have promoted quenching is oligomerization of TNF-α, but this only tends to occur at concentrations in excess of 1 nM or 10 ng ml^{-1}.[77] The QD IC was not affected by quenching (Figure 2.8 and 2.9) suggesting that the ChemAmp technique did have higher overall QD density even though signal intensity was lower. Focusing on the low TNF-α range and now

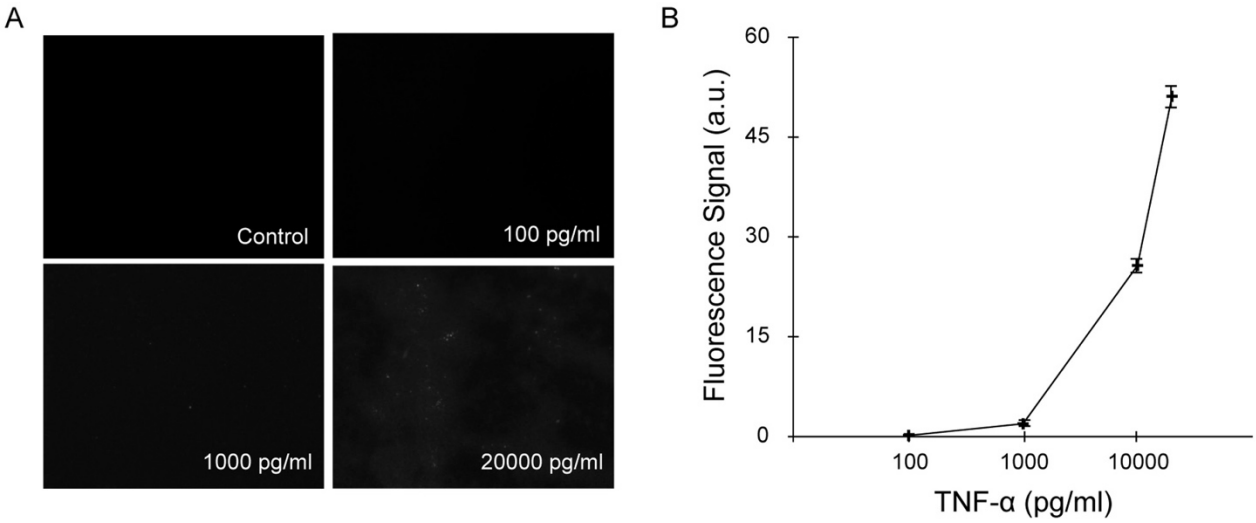

Figure 2.3. TNF-α detection by imaging rhodamine. (A) Representative images at select TNF-α concentrations for tetramethylrhodamine (TMR)-modified detection antibody. (B) Fluorescence intensity standard curve obtained using different TNF-α concentrations, after background subtraction. Detection threshold was ~1 ng/ml (60 pM). Error bars represent the standard error from at least three independent experiments.

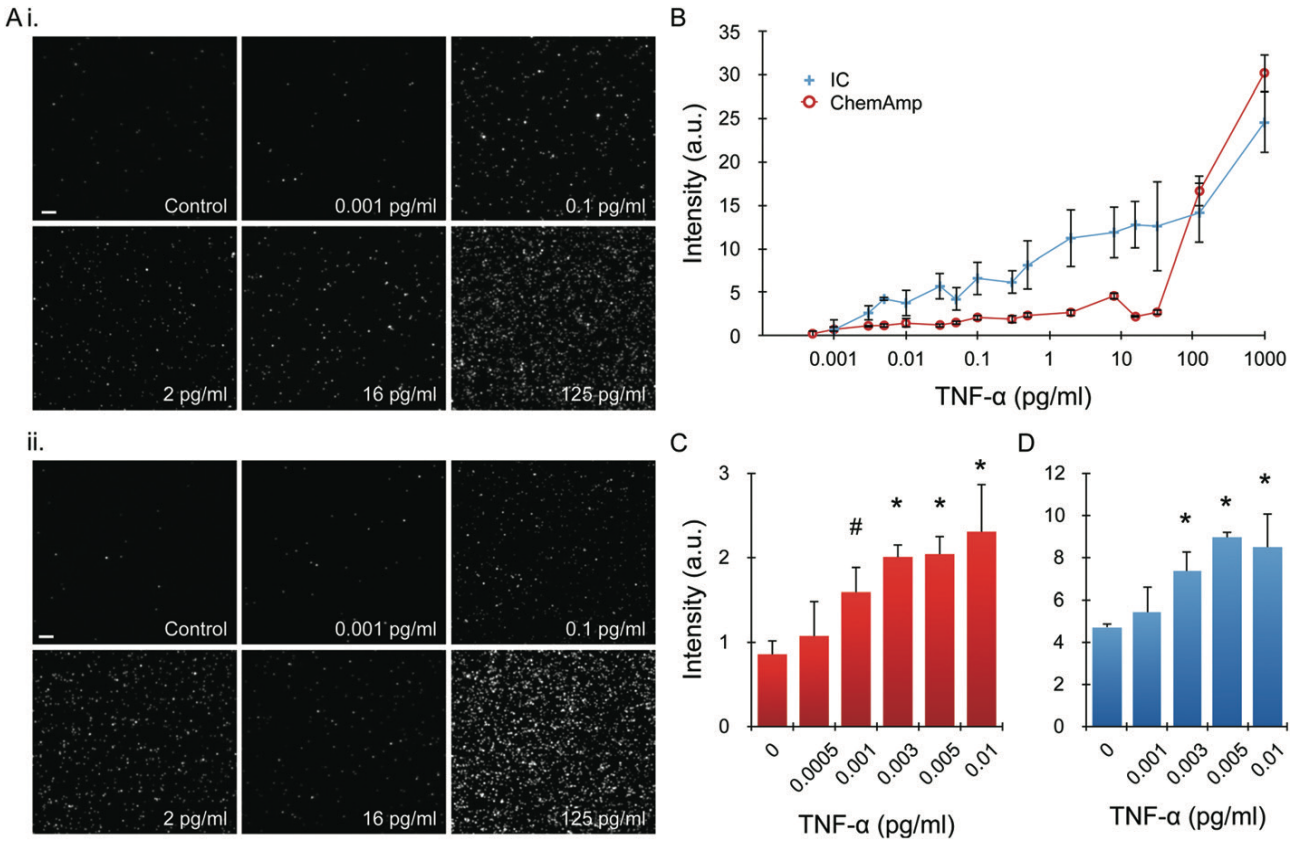

Figure 2.4. TNF-α detection by imaging. A) Representative images at select TNF-α concentrations for (i) QD IC and (ii) ChemAmp technique (PEG-TCO case). (B) Average intensity, after background subtraction, obtained across 6 orders of magnitude in TNF-α concentration. The response curve for the QD IC was generally monotonic, while the ChemAmp case was complex. The QD IC also exhibited higher signal at most TNF-α concentrations. (C, D) Mean intensities in the low TNF-α concentration range, including comparisons to control, for (C) ChemAmp and (D) IC cases. Detection thresholds were 1 fg ml^{-1} (60 aM) and 3 fg ml^{-1} (180 aM), respectively. Scale bars are 100 μm. Error bars represent the standard error from at least three independent experiments. # denotes $p < 0.05$ and * denotes $p < 0.01$ when compared to controls.

comparing directly to background signal, both QD assay formats provided statistically significant detection down to 3 fg ml^{-1}, or 180 aM (Figure 2.4C and 2.4D). This also corresponded to three standard deviations above the mean intensity of the control, which is typically used to define detection threshold.[54,57,66]

The ChemAmp technique was superior at low TNF-α concentration, primarily due to lower background signal (Figure 2.4C and 2.4D), which enabled detection threshold to extend down to 1 fg ml^{-1}, or 60 aM. This is orders of magnitude more sensitive than standard ELISA and 3-fold more sensitive than enhanced ELISA with ultrafast polydopamine deposition.[62,67] Most importantly, compared to other probe- based methods, it has only been surpassed by bulk methods such as the bio-barcode and digital ELISA assays.[66] For QD- based immunoassays, the lowest reported detection threshold was ~25 fM, which was attained using a QD IC for two soluble cancer biomarker proteins.[72] We have achieved a ~150-fold improvement here using a similar QD IC format, which we attribute to our unique approach to image single QDs. While

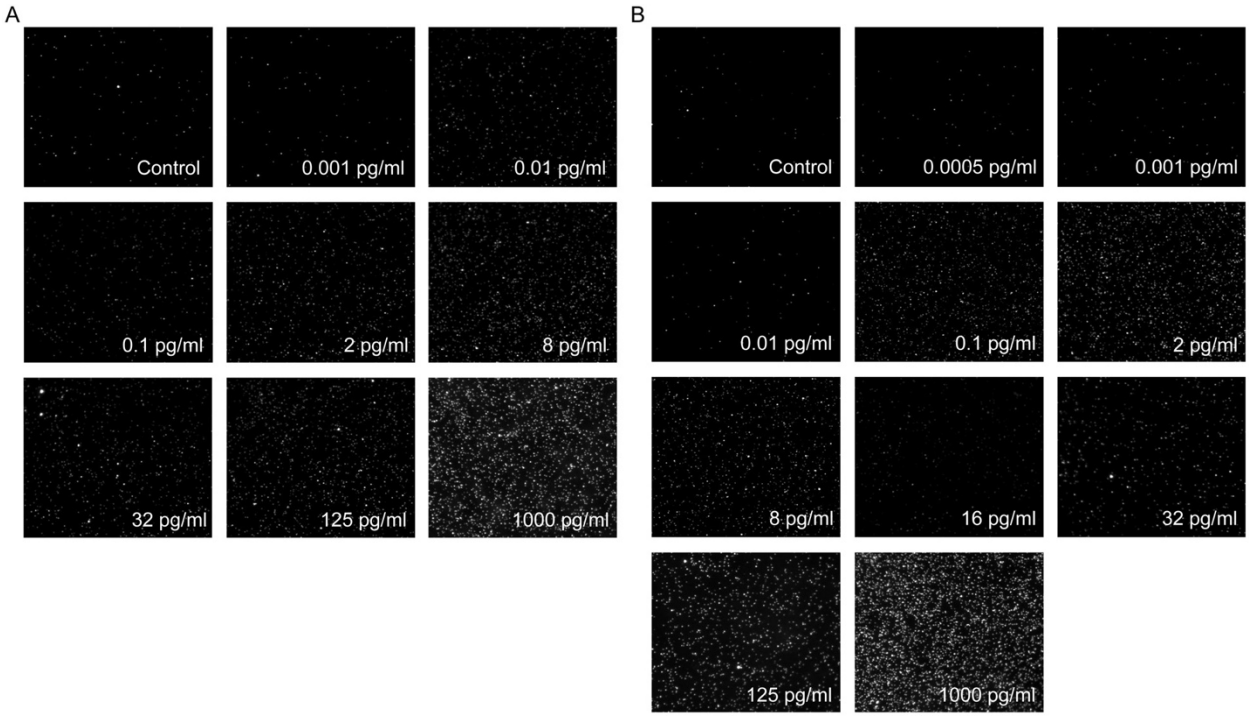

Figure 2.5. Representative QD images at all TNF-α concentrations. Results shown are for (A) QD IC and (B) ChemAmp cases, and TNF-α concentration is indicated in each image.

the ChemAmp technique further improved detection sensitivity by another 3-fold, the complex relationship between intensity and TNF-α concentration would make it difficult to quantify secretion across the full dynamic range of interest. Thus, we conclude that as currently deployed, the ChemAmp technique would only be recommended for detecting the very low concentration range (0.001 to 0.01 pg ml^{-1}). Quantitation of higher concentrations could potentially be addressed by image processing, and we describe a look-up table approach in the next section. The ideal solution would involve directly assessing quenching using a technique such as fluorescence polarization microscopy or fluorescence lifetime imaging microscopy, or eliminating quenching entirely by separating QDs further apart from each other using molecular spacers or a protective shell. These strategies will be pursued in future work.

2.3.3 Analysis of QD Fluorescent Spots

The complex relationship intensity profile that was observed for the ChemAmp technique would make it difficult to quantify concentration, particularly at high values. To address this issue, we processed images using Matlab to identify all contiguous fluorescent spots, which were then enumerated and assessed for intensity and area. Representative processed images are shown for select TNF-α concentrations in Figure 2.6, along with the corresponding raw and grayscale images. Spot number per image increased progressively until reaching a plateau around 10 pg/ml, then fell sharply at 16 pg/ml before rising again (Figure 2.6B). We then normalized the intensity by spot number, and the results are presented in Figure 2.6C. We found that the intensity per

spot was consistent at low TNF-α concentrations, decreased for the region spanning 0.3 to 30 pg/ml, and increased markedly at high concentrations.

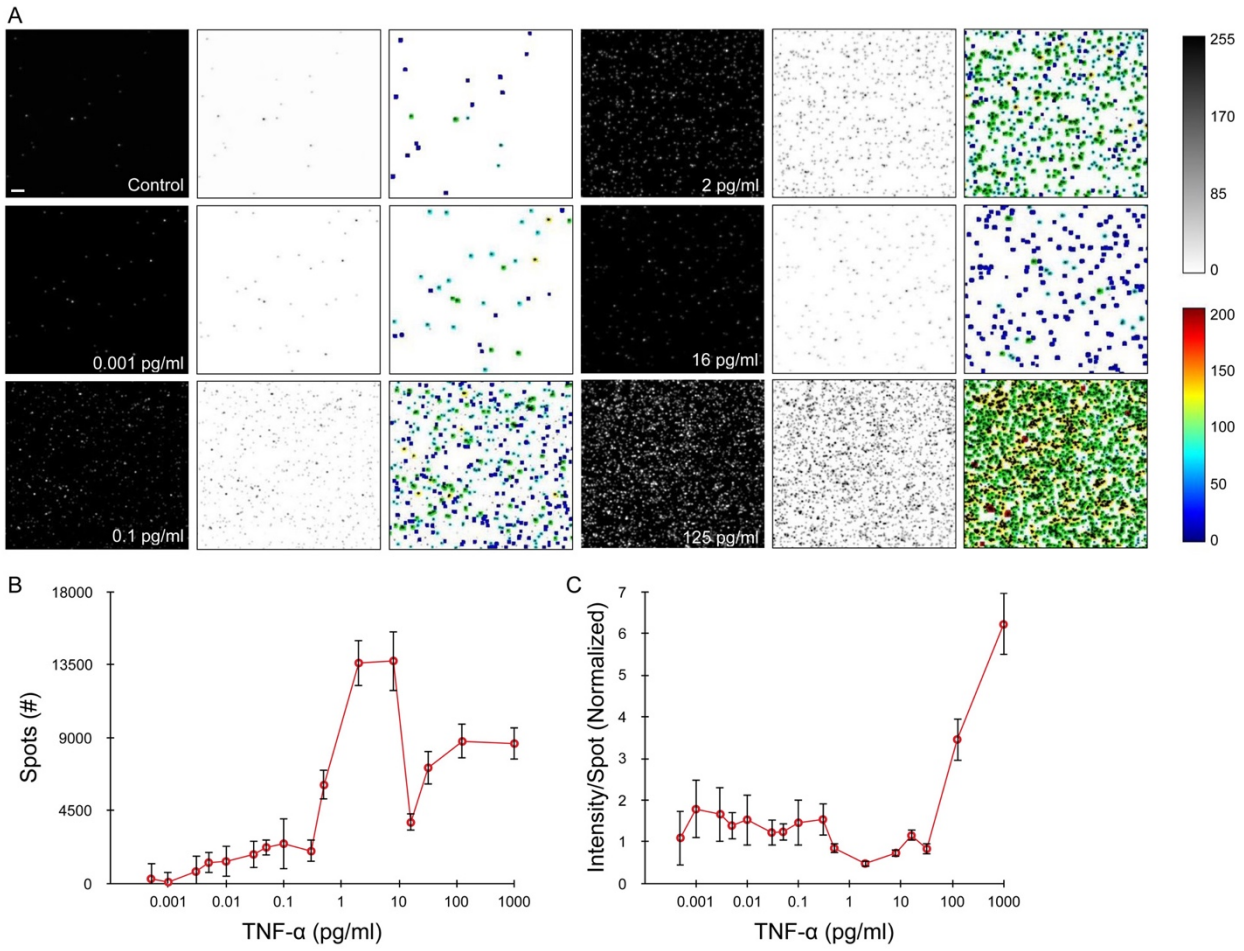

Figure 2.6. Image processing of fluorescent spots obtained with the ChemAmp technique. (A) Representative processed images at select TNF-α concentrations, shown side-by-side with raw fluorescence and grayscale images for comparison. Intensity scalings are indicated by the legends in the lower right hand corner (white to black for grayscale, heat map for processed). (B) Spot number at different TNF-α concentrations. Control value was subtracted. (C) Plot of intensity per spot, normalized to the control (value = 1). Results were close to the control up to 0.3 pg/ml, then decreased below 1 due to quenching. Above 30 pg/ml, QDs were too close together to distinguish. Scale bar is 100 μm. Error bars represent the standard error from at least three independent experiments.

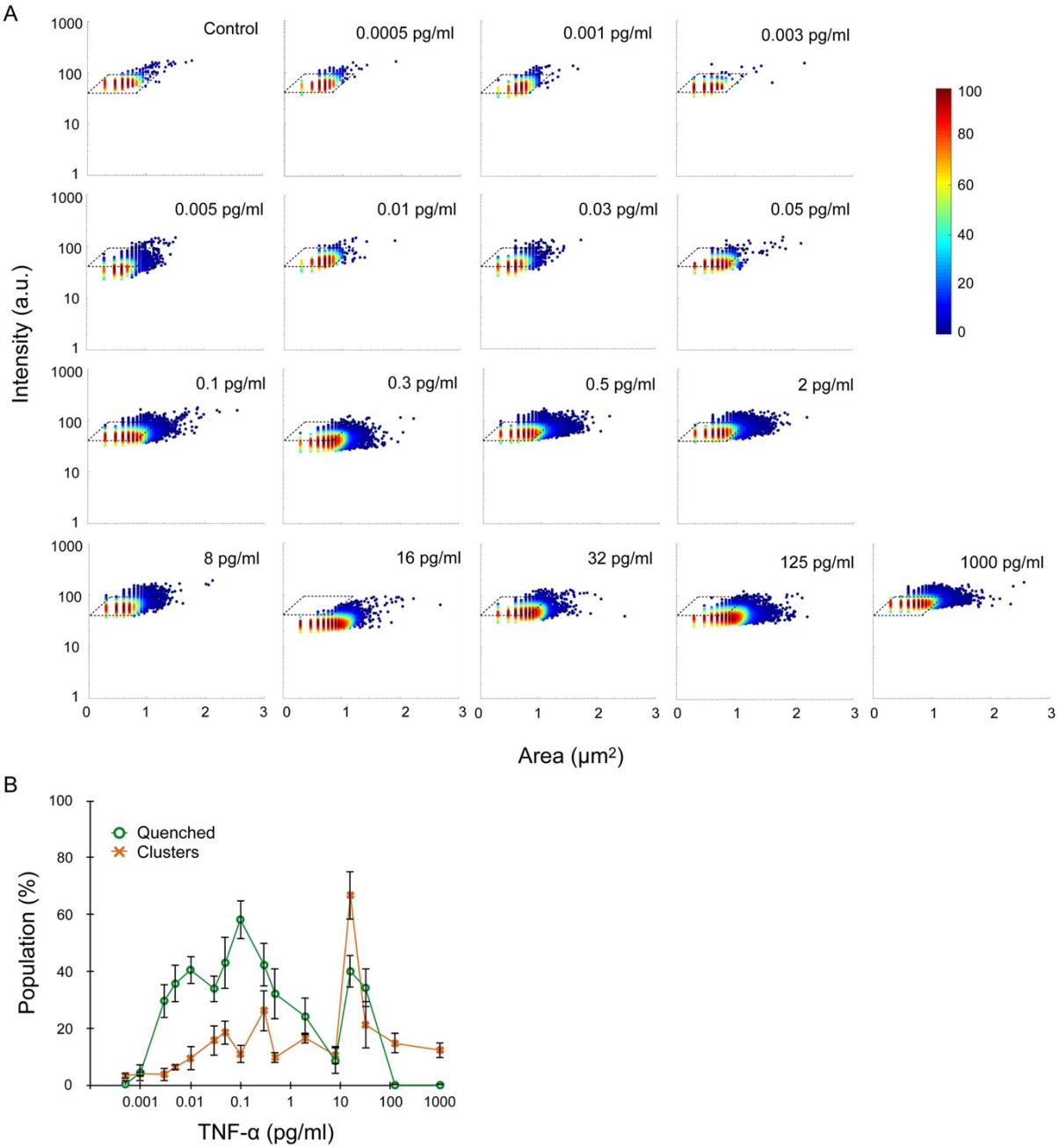

Figure 2.7. Analysis of intensity versus area plots for the ChemAmp technique. (A) Representative density plots of spot intensity vs area for all TNF-α concentrations. (B) Total percentage of quenched and clustered spots plotted versus TNF-α concentration. Error bars represent the standard error from at least three independent experiments.

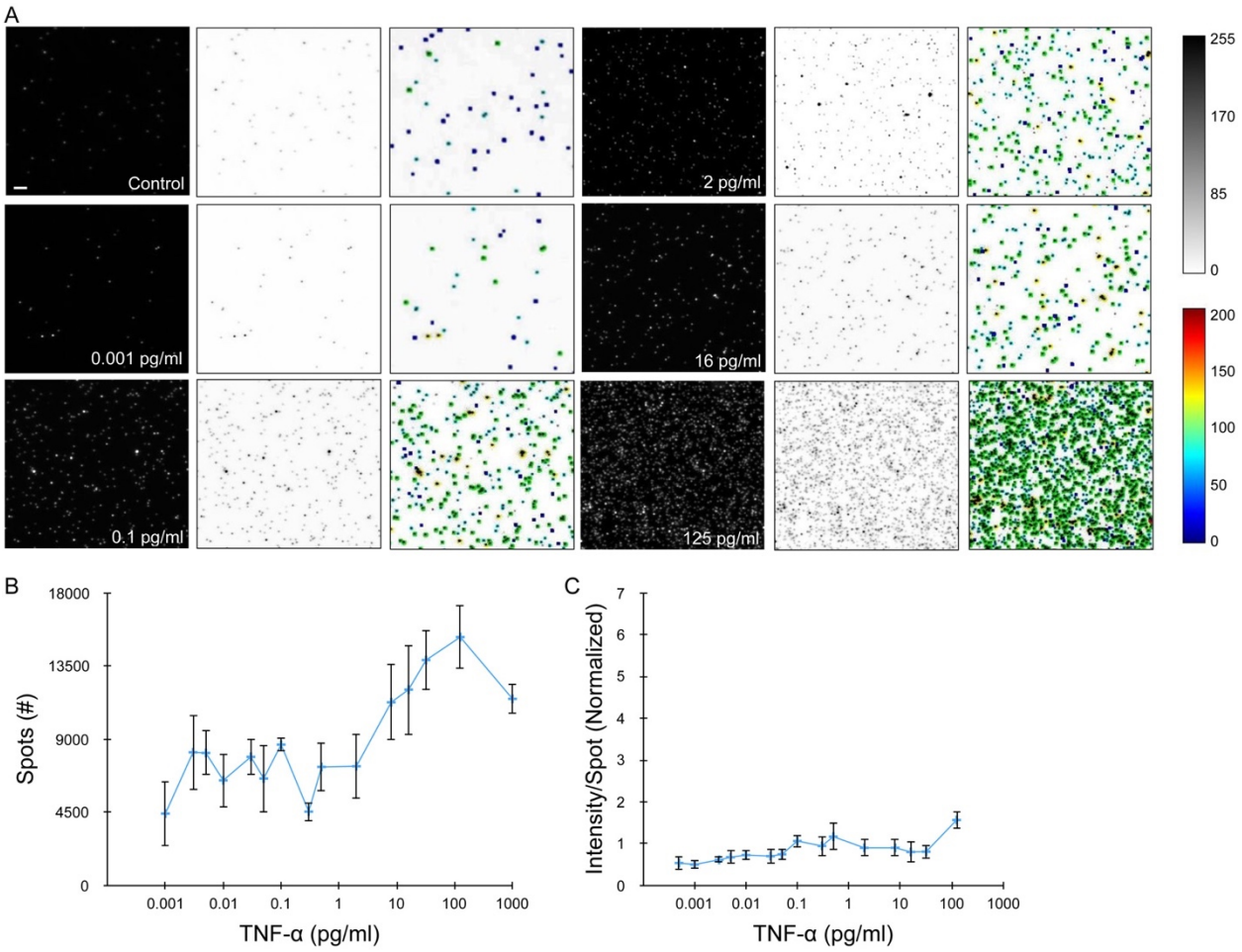

Figure 2.8. Image processing of fluorescent spots obtained with the QD IC. (A) Representative processed images at select TNF-α concentrations, shown side-by-side with raw fluorescence and grayscale images for comparison. Intensity scalings are indicated by the legends in the lower right hand corner (white to black for grayscale, heat map for processed). (B) Spot number at different TNF-α concentrations. Control value was subtracted. (C) Plot of intensity per spot, normalized to the control (value = 1). Results were close to the control up to 0.3 pg/ml, then decreased below 1 due to quenching. Above 30 pg/ml, QDs were too close together to distinguish. Scale bar is 100 μm. Error bars represent the standard error from at least three independent experiments.

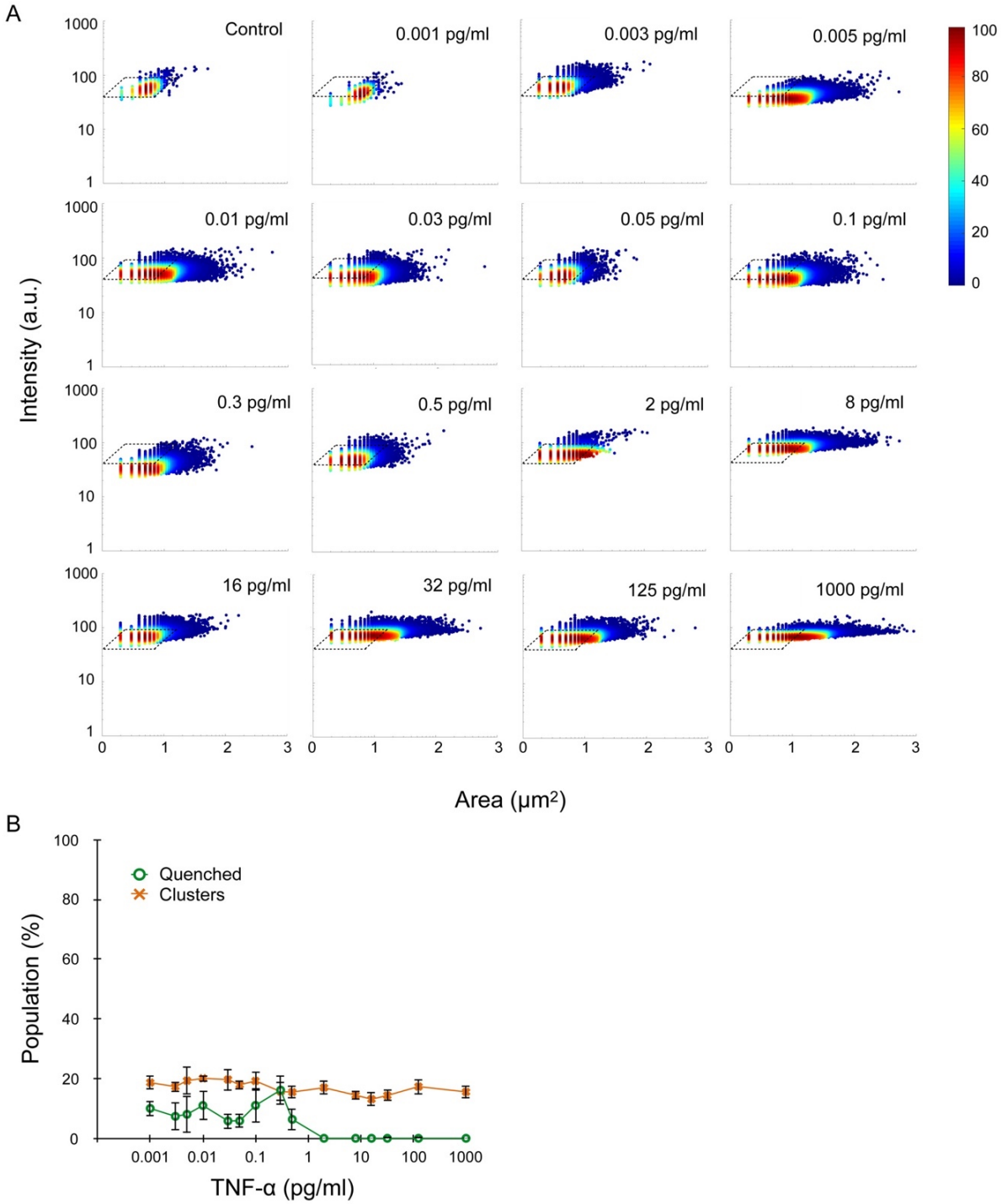

Figure 2.9. Analysis of intensity versus area plots for the QD IC. (A) Representative density plots of spot intensity vs area for all TNF-α concentrations. (B) Total percentage of quenched and clustered spots plotted versus TNF-α concentration. Error bars represent the standard error from at least three independent experiments.

Since this data was likely confounded by two factors, homo-quenching that decreases intensity and clustering that decreased spot number, we directly plotted intensity versus area. Density plots are shown for all TNF-α concentrations in Figure 2.7A. Based on controls, which we believe primarily contained single QDs, we observed that intensity and area were well-correlated, with only a small number of outliers that may have been related to QD blinking. Next we defined a gate characteristic to single QDs, indicated by the polygons in Figure 2.7A. As TNF-α concentration increased, spot distributions shifted to both lower intensity and area (region **a**) or generally larger area (region **b**). We interpreted the shifts into region **a** as corresponding to quenched single QDs and possibly small clusters, and region **b** corresponding to large clusters with varying degrees of quenching. We acknowledge that this is a crude way to assess these effects, and it is possible that some large, highly quenched clusters could be located within the single QD gate or region **a**. However, we found that the percentage of spots within regions **a** (quenched QDs) and **b** (clusters) successfully illustrated key features (Figure 2.7B). For example, quenching was significant even at low TNF-α concentrations, reaching a maximum at 0.1 pg/ml. Clustering was also present at low TNF-α concentrations but rose more slowly, and peaked at 16 pg/ml. Both quenching and clustering decreased at high TNF-α concentrations, although this was likely due to difficulty distinguishing single QDs at such high surface density. The above analysis was repeated for the QD IC, and results are presented in Figure 2.8 and 2.9 As expected, quenching was minimal, as indicated by a relatively flat intensity per spot response curve (Figure 2.8B) and very low percentages of both quenched and clustered spots (Figure 2.9B). Taken together, we believe that the image processing data could

make it possible to calibrate TNF-α concentration for the ChemAmp technique across the fully dynamic range of interest. Specifically, the combination of average intensity, intensity/spot, and ratio of abnormal spot (quenched and clustered) data could be used in a “look-up” table approach (Table 2.1). This would start with a general determination of the concentration range. The low range extends up to ~0.3 pg/ml, and is characterized by intensity/spot values slightly >1 and % quenched values that roughly scale with intensity. The moderate range from 0.3 to 30 pg/ml is dominated by quenching, and as such is characterized by intensity/spot values <1 and generally high numbers of quenching and clustered spots (>10% each). The high range >30 pg/ml has substantially greater intensity and intensity/spot values and very low numbers of quenched spots. Within the low and high ranges, we believe that intensity provides an accurate calibration of TNF-α concentration. The moderate range would be most complex, requiring the combination of intensity, % quenched, and % clustered data to approximate TNF-α concentration. We acknowledge that more detailed investigation will be required to confirm these results and improve robustness so that the ChemAmp technique can be deployed for various applications, including single cell secretion studies.

Table 2.1. Reference table for the QD ChemAmp technique. The combination of all metrics could be used as a unique identifier for TNF-α concentration.

TNF-α (pg/ml)	Intensity (Normalized)	Intensity/Spot (Normalized)	Quenched (%)	Clusters (%)
0	1.0 ± 0.21	1.0 ± 0.00	2.4 ± 0.21	3.0 ± 0.59
0.0005	1.3 ± 0.48	1.1 ± 0.66	2.7 ± 1.29	6.3 ± 1.21
0.001	1.9 ± 0.36	1.8 ± 0.70	6.8 ± 2.97	7.0 ± 1.02
0.003	2.4 ± 0.19	1.7 ± 0.65	32.1 ± 5.89	6.8 ± 2.35
0.005	2.4 ± 0.25	1.4 ± 0.33	38.1 ± 6.57	9.4 ± 1.10
0.01	2.7 ± 0.67	1.5 ± 0.61	43.0 ± 4.77	12.4 ± 4.24
0.03	2.5 ± 0.28	1.2 ± 0.32	36.4 ± 4.79	18.8 ± 5.25
0.05	2.8 ± 0.30	1.2 ± 0.21	45.5 ± 9.06	21.6 ± 4.18
0.1	3.5 ± 0.38	1.5 ± 0.56	60.7 ± 6.78	13.9 ± 3.11
0.3	3.3 ± 0.53	1.5 ± 0.38	44.7 ± 7.68	29.3 ± 7.28
0.5	3.8 ± 0.38	0.8 ± 0.13	34.5 ± 9.00	12.8 ± 2.03
2	4.2 ± 0.48	0.5 ± 0.07	26.6 ± 6.56	19.6 ± 1.92
8	6.4 ± 0.40	0.7 ± 0.10	11.0 ± 4.61	13.5 ± 3.26
16	3.6 ± 0.22	1.1 ± 0.13	42.4 ± 5.85	69.9 ± 8.56
32	4.2 ± 0.42	0.8 ± 0.13	36.7 ± 6.69	24.2 ± 8.23
125	20.6 ± 2.18	3.5 ± 0.51	0.3 ± 0.35	17.7 ± 3.65
1000	36.6 ± 2.57	6.2 ± 0.75	0.1 ± 0.10	15.4 ± 2.64

2.3.4 Detection of TNF-α Secretion from Single Cells

Based on the above findings, we evaluated the QD IC in single cell secretion studies. Experiments were conducted by seeding PMA-treated U-937 cells in an array of 90 × 90 × 43 μm (length × width × height) wells, then quickly adding LPS at 100 μg/ml and sealing the wells with the detection slide. After incubating for 24 h, the

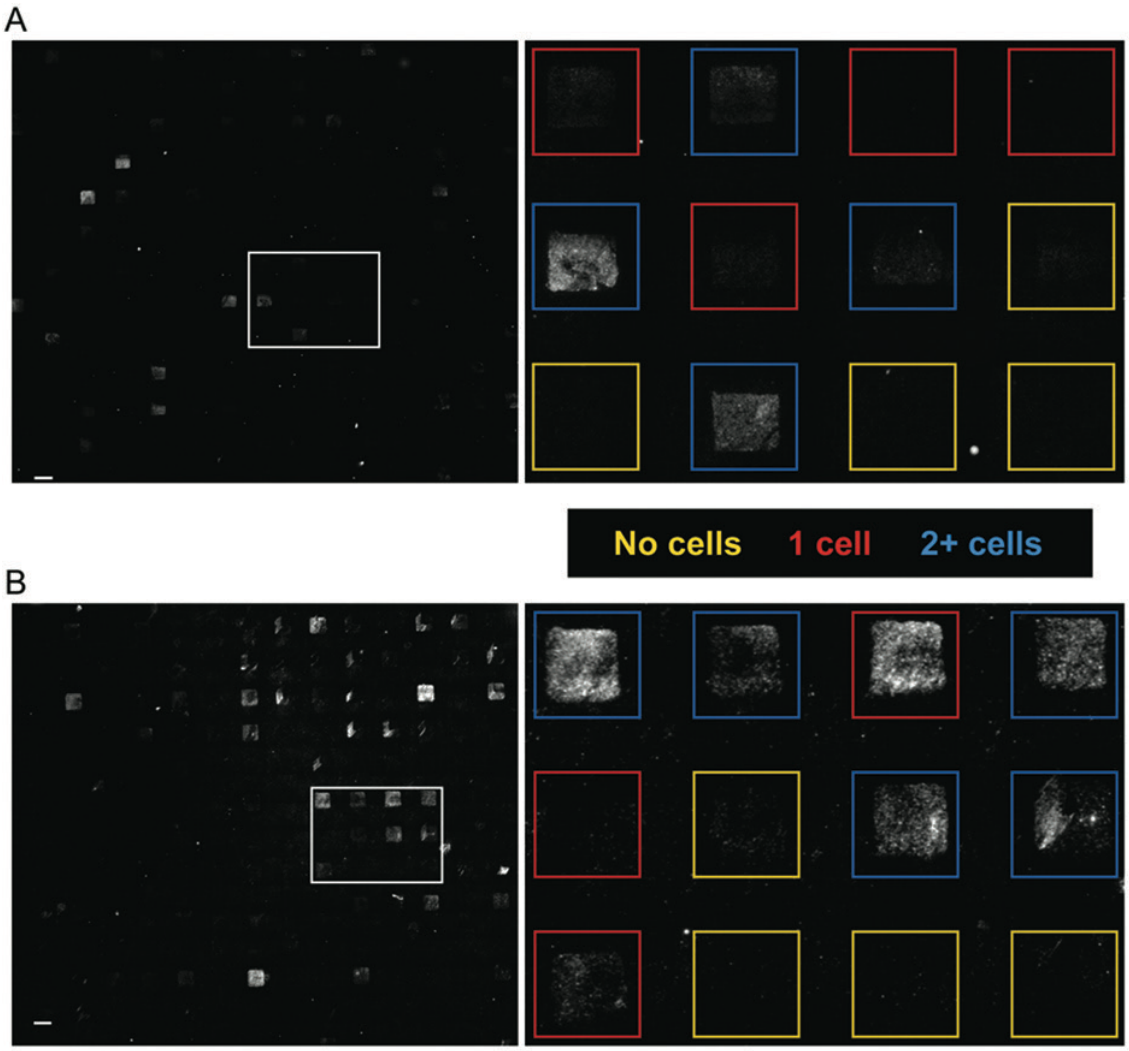

Figure 2.10. Single cell secretion results. (A, B) Representative detection slide images for (A) TMR and (B) QD IC formats. The dashed box indicates the region that was expanded to the right, with individual wells outlined and color coded based on the presence of 0 (yellow), 1 (red), or multiple (blue) cells as determined by phase contrast imaging. Scale bars are 100 μm.

microwells were imaged under bright field to determine the number of cells per well.

Detection slides were then separated, stained with detection antibody coupled to TMR or QD IC, and imaged by fluorescence microscopy. The collection of images obtained under brightfield and fluorescence were separately stitched together, and then superimposed to identify well borders and classify wells as containing no cells, one cell, or multiple cells. Representative images are displayed in Figure 2.10A and 2.10B which qualitatively show that the QD IC provided brighter signals and higher numbers of positive microwells.

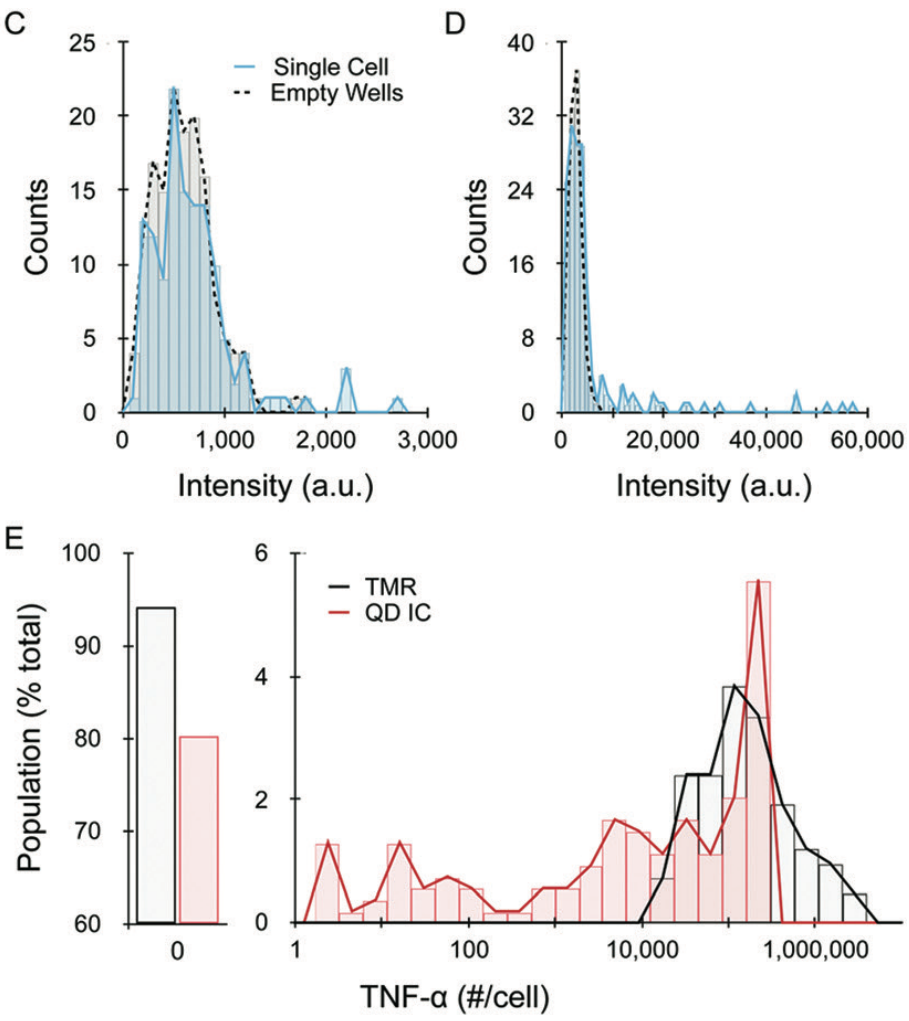

Figure 2.11 Continuation of single cell secretion results. (C, D) Histograms of average well intensity for (C) TMR and (D) QD IC from a representative experimental replicate. Empty well results are indicated by the dotted black line to establish background signals. (E) Histogram of single cell detection results after calibrating TNF-α secretion per cell. Single cells had to secrete >10 000 molecules for detection with TMR, but the QD IC enabled detection down to ~1.3 molecules secreted per cell.

Next, we quantified fluorescence signal for empty and single cell wells, and histograms for a representative experiment are shown for TMR and QD IC in Figure 2.11C and 2.11D, respectively. The single cell wells largely overlapped with empty wells for TMR, indicating that very few single cells secreted enough TNF-α to be detected. For the QD IC, the dynamic range of intensity was much greater, as was the number of single cell wells that exhibited higher signal than empty well controls. To establish a positive detection criterion, we chose the fluorescence intensity that was two standard deviations higher than the mean intensity signal from empty (no cell) wells.[56,59] This resulted in false positive rates of ~3% for both TMR and QD IC cases. We note that it is more common to establish positive detection based on the mean intensity for controls, and then subtract this value from all other conditions. For our data, this approach would have resulted in a false-positive rate of ~45%, and thus our ~3% cut-off was far more stringent. Table 2.2 summarizes results from three independent experimental replicates for the TMR and QD IC cases. After correcting for the false positive rate, signal was detectable from single cells at a rate of 1–13% for TMR and 18–23% for the QD IC, with averages of approximately 6% and 20%, respectively. Thus, we were able to detect TNF-α secretion from >3-fold more single cells using the QD IC. TNF-α concentration was then quantified using calibration curves and regression analysis and converted to

Table 2.2. Detection results for single cell secretion experiments for an organic fluorophore (TMR) and QD IC.

Replicate	TMR (%)	QD IC (%)
1	4.2	18.6
2	12.6	18.2
3	0.7	22.7
Average	5.8 ± 3.5	19.8 ± 1.4

number of molecules secreted per cell (Figure 2.12). Finally, we corrected for our false positive rate by removing cells (~3% of the total population) from the lowest concentrations, and the resulting histograms are displayed in Figure 2.11E. For TMR, cells were only positive if they secreted at least 10,000 molecules (~60 pM or 1 ng ml^{-1}), which is consistent with previous studies.[16,17] For the QD IC, ~50% of positive cells secreted >10,000 molecules, and this population had a similar distribution as TMR, except for an abrupt truncation at ~400,000 molecules per cell (~1500 pM or 25 ng ml^{-1}) that was most likely due to QD homo-quenching. The remaining positive cells secreted TNF-α at levels that could not be detected by TMR, extending all the way down to 1.3 molecules per well (~5 fM or 0.1 pg ml^{-1}). We note that obtaining near single molecule resolution is reasonable since 5 fM is ~50-fold higher than the detection threshold determined for the QD IC (180 aM, see 0.1 pg/ml results in Figure 2.4). However, it is important to note that these numbers refer to captured TNF-α. At this time, we cannot confirm the number of molecules secreted, as this is a function of antibody binding properties and possibly TNF-alpha oligomerization. We can conclude that our QD-based imaging method provides the maximum detection sensitivity possible for single cell secretion studies. Moreover, there is considerable detection potential, as much as 100-fold, remaining to be leveraged for multiplexing purposes. Methods that pattern different capture antibodies into barcodes require larger wells, which dilutes analyte concentration.[55,56] Alternatively, multiple capture anti- bodies can be conjugated to the same surface to enable detection by a set of probes with distinct emission spectra, thus diluting the density of each capture antibody per well.[18,56] One or both of these multiplexing strategies could be pursued using our QD-based format while still

maintaining detection sensitivity below 5 fM. We do note that the simultaneous use of multiple QDs, even in the IC format, would require careful control of resonance energy transfer (homo-quenching and FRET). We also conclude that ~80% of the single cells did not secrete more than one molecule of TNF-α. This corroborates previous work that has established a key role for small numbers of precocious or first responder cells in stimulating larger populations of dendritic cells or macrophages through paracrine signaling.[17,46,78,79] To further confirm this interpretation, we performed bulk ELISA experiments using PMA-activated, LSP-stimulated U937 cells and found that secretion rate varied with cell seeding density, and was at least 1000-fold higher on a per cell basis than single cell studies (Figure 2.13).

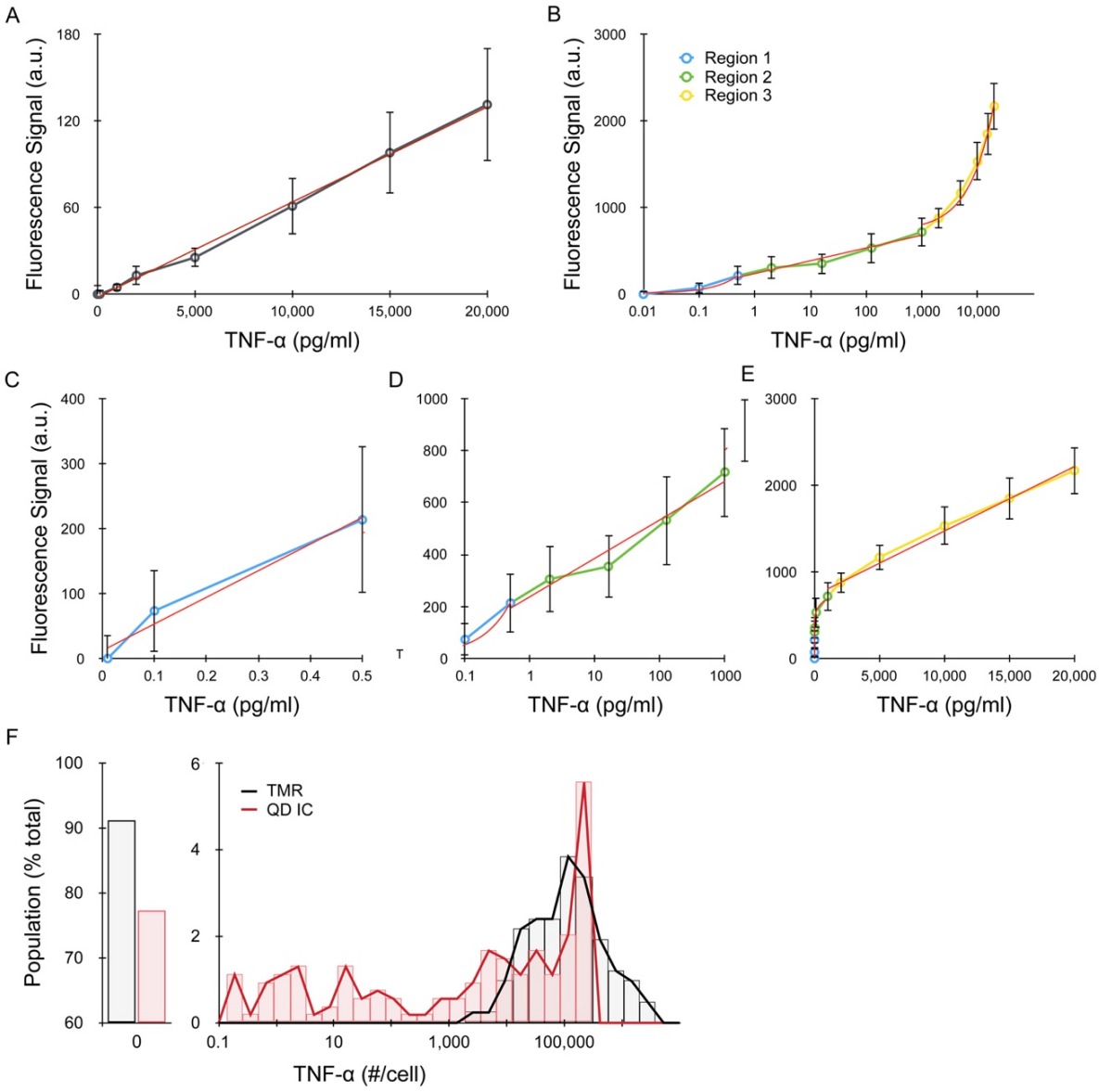

Figure 2.12. Calibration of TNF-α for single cell secretion studies. (A,B) Standard curves obtained for (A) TMR and (B) QD IC. The fits used to calibrate concentration in single cell secretion studies are shown in red. (C-E) Three separate fittings were used to encompass the full dynamic range of the QD IC, including (C) low, (D) moderate, and (E) high TNF-α ranges. (F) Histogram of single cell secretion after calibrating TNF-α concentration and number per cell. This data includes false-positives (3% of total population) that were removed from Fig. 4E in the main text. Error bars represent the standard error from at least three independent experiments.

To assess potential paracrine effects that would affect bulk populations, but not

single cells, we performed experiments in which PMA-differentiated, LPS-activated U937 cell density was varied from 1,000 to 5,000 cells per well. ELISAs were performed on supernatants after 3 and 6 hours incubations with LPS, and results were calibrated to TNF-α concentration per well (Figure 2.13A) and converted to number of molecules secreted per cell (Figure 2.13B). TNF-α concentration increased with both time and cell density, as expected. Interestingly, the number of TNF-α molecules secreted per cell also increased in a dose dependent manner with cell density, particularly for the 3 hour data. We could not assess whether this trend extended to lower densities because ELISA signal was undetectable above background. Notably, the average secretion rate for the 1,000 cell/well and 3 h incubation time condition was >100,000 molecules/cell. This was orders of magnitude greater than single cell studies for both TMR and QD IC assays, which had average secretion rates of approximately 230 and 50 molecules/cell, respectively. These average secretion numbers include the zero-count population. These data add to a growing body of literature suggesting the importance of paracrine signaling in the activation of macrophage populations. Using our QD-based system, we can now confirm that most of the cell population did not respond to LPS at all, while a significant sub-population (~10%) responded weakly by secreting ~2 to 10,000 TNF-α molecules. We will seek to confirm these findings using other cell macrophage cell models, and potentially detection techniques such as single cell RNA sequencing.

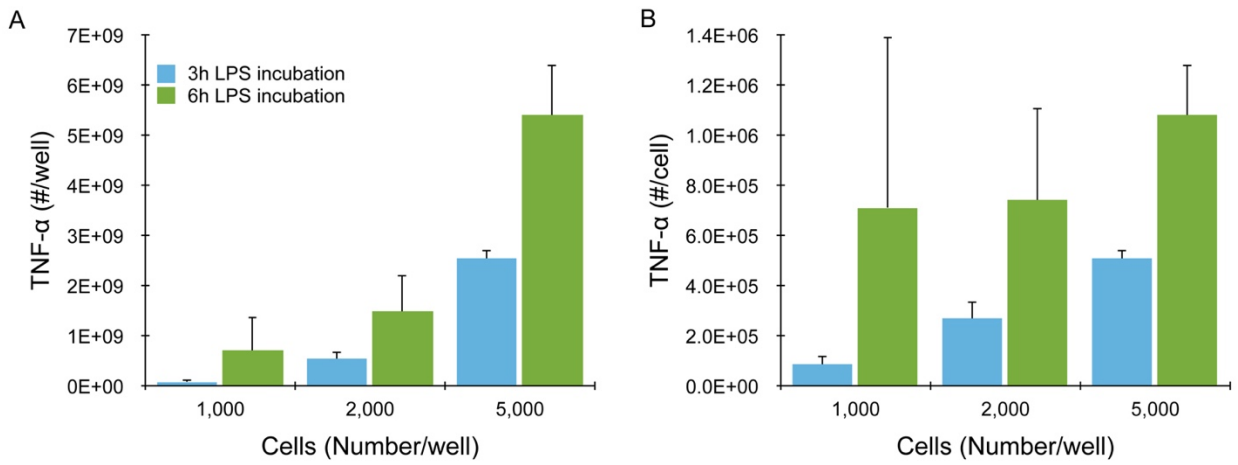

Figure 2.13. Bulk TNF-α secretion experiments at different cell densities. U937 cells were plated at 1,000, 2,000, or 5,000 cells/well, differentiated with 50 ng/ml PMA, and stimulated with 100 ng/ml LPS for 3 or 6 hours. TNF-α was quantified by ELISA, and results are presented as TNF-α (A) concentration and (B) molecule number per cell. TNF-α secretion increased on a per cell basis with time and seeding density. Error bars represent the standard error from at least three independent experiments.

2.4 Conclusion

In this work, we advanced the detection sensitivity of QD sandwich immunoassays for soluble proteins using single QD imaging and amplification of binding using bioorthogonal chemical reaction, reaching a lower threshold of 60 aM. To our knowledge, this is the lowest detection threshold that has been achieved using a non-enzymatic, probe-based method. Our detection format used a simple sandwich immunoassay and standard fluorescence microscope, and thus comes with additional benefits such as assay speed, simplicity, large dynamic range, and the spatial resolution essential for single cell secretion studies. The QD-based detection method increased the number of single cells that could be interrogated for TNF-α secretion by 3-fold in comparison to an organic fluorophore, which was achieved by extending

detection range down to nearly 1 molecule captured per microwell. We acknowledge that organic fluorophore results could be improved using amplification methods such as multi-round labeling,[54] FLUOROSpot, or ultrafast polydopamine deposition,[62] but these assays are more complex, may be difficult to quantitate, and will still not reach the detection sensitivity of our one-step, non-enzymatic, QD-based assay. Presumably, comparable results could be achieved using a single fluorophore imaging technique such as super resolution microscopy, but this would significantly increase imaging time, complexity, and cost. This study will significantly improve the detection capacity of single cell secretion studies, enabling interrogation at earlier time points and/or lower secretion rates. Future work will investigate the implications of this new capability in biologically relevant models, with a particular focus on assessing macrophage polarization under different microenvironmental stimuli such as well size, shape, and extracellular matrix type using our three-component well system,[17] as well as analyzing immune cells isolated from various disease models including solid tumors. We will also adapt the technique to diverse soluble protein targets to validate these findings and enable multiplexing capabilities. We acknowledge that unforeseen challenges may be encountered when we move to in vivo applications, such as oligomerization, or different targets, such as variable antibody binding affinities. Finally, we will explore ways of directly assessing or eliminating the homo-quenching effects that we believe complicated analysis of the ChemAmp technique so that we can leverage the lowest detection threshold possible.

CHAPTER 3: Quantum dot-based multiplexed detection of proteins secreted from single cells

3.1 Introduction

Cells from any given population tend to have unique phenotypic and behavioral characteristics. Growing evidence showing that there is cell-to-cell variability within a genetically identical cell population has shown that cellular heterogeneity is present in most cell populations.[56,80] Specially in the immune system, where immune responses are mediated by many effector proteins, such as cytokines, chemokines, and growth factors, secreted by single cells. These secreted proteins are important regulators that facilitate the cell-to-cell communication that affects cellular behavior and paracrine/autocrine signaling.[55] Understanding the secretome signature of a cell population during healthy and diseased microenvironments can lead to greater insights into cell development and more effective therapeutic treatments.[81]

Current techniques that can monitor secreted proteins for single cells without compromising cell viability, detection sensitivity, and assay simplicity are limited. Enzyme-linked immunospot (ELISpot) assay measures the frequency of cytokine secretion from single cells using immunosandwich-based detection, where spots correlate to the magnitude of captured proteins secreted by neighboring cells. In a subtle variation to ELISpot, fluorescence enzyme-linked immunoSpot (FLUOROSpot) uses fluorescent dyes instead of colorimetric enzymatic reactions to assess the secretion of more than one protein. Even though both techniques offer several advantages, such as detection sensitivity and multiplexing adaptability for the FLUOROSpot assay, protein secretion can't be correlated to the originating cell or

quantified, and multiplexing is limited to 2-4 proteins.[82] Intracellular cytokine staining (ICS) flow cytometry is a common alternative to quantify secretion from single cells, but protein secretion must be blocked, and cells fixed before protein measurement.[83] Recent advances in microfabrication have enable the development of micro-technology; nano-size well arrays that can isolate and interrogate secreted proteins from single cells.[9,16,84–86] In this technique, a glass slide containing immobilized antibodies is used to seal the wells and capture secreted proteins from single cells, followed by quantification by immunofluorescence detection. Recently, we increased detection sensitivity for soluble TNF-α protein using this technique by switching the probe from a fluorophore to a quantum dot (QD) (Chapter 2). We were able to improve detection threshold to 60 aM by using QD imaging and *trans*-cyclooctene/tetrazine bioorthogonal signal amplification. QD are extremely bright and photostable nanoparticles, with broad absorption and narrow emission wavelengths, and size-dependent light color emission. These properties make QD excellent probes for adapting multiplexing capabilities to single cell protein detection microarrays.[87,88] We have already demonstrated that the modification of detection antibodies with QD has great potential to reach low detection limits; thus, we can incorporate multiplexing capabilities of the detection system by conjugating detection antibodies with multi-color QD probes.

Here, we report the simultaneous sensitive detection of four soluble proteins, monocyte chemoattractant protein 1 (MCP-1), transforming growth factor beta (TGF-β), interleukin 10 (IL-10), and tumor necrosis factor-α (TNF-α), secreted from single immune cells using multi-color QD probes. In this work we focus on studying macrophages, which are known to adopt a spectrum of phenotypes that generally fall

into pro-inflammatory (M1) or pro-healing (M2) subtypes depending on their tissue microenvironment. Macrophage activation is characterized by secretion of specific proteins, and as such, we chose to study two for each subtype: MCP-1 and TNF-α for pro-inflammatory and TGF-β and IL-10 for pro-healing polarization. First, we optimize the assay's ability to reach low detection limits on glass slides by performing calibration curves using the same QD immunoconjugate (IC) 605 nm emission probe. From these results, we find that intensity signal was not affected by diluting the availability of capture antibody on the slide by 4-fold. Next, we generate protein standard curves on glass slides at optimal QD concentrations using the multi-color protein/QD pairs, where we see detection limits similar to our previous work at around 1 fM or one protein secreted per cell in single cell experiments. We further evaluate if there is any signal crossover from neighboring emission QD, where we calculate the percent bleed-through to be consistently below 5% for every emission window. Next, we assess if QD quenching is affecting the signal from QD with neighboring emission channels, where we conclude that the intensity signal is not affected. Lastly, we perform single cell experiments using phorbol 12-myristate 13-acetate (PMA) differentiated, lipopolysaccharide (LPS) and/or interleukin 4 (IL-4) activated U-937 cells. We find that protein secretion under each stimulation condition changes as expected, where LPS mostly increases secretion of pro-inflammatory proteins and addition of IL-4 further improves the secretion of pro-healing proteins. We are also able to assess the behavior of protein secretion at levels below 60 pM, which is the current detection limit for most multiplexing fluorophore immunoassays. Based on our findings, we conclude that our

QD-based imaging method is able to successfully detect the simultaneous secretion of four proteins in single cell experiments.

3.2 Methods

All chemicals were purchased from Sigma-Aldrich (St Louis, MO) unless otherwise noted. Sulfo-NHS-LC-Biotin, sulfo-SMCC (sulfosuccinimidyl 4-(N-maleimidomethyl)cyclohexane-1-carboxylate), primary amine-terminated quantum dots (Qdot 525, 565, 605, and 655 ITK Amino PEG), and Neutravidin were purchased from Thermo Fisher Scientific (Waltham, MA). Recombinant human monocyte chemoattractant protein 1 (MCP-1), transforming growth factor-β (TGF-β), interleukin 10 (IL-10), and tumor necrosis factor-α (TNF-α) and matched monoclonal mouse antibodies for human MCp-1, TGF-β , IL-10, and TNF-α sandwich immunoassays (IgG, clones 2H5 and 5D3-F7; IgG1κ, clones TW7-7H4 and TW4-6H10; IgG1κ , clones JES3-9D7 and JES3-12G8; IgG1κ, clones MAb1 and MAb11, respectively) were purchased from BioLegend (San Diego, CA).

3.2.1 Immunoconjugate (QD IC) Conjugations

Anti-MCP-1 (2H5, 5D3-F7), anti-TGF-β (TW7-7H4, TW4-6H10), anti-IL-10 (JES3-9D7, JES3-12G8), and anti-TNF-α (MAb1, MAb11) capture and detection antibodies (BioLegend) were buffer-exchanged into PBS using Zeba spin desalting columns prior to modification. Biotinylated capture antibodies and QD immunoconjugates (IC) were modified, as described previously[91]. Briefly, capture antibodies were reacted to 5 molar equivalents of sulfo-NHS LC Biotin in PBS containing 10% dimethylformamide (DMF)

and 0.1 M $NaHCO_3$ (pH 8.4). In a similar manner, detection antibodies were modified with 30 molar equivalents of NHS-TCO. All modified proteins were purified using Zeba spin desalting columns (Thermo Fisher). Antibody concentrations were determined by absorption measurement using a NanoDrop 2000 spectrophotometer. Amine-terminated QD were modified with NHS-tetrazine using 0.8 nmoles of amine-QD (Thermo Fisher, emissions 525, 565, 605, and 655 nm) and 500 molar equivalents of NHS-tetrazine in PBS containing 5% DMF and 0.01 M $NaHCO_3$. Reaction was incubated for 3 h at room temperature, and tetrazine-QD were purified into PBS using an Ultra-4 centrifugal filter with 10 kDa MWCO. QD immunoconjugates (IC) were prepared by reacting 0.15 nmole tetrazine-QD with 200 µg TCO-modified detection antibody (prepared with 30 molar equivalents TCO-NHS) in 1 ml of PBS containing PBS+ for 3 h at room temperature. QD ICs were purified using Sephacryl S-400 (GE Healthcare) gel filtration media on an AKTA Pure FPLC system (GE Healthcare). Final concentrations were determined by absorption measurements and calibration using the QD stock solution.

3.2.2 Fabrication of PDMS Microwell Arrays

PDMS microwell arrays were fabricated as described previously[89]. Briefly, SU-8 50 photoresist (MicroChem, MA) was spin-coated onto a 3″ silicon wafer to get a 80 mm thick layer. After baking at 95 °C for 2 h, the wafer was placed under a mask containing clear rectangles (90 µm × 90 µm) and was exposed to UV light. After 10 minutes, the wafer was submerged in SU-8 developer for 5 minutes to clean unpolymerized photoresist. Wafer was then baked at 200 °C for 30. PDMS and curing agent (Dow Corning, MI) were mixed in 10:1 ratio and poured onto the silanized silicone master to

produce the microwell array. The microwells measured 90 μm × 90 μm × 43 μm, for a volume of ~350 pl. Arrays were then degassed, cured in oven at 65 °C, and sterilized with 70% ethanol.

3.2.3 U-937 Cell Culture and Differentiation

The pro-monocytic, human myeloid leukemia cell line U-937 was obtained from ATCC (Manassas, VA) and cultured as recommended in RPMI 1640 medium supplemented with 2 mM L-glutamine, 10 nM HEPES, 1 mM sodium pyruvate, 4.5 g/L glucose, 1.5 g/L sodium bicarbonate, and 10% fetal bovine serum (Thermo Fischer Scientific, MA). U-937 cells were seeded for single cell experiments as described previously[91]. Briefly, U-937 cells were seeded at density of 500 000/ml in 12-well plates, differentiated with 50 ng/ml PMA for 48 h and allowed to rest for 24 h in culture media. On the day of the experiment, the cells were treated with 4% Trypsin EDTA (Thermo Fisher Scientific, MA) to detach cells from the flask, seeded onto the PDMS microwells by centrifuging at 700 rpm for 5 min, and incubated for at least 1 h before stimulation with 100 ng/ml LPS or 10 ng/ml interleukin 4 (IL-4). Detection glass slides were then inverted over the top of the microwells and sealed using a customized acrylic housing. Protein was allowed to secrete for 24 h at 37 °C, followed by imaging cells under bright field using an Olympus IX83 inverted microscope (Olympus, Japan) and a 10x objective (NA 0.3, Olympus) to determine the number of cells present within each microwell.

3.2.4 Assess Protein Detection by Fluorescence Imaging

Standard 25 mm x 75 mm glass microscope slides were cleaned, silanized, and treated with activated neutravidin, as previously described[89]. Briefly, slides were cleaned using Piranha solution (3% H_2O_2 and concentrated H_2SO_4 at 1 : 2 volume ratio) for 30 min, rinsed with double deionized water H_2O (dH_2O), and dried in an oven for 1 h at 100 °C. Slides were then submerged in a solution of 4% (3-mercapto-propyl)trimethoxysilane in 100% ethanol for 1 h, rinsed with ethanol, and dried in the oven for 30 min. Silanized glass slides were stored in a desiccator until later use. Prior to calibration experiments, a 50 microwell silicon gasket (Grace Bio-Labs) was placed onto the silanized glass slide and 5 µl of PBS containing 1 mg/ml maleimide-modified neutravidin was added to each well. After reacting for 2 h at room temperature, wells were washed with PBS, biotinylated capture antibody either one at a time at 10 µg/ml in PBS or all anti-MCP-1, anti-TGF-β, anti-IL-10, and anti-TNF-α antibodies at 2.5 µg/ml in PBS each were incubated for 2 h, and wells were blocked with PBS+ for 15 min at room temperature. Purified protein (MCP-1, TGF-β, Il-10, and/or TNF-α) was then added at concentrations ranging from 1 fM to 100,000 fM in PBS+ and incubated for 2 h at room temperature. Lastly, QD IC detection antibodies (anti-MCP-1, anti-TGF-β, anti-IL-10, and anti-TNF-α) were incubated at a final concentration of 20 nM (anti-IL-10 and anti-TNF-α) and 100 nM (anti-MCP-1 and anti-TGF-β) for 30 min at room temperature and washed with PBS+. Silicon gasket was then removed and glass slides sealed with a cover slip in 1X PBS for imaging. For single cell secretion studies, a 2 cm × 2 cm square region was outlined with a grease pen on silanized detection glass slides, coated with 125 µL of 1 mg/ml maleimide-modified neutravidin for 2 h, rinsed, blocked with 200 µL

of PBS+ for 15 min, incubated with 125 µL of anti-MCP-1, anti-TGF-β, anti-IL-10, and anti-TNF-α (2.5 µg/ml each) biotinylated capture antibody for 2 h at room temperature, and treated with PBS+ for 15 min at room temperature. After 24 h, the silicon gasket was carefully separated from the glass slide, the slide was washed with 200 µL ice cold PBS+, and stained with QD IC (anti-MCP-1, anti-TGF-β, anti-IL-10, and anti-TNF-α at final concentration of 20 nM for each detection QD IC antibody) for 30 min. After additional washing with ice cold PBS+, a cover slip was mounted in preparation for imaging.

3.2.5 Imaging and Analysis

Glass slides were imaged using an Olympus X83 inverted microscope as described previously[89]. Briefly, single-band QD filter sets optimized for 525, 565, 605, and 655 nm emission (415–455 nm single band exciter for all filter cubes, and 510 and 540 nm for QD525, 550 – 580 nm for QD565, 590–620 nm for QD605, and 640-670 nm for QD655, Semrock and Chroma), and 40x oil-immersion objective (NA 1.3, Olympus). Images were captured using an Orca-R2 CCD camera (Hamamatsu Photonics) and mManager control software for at least five fields of view per sample using 500 ms integration times. ImageJ software was then used to quantify mean fluorescence intensity. For single cell studies, the complete series of brightfield or fluorescence images were stitched together using Fiji software and the Grid/Collection Stitching plug-in and analyzed. Microwell locations were then defined in the stitched fluorescence images by aligning with the stitched bright field images using the built-in mask, selection, and ROI manager tools. Afterwards, the defined ROIs for empty and single

cell wells were superimposed on the fluorescence images from the detection glass slides and the mean intensity for each ROI was obtained with the built-in multi-measure tool in ImageJ. The spectral overlap or bleed-through signal was first subtracted from the mean intensity from both empty and single cell wells. Matlab was then used to generate mean intensity histograms for single cell and empty well counts, as well as to classify the protein secretion profile based on the threshold, two standard deviations above the background mean. Finally, protein secretion for the positive population was calibrated from intensity measurements obtained using soluble protein. Matlab was also used to generate 3D scatter plots.

3.3 Results

3.3.1. Single Target Detection Using QD ICs

We first assessed protein detection sensitivity on glass slides using fluorescence imaging and 605 nm emission QD detection. We were interested in evaluating intensity

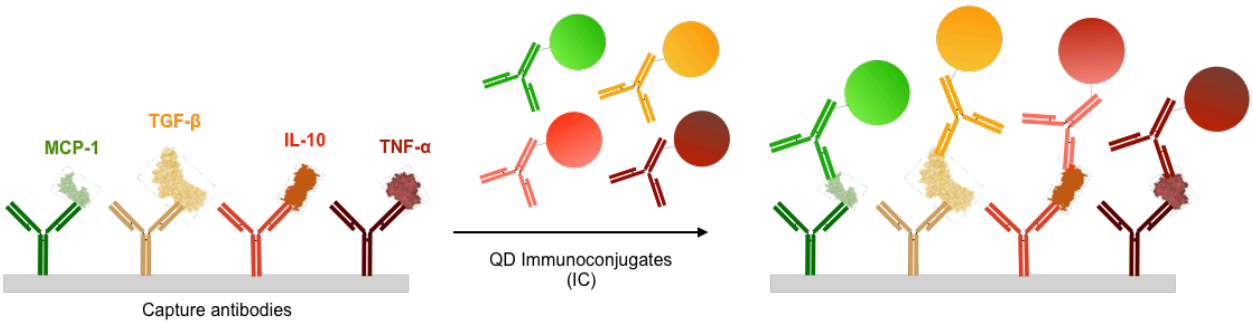

Figure 3.1. Detection of purified soluble protein using quantum dot immunoconjugates (QD ICs). Schematic of sandwich detection scheme using biotinylated capture antibody bound to the detection glass slide, soluble protein, and detection QD IC antibody, where green is TGF-β, orange is MCP-1, red is TNF-α, and blue is IL-10 detection.

signal from detection glass slides reacted with a single capture antibody or with all four (multiple) capture antibodies. These experiment where done to verify if the intensity

signal was affected by diluting the capture antibody availability on the slides by 4-fold, as well as assess capture antibody binding kinetics efficiency in recognizing protein targets. To do so, glass slides were silanized, covalently modified with neutravidin, and reacted with biotinylated capture antibody. For single capture antibody conditions, only one capture antibody was incubated at a time; whereas for the 4 capture antibodies condition, equal amounts (2.5 μg/ml) of MCP-1, TGF-β, IL-10 and TNF-α capture antibodies were incubated. Afterwards, purified recombinant human protein (MCP-1, TGF-β, IL-10, or TNF-α) at concentration ranging from 1 to 10,000 fM was added, followed by QD ICs (QD pre-conjugated with detection antibody) to achieve immunoassay detection (Figure 3.1). Slides were imaged under a traditional fluorescence microscope using a QD605 filter cube and the same parameters optimized in our previous work (Chapter 2). After measuring mean intensity and subtracting the background signal, we get the calibration curves in Figure 3.2. The fluorescence intensity signal from single and all 4 capture antibodies for the detection of MCP-1 (Figure 3.2A), TGF-β (Figure 3.2B), IL-10 (Figure 3.2C), and TNF-α (Figure 3.2D) proteins was consistently within standard error for both cases, eluding to the fact that

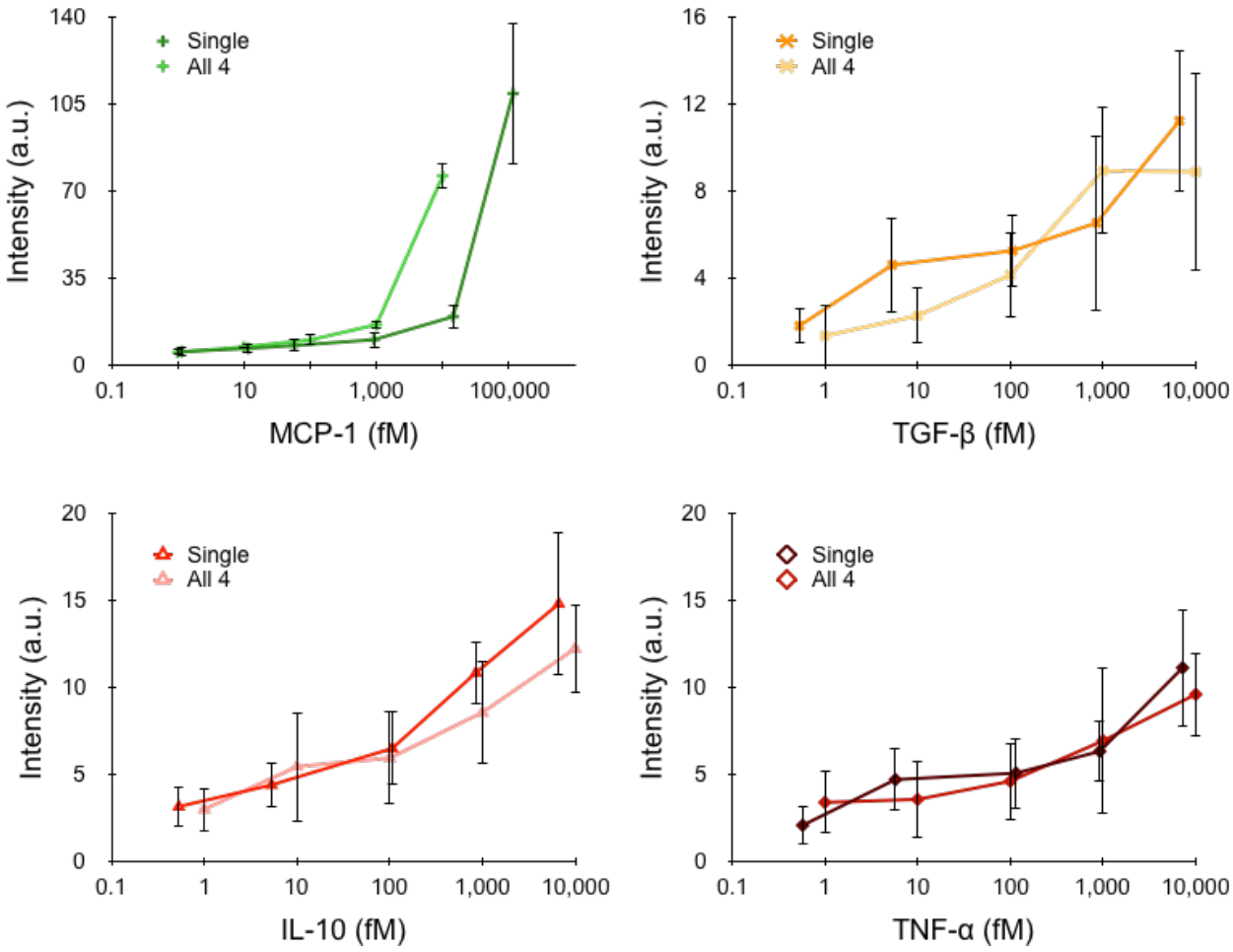

Figure 3.2. Single target detection using 605 nm QD IC. Average intensity, after background subtraction, for (A) MCP-1, (B) TGF-β, (C) IL-10, and (D) TNF-α 605 nm QD ICs. The fluorescence intensity signal from single and multiple capture antibodies detection was similar to each other. Thus, diluting the capture antibody availability on the detection slide did not affect intensity signal. Furthermore, detection threshold was at least 1 fM for all QD ICs. Error bars represent the standard error from at least three independent experiments.

diluting the capture antibody availability on the glass slides did not affect intensity signal, as well as the capture antibody binding kinetics for their respective protein was efficient. Detection threshold, which corresponds to two standard deviations above the mean intensity of the control, is at least 1 fM for all proteins. Detection limit of 1 fM corresponds to the ability of the assay to measure the secretion of only one protein secreted per cell in single cell experiments using our microarray system. Glass slides for imaging experiments moving forward are modified with four capture antibodies, as seen in the schematic in Figure 3.1.

Next, we conjugated each protein detection antibody with multi-color QD probes as follows, MCP-1/525 nm QD, TGF-β/565 nm QD, IL-10/605 nm QD, and TNF-α/655 nm QD. QD concentration was first optimized using 100,000 fM of protein; we found that

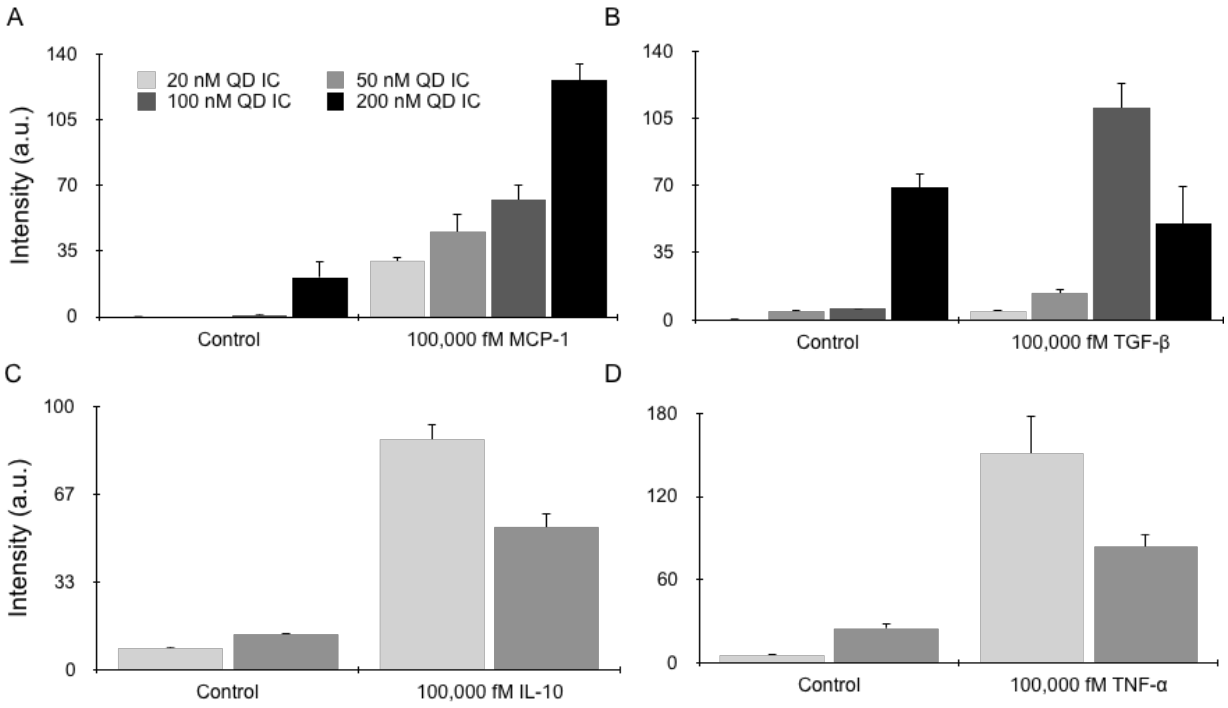

Figure 3.3. Optimal QD concentration. Intensity signal results for (A) MCP-1/525, (B) TGF-β/565, (C) IL-10/605, and (D) TNF-α/655 QD ICs controls and 100,000 protein concentration. The maximum signal was obtained at 20 nM QD for IL-10/605 and TNF-α/655 and at 100 nM for MCP-1/525 and TGF-β/565. Error bars represent the standard error from at least three independent experiments.

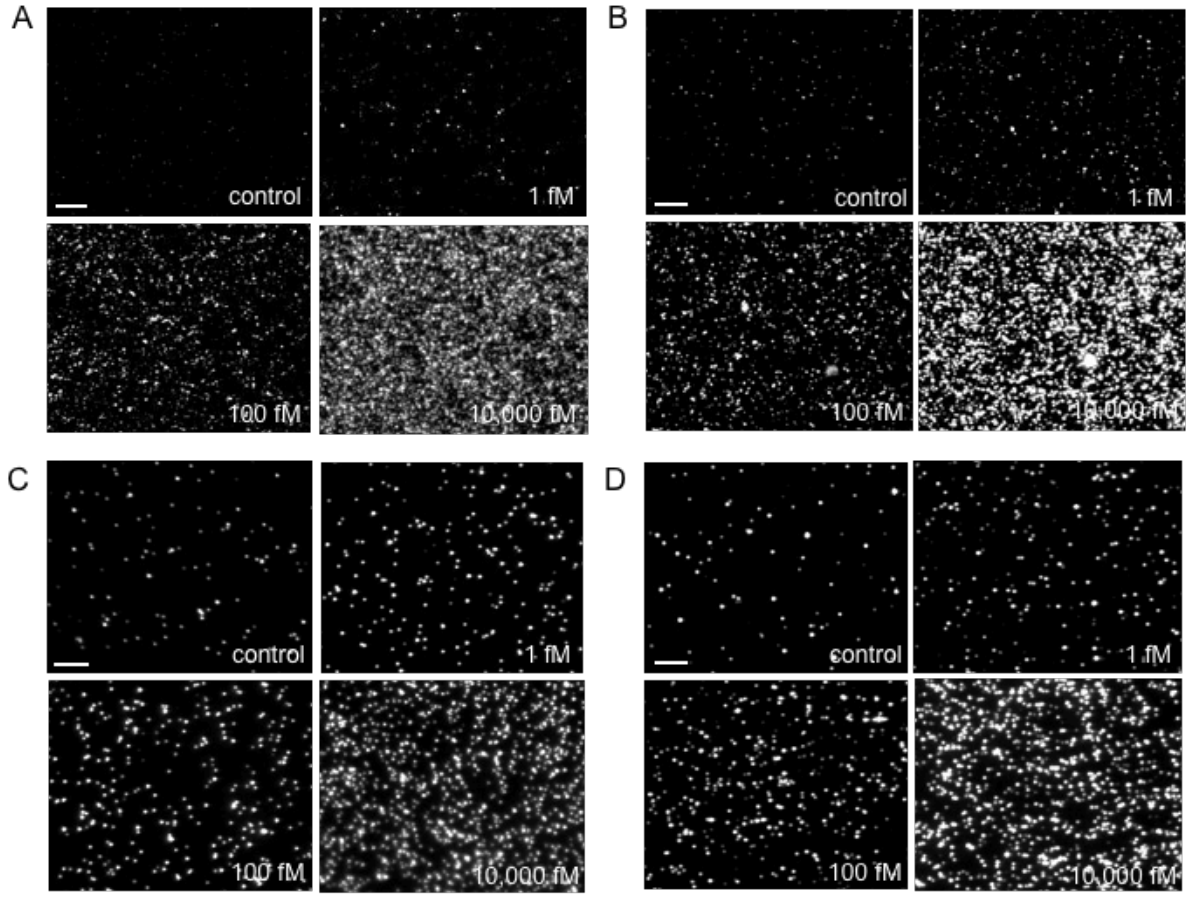

Figure 3.4. QD fluorescent images. Representative fluorescent images at increasing protein concentration for (A) MCP-1/525, (B) TGF-/565, (C) IL-10/605, and (D) TNF-/655 QD IC detection antibodies. Scale bars are 30 μm.

20 nM was optimal for IL-10 and TNF-α and 100 nM for MCP-1 and TGF-β QD IC antibodies (Figure 3.3). Afterwards, we evaluated detection threshold for each of our protein probes following similar steps as discussed previously. Briefly, glass slides were silanized, neutravidin conjugated, and the four biotinylated capture antibodies were added. Next, purified soluble human proteins (MCP-1, TGF-β, IL-10, or TNF-α) at concentrations ranging from 1 to 100,000 fM were incubated one by one, followed by their respective QD ICs. Figure 3.4 shows representative fluorescence images at increasing protein concentrations for MCP-1 (Figure 3.4A), TGF-β (Figure 3.4B), IL-10 (Figure 3.4C), and TNF-α (Figure 3.4D) detection. From these images, we can see that

the intensity signal from the MCP-1 and TGF-β controls is lower than the background levels from the other two probes. Even though this might be the case, as we increase the concentration of the proteins, we see a similar increase in intensity for all proteins. When the mean intensity was calculated from these images, we generated the bar graph in Figure 3.5A. After subtracting the background signal from the averaged intensity signal, we get the scatter plots in Figure 3.5B. From these graphs, we can see that detection sensitivity remained consistent to previous experiments, reaching sensitivity levels below 5 fM. Specifically, MCP-1/525 QD, TGF-β/565 QD and IL-10/605 QD detection limit was around 1 fM and TNF-α at 5 fM. Detection sensitivity for TNF-α was not as high as Chapter 2, probably because the we switched the QD to a 655 nm QD.

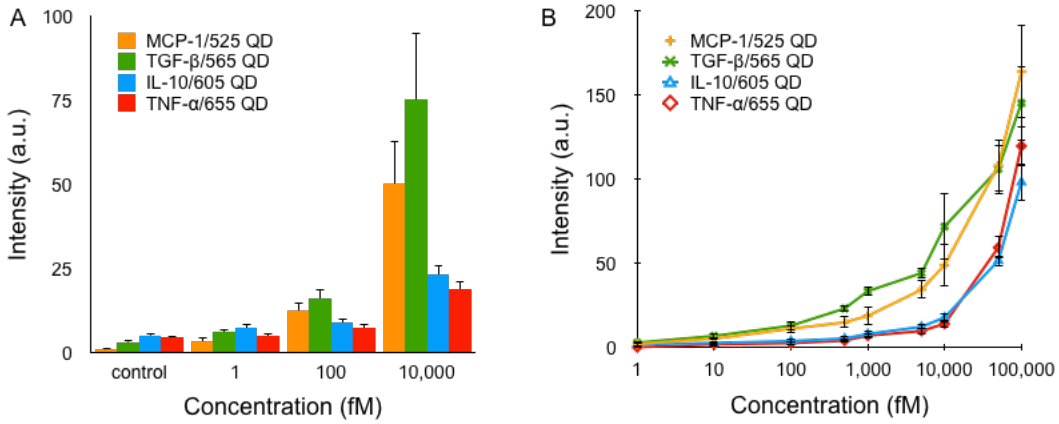

Figure 3.5. Single target detection. (A) Average intensity signal at representative protein concentrations for MCP-1/525, TGF-β/565, IL-10/605, and TNF-α/655 QD ICs. (B) Average intensity, after background subtraction, for all QD ICs. Detection thresholds were 1 fM for almost all QD ICs, with the exception of TNF-α/655 QD, which was 5 fM. Error bars represent the standard error from at least three independent experiments.

3.3.2. Evaluation of QD Fluorescence Signal in Neighboring Emission QD

Next, we evaluated if bleed-through from neighboring emission channels compromises the fluorescence signal. This phenomenon is usually seen when the

emission of one fluorophore can be detected in the filter channel of a second fluorophore, resulting in significant background signal. Even so, QD should have minimal signal crossover compared to other fluorescent probes since they have narrow emission spectra. To evaluate bleed-through, slides were silanized and neutravidin modified, four biotinylated capture antibodies were subsequently added followed by protein incubations at 1000, 10,000 and 100,000 fM. To calculate the percent (%) bleed-through of fluorescence emission, fluorescence images of the same field of view were taken with both the corresponding QD filter cube and the neighboring QD emission filter cubes; mean fluorescence intensity was calculated from the images, and the value of the mean intensity signal of the neighboring filter cube (crossover signal) over the mean intensity signal of the corresponding filter were divided to get a percentage. Figure 3.6 and Table 3.1 show the finalized results; where % bleed-through was consistently below 5% for all channels.

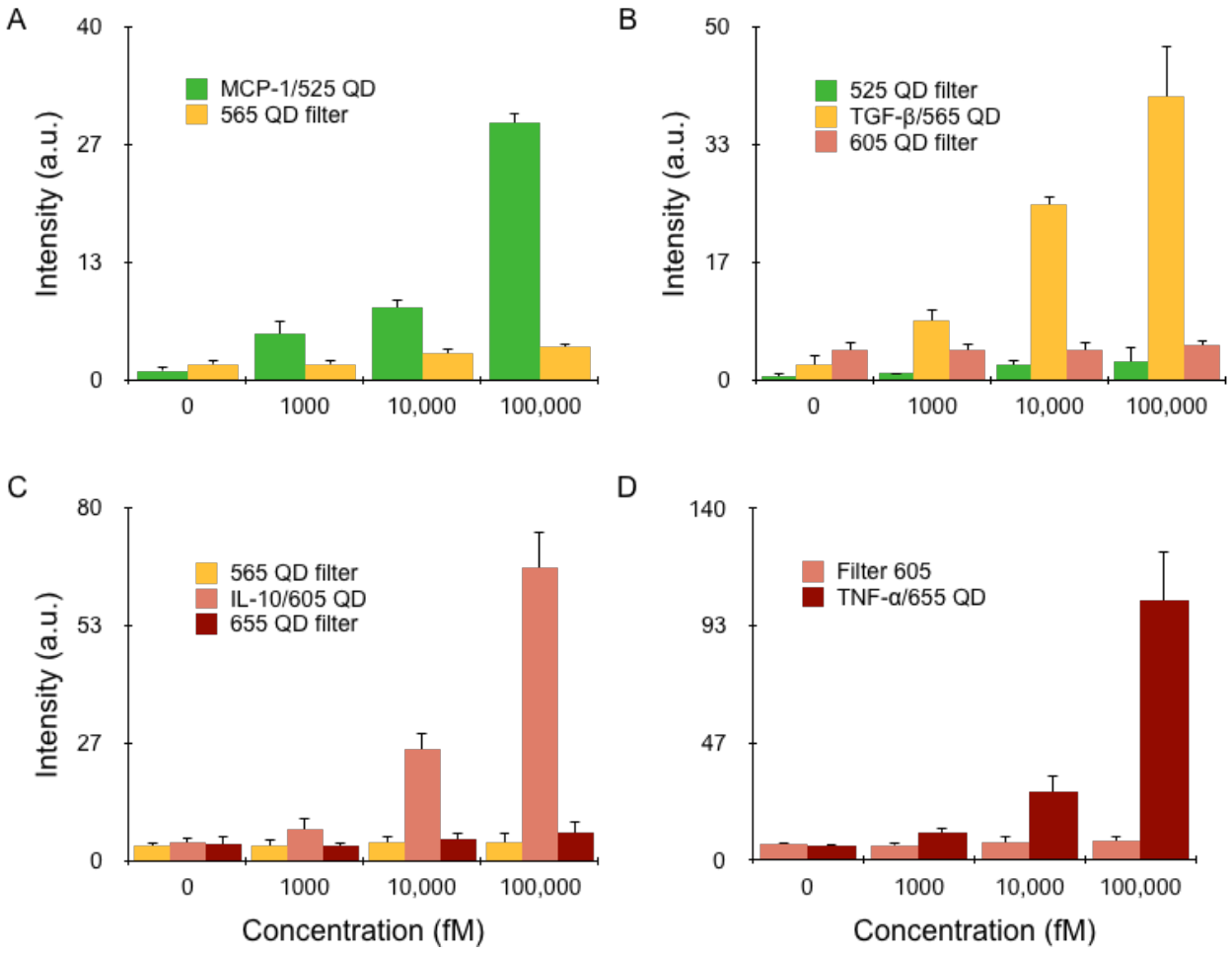

Figure 3.6. Evaluating signal bleed-though from neighboring emission channels. Bar graphs showing the intensity measurements at 1000, 10,000, and 100,000 fM protein concentrations for (A) MCP-1/525, (B) TGF-β/565, (C) IL-10/605 and (D) TNF-α/655, where the same field of view was imaged using the corresponding QD filter cube as well as the neighboring QD filter cubes.

Table 3.1. Percent bleed through (%) from neighboring QD channels. Table summarizing the % bleed through calculated for each of the QD assays.

		1000	10,000	100,000
A	565 filter	0% ± 1.4%	0.9% ± 0.7%	3.1% ± 0.6%
B	525 filter	3.7 ± 0.2%	4.7% ± 0.7%	4.5% ± 1.4%
	605 filter	0.6% ± 0.8%	0.8% ± 1.0%	2.8% ± 0.8%
C	565 filter	2.4% ± 1.5%	3.7% ± 1.6%	2.5% ± 2.2%
	655 filter	0% ± 0.9%	5.1% ± 1.3%	4.0% ± 2.6%
D	605 filter	0% ± 1.0%	5.5% ± 2.1%	1.7% ± 1.6%

Based on the above findings, we considered developing a compensation analysis to correct for fluorescence bleed-through to other channels. To do so, we used the bleed-through percentage (%) at the highest protein concentration (100,000 fM) to calculate the percentage of signal crossover at each protein concentration and subtracted this value from the mean intensity measurements. First, neighboring QD emission pairs were classified. The QD IC pairs were studied as follow, MCP-1/525 and TGF-β/565, TGF-β/565 and IL-10/605, IL-10/605 and TNF-α/655; both QD ICs in each pair were incubated at the same time. This detection was referred to as single target detection. For each single target detection, the proteins were first incubated one at a time at the desired concentration, followed by the QD IC pair. Figure 3.7 summarizes the results obtained for the TGF-β/565 and IL-10/605 QD IC pair. For these experiments, glass slides were silanized and neutravidin modified, four biotinylated capture antibodies were then incubated, followed by the proteins at concentrations ranging from 1 to 10,000 fM, and lastly the TGF-β/565 and IL-10/605 QD IC pair. The bar graph compares the intensity signal of three different protein incubation cases. First,

when only one protein, either TGF-β or IL-10, was present at different concentrations (e.g. 0 fM IL-10 and increasing concentrations of TGF-β). Second, when one protein is incubated at high protein concentration, we chose 10,000 fM, and the other one at increasing concentrations (e.g. 10,000 fM IL-10 and increasing concentrations of TGF-β). And third, the second case compensated using the above compensation analysis. The intensity signal for all three cases was within standard error to each other. This led us to conclude that calculating a

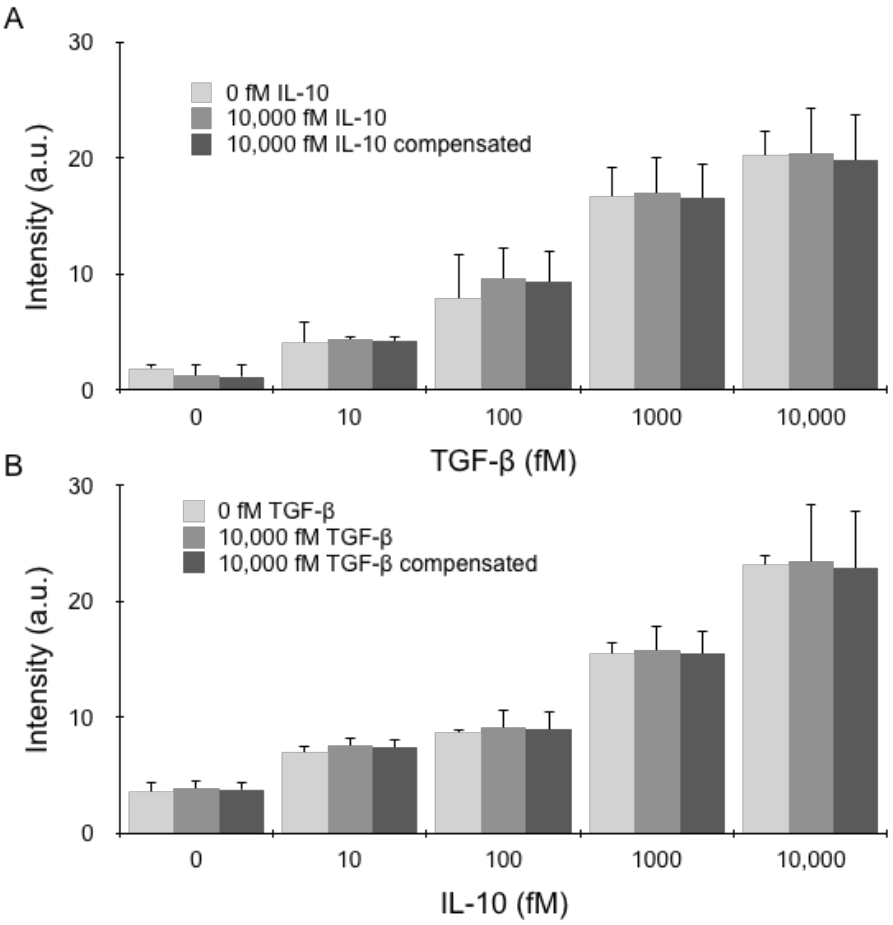

Figure 3.7. Compensation analysis to correct for fluorescence bleed-through. Percentage (%) of signal crossover in the (A) TGF-β/565 and (B) IL-10/605 QD IC pair. The bar graph compares the intensity signal of three different cases: signal detected when only one protein was present at different concentrations, signal detected when one protein is incubated at 10,000 fM and the other one at increasing concentrations, and lastly, the signal in the second case corrected using the compensation analysis. The intensity signal for all three cases was within standard error. Error bars represent the standard error from at least three independent experiments.

compensation number unique to each QD IC pair was not necessary; thus, we instead decided to compensate the intensity measurements by subtracting 5% of the total intensity signal for all neighboring channels.

Furthermore, we assessed if QD quenching, specially from neighboring emission QD, was affecting our intensity measurements. It has previously been reported that in a mixed QD size population, as is the case when we have multi-color QD, the signal from the smaller size QD can be quenched, and the signal from the larger QD can increase. (Chou, KF and Dennis, AM, Sensors, 2015). Therefore, we wanted to evaluate if quenching effects were affecting our fluorescence measurements. To do so, the intensity measurements from the single target detection where compared with the signal from the multiplexing detection. The single target detection is the incubation of one protein at a time followed by the QD IC pair (described previously). The multiplexing detection corresponds to the incubation of two soluble proteins at the same time corresponding to the QD IC pair, followed by the QD IC pair. The same three QD IC pairs used previously were tested for these experiments (MCP-1/525 and TGF-β/565, TGF-β/565 and IL-10/605, IL-10/605 and TNF-α/655). Figure 3.8 shows the mean intensity signal (background subtracted) obtained at 1000, 10,000, and 100,000 fM protein concentrations for each QD IC pair. If QD quenching was occurring in our results, the multiplexing detection intensity signal from the lower emission or smaller size QD would have been quenching when compared to the single target detection signal (Figure 3.8A, 3.8C, 3.8E). And as a consequence, the signal from the multiplexing detection from the higher emission or bigger size QD would have been enhanced when compared to the single target detection signal (Figure 3.8B, 3.8D,

3.8F). From these bar graphs, we can see that the intensity signal between single target and multiplexing detection was within standard error, suggesting that QD quenching effects were not affecting our intensity measurements from neighboring emission QD.

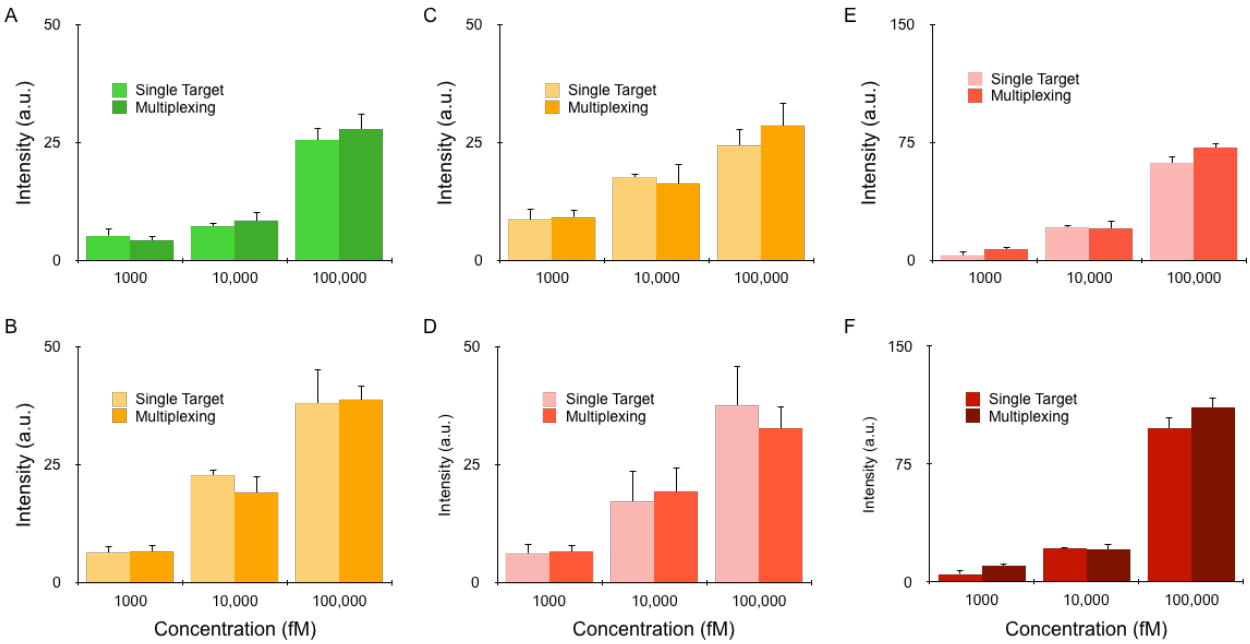

Figure 3.8. Assessing for QD quenching effects in fluorescence measurements. Bar graphs showing the mean intensity signal (background subtracted) obtained at 1000, 10,000, and 100,000 fM protein concentrations for (A,B) MCP-1/525 and TGF-β/565, (C,D) TGF-β/565 and IL-10/605, and (E, F) IL-10/605 and TNF-α/655 QD IC pairs. The single target detection refers to the incubation of only one protein at a time, whereas the multiplexing detection refers to the incubation of both proteins from the QD IC pair. The intensity measurements between these two experimental setups were compared to assess if QD quenching was occurring. The intensity signal between the single target and the multiplexing detection was within standard error for every QD IC pair; thus, we concluded that QD quenching effects were not present in our measurements. Error bars represent the standard error from at least three independent experiments.

3.3.3. Detection of MCP-1, TGF-β, IL-10, and TNF-α Secretion from Single Cells

Next, we evaluated the protein secretion from single cells using all QD IC detection antibodies. Experiments were performed by seeding PMA-differentiated U-937

cells in microarrays (900 x 90 x 43 μm), adding LPS at 100 μg/ml and/or IL-4 at 10 μg/ml and sealing the wells with the detection slide. After sealing, the microwells were first imaged under bright field to determine the number of cells per well, followed by 24 h incubation. Detection slides were then separated, stained with all four QD ICs, and imaged by fluorescence microscopy. After imaging, the collection of bright field and fluorescence images were independently stitched, superimposed to identify the well location and classified into wells containing no cells (empty) and single cells. The intensity signal for both empty and single cell wells was fist corrected by subtracting the spectral overlap (bleed-through) signal from neighboring channels. In Table 3.2, we determined each of the possible single cell secretion behaviors, where “0” stands for no protein secretion and “1” for protein secretion. For the non-stimulation case, 75% of the single cells did not secrete any of the four proteins tested, but with the addition of LPS only or LPS and IL-4, 15% more of the single cells secreted proteins. This increase in protein production from the single cells was driven by the enhanced secretion of TNF-α. The percentage of the single cells that secreted TNF-α increased from 2% to 9% with the addition of LPS. We also see an increase in both MCP-1 and TNF-α secretion from 2% to 6% with the LPS and IL-4 stimulation condition. The percentage of the single cell population that secreted only MCP-1, remained at 15% independently of the stimulation condition. For TGF-β and IL-10, we only saw a small increase in secretion from single cells by stimulating the cells with LPS and/or IL-4, from <1% to 2-3%.

Table 3.2. Single cell secretion profile. Single cell behavior as a percentage (%) of the total single cell population, defined as negative (“0”) and/or positive ("1”) secretion.

TNF-α	MCP-1	TGF-β	IL-10	Non stimulated total population (%)	LPS stimulated total population (%)	LPS & IL4 stimulated total population (%)
0	0	0	0	74.9%	59.7%	56.8%
1	0	0	0	2.2%	8.7%	8.3%
0	1	0	0	15%	15.3%	14.5%
0	0	1	0	0.2%	0.9%	1.9%
0	0	0	1	0.8%	1%	3%
1	1	0	0	1.6%	4.9%	5.5%
0	0	1	1	0.2%	0.5%	1.8%
1	0	1	0	0.2%	0.2%	0%
0	1	0	1	0%	0.6%	0.3%
1	1	1	0	0%	0.6%	0.3%
0	1	1	1	1.7%	0.1%	3.5%
1	0	1	1	0.2%	1.8%	0.3%
1	1	0	1	0%	1.5%	1.7%
1	1	1	1	3%	4.2%	2.1%
			Total	**100%**	**100%**	**100%**

Additionally, we generated histograms showing the distribution of fluorescence signal for empty (black dotted line) and single cell wells (solid colored line) in all cell stimulation condition, as can be seen in Figure 3.9. To establish a positive detection criterion, we defined the threshold limit as the fluorescence intensity that was two standard deviations above the background (empty wells) mean. Based on this, we classified single cells that were protein secretors to be those that have intensity signals above the threshold, depicted as the colored region in the histograms (Figure 3.9). Table 3.3 summarizes the percentage of total single cell population that was classified as negative or positive protein secretors based on the threshold for each protein. These percentages correspond to the colored region in the histograms on Figure 3.9. From this table, we can see an increase of positive protein secretors when cells are stimulated. At

the baseline or non-stimulated cells, about 6% of the single cell population was categorized as positive secretors for TGF-β, IL-10, and TNF-α, whereas 21% of the cells secreted MCP-1 protein. By adding LPS, or LPS and IL-4, the percentage of single cells that secreted any of the four proteins was considerably increased. MCP-1 protein secretion increased to 27% with the addition of LPS, and 31% with LPS and IL-4 stimulation. TNF-α secretion was also increased to 22% with the addition of LPS only and LPS and IL-4. For the two pro-healing proteins, LPS stimulation slightly increased the single cell secretion of TGF-β and IL-10 to 9% and 10%, respectively. By adding IL-4, a cytokine that typically favors the cell secretion of pro-healing proteins, TGF-β and IL-10 secretion was further increased to 13%. It's also important to note that the percentages in Table 3.3 are dependent on the percentages in Table 3.2. For instance, 21% of the total cell population that secreted MCP-1 protein (which is only 15% of the total cell population, according to Table 3.2) was classified as positive secretors for MCP-1. Thus, only 21% of the 15% single cell population is classified as a positive MCP-1 secretor; or in other words, only 3% of the total cell population was a positive secretor for MCP-1.

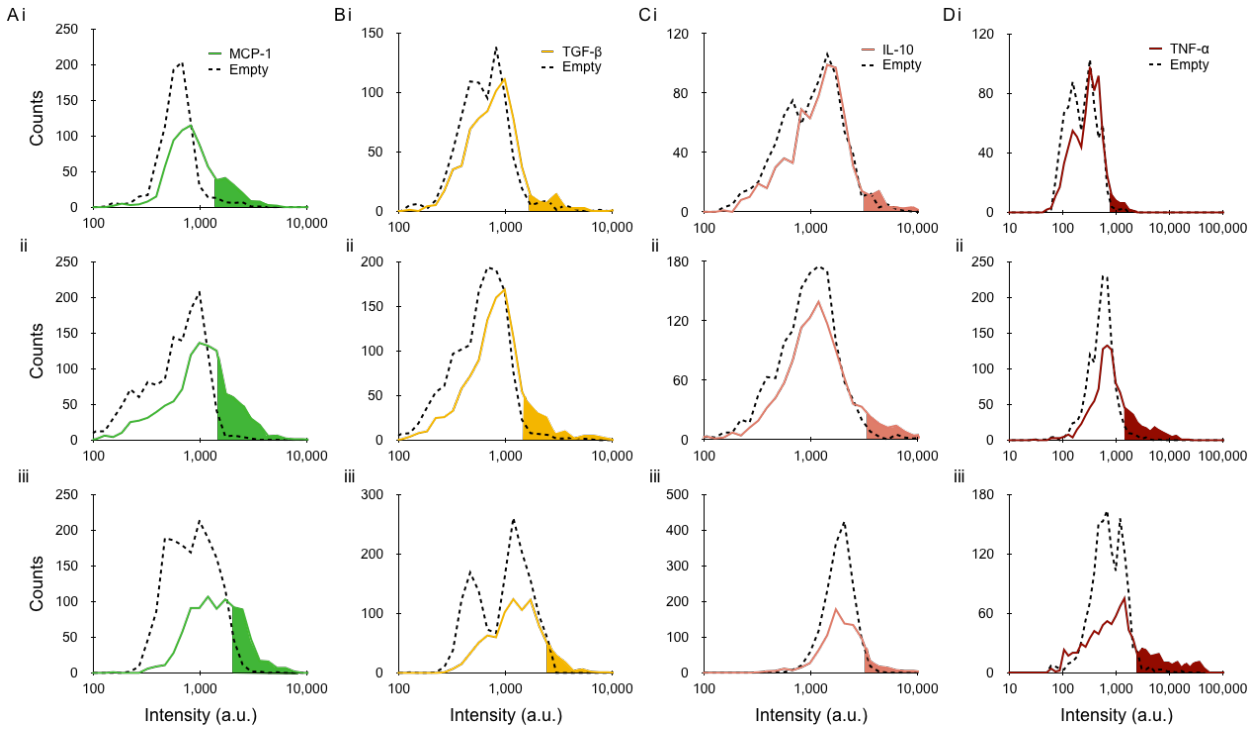

Figure 3.9. Intensity histograms from single cell experiments. Histograms showing the intensity signal distribution for U-937 cells that were either (Ai, Bi, Ci, Di) not stimulated (Aii, Bii, Cii, Dii) stimulated with LPS only, or (Aiii, Biii, Ciii, Diii) stimulated with LPS and IL4. Dotted black line is the intensity distribution from the empty wells signal, the colored line is the intensity distribution from the single cells signal, and the colored region is the intensity signal above the threshold (two standard deviations above the empty wells mean). The colored region on each histogram defines the distribution of single cells that were classified as positive protein secretors for each protein.

3.3.4. Protein Secretion Analysis from Single Cell Experiments

Lastly, we decided to test different analysis methods to explain the protein secretion dynamics from stimulated single cells. First, we decided to investigate the relationship of pro-inflammatory and pro-healing proteins secretion behavior. To do so, we plotted the intensity signal from the pro-inflammatory (MCP-1 and TNF-α) and the pro-healing (TGF-β and IL-10) proteins in two separate scatter plots (Figure 3.10). We then used the threshold limits for each protein to define a grid system that classified the intensity signal from the single cell population into four quadrants as follows, double

negative secretors on the lower left corner, positive secretor for one protein on both the upper left and lower right corners, or double positive secretors on the upper right corner. We also calculated the percentage (%) of data points within each quadrant. For the pro-inflammatory plots (Figure 3.10Ai, 3.10Bi, and 3.10Ci), MCP-1 is secreted at a similar rate for all cell stimulation conditions (17% for non-stimulation, 19% for LPS only, and 22% for LPS and IL4), whereas TNF-α increased from 3% to 10% by stimulating the single cells with LPS only and LPS and IL-4. At least half of the single cell population was double negative secretors (neither MCP-1 or TNF-α were secreted); specifically, 74% for non-stimulated, 58% for LPS only, and 55% for LPS and IL-4. The single cells classified as double positive secretors, secreting both MCP-1 and TNF-α, increased from 5% to 12-13% by stimulating the cells with LPS only and LPS and IL-4. For the pro-healing plots (Figure 3.10Aii, 3.10Bii, and 3.10Cii), most of the single cells were double negative and did not secrete neither TGF-β or IL-10 proteins;

Table 3.3. Classification of negative and positive protein secretors. Total single cell population (%) that was categorized as negative or positive protein secretors based on the threshold for MCP-1, TGF-β, IL-10, and TNF-α proteins under each cell

		Negative secretors (%)	Positive secretors (%)
MCP-1	Non stimulated	78.8%	21.2%
	LPS stimulated	72.6%	27.4%
	LPS & IL4 stimulated	69%	31%
TGF-β	Non stimulated	94.8%	5.2%
	LPS stimulated	91.3%	8.7%
	LPS & IL4 stimulated	86.8%	13.2%
IL-10	Non stimulated	93.8%	6.2%
	LPS stimulated	89.7%	10.3%
	LPS & IL4 stimulated	86.2%	13.8%
TNF-α	Non stimulated	92.4%	7.6%
	LPS stimulated	77.7%	22.3%
	LPS & IL4 stimulated	78%	22%

specifically, 93% with no stimulation, 86% with LPS only, and 76% with LPS and IL-4 stimulation. Single cell secretion of IL-10 increased from 2% to 4% by adding LPS, and to 9% with the addition of IL-4. In a similar manner, TGF-β increased from 0.7% to 3% or 6% by stimulating the cells with LPS only or LPS and IL-4. The single cells that were defined as double positive, secreting both TGF-β and IL-10, ranged from 5% to 9% depending on the stimulation condition.

Afterwards, protein concentration from positive secretors was calculated by using calibration curves and regression analysis (Figure 3.11). Two separate fittings were necessary to encompass the full protein dynamic range on the calibration curves. The lower concentration regime (<10,000 fM) was fitted using a logarithmic fit and the higher concentration range (>10,000 fM) was fitted using a linear fit. Next, histograms of positive single cell secretors after calibration were plotted on Figure 3.12. It is evident that higher protein secretion was seen when single cells were stimulated with LPS (Figure 3.11Bi, 3.11Bii, 3.11Biii, 3.11Biv) or LPS and IL-4 (Figure 3.11Ci, 3.11Cii, 3.11Ciii, 3.11Civ). Detection sensitivity, specifically protein detection below 60 pM, is one of the main benefits of our QD-based detection compared to traditional fluorophore immunoassays. Thus, we wanted to investigate the single cell behavior in the low protein secretion range (zoomed in histograms on Figure 3.11). Table 3.3 summarizes the percentage of the positive single cell secretors that secreted protein concentrations below 60 pM. For MCP-1, secretion below <60 pM remained mostly consistent at around 4%. Secretion of TGF-β in this low regime is minimal, from 0.1% for non-stimulated cells, to 1 or 4% when the cells were stimulated with either LPS or LPS and IL4. For IL-10, we see a lot of protein secretion in this low regime, especially when the

cells are stimulated; this increase in secretion is probably due to the overall higher levels of total IL-10 secretion when the cells are stimulated. In contrast, TNF-α secretion in this low regime decreases when cells are stimulated, from 31% to 10% for LPS only and 2% for LPS and IL-4. Potential explanation for this behavior could be that the cells that secreted low TNF-α levels when the cells were not stimulated, ended up secreting

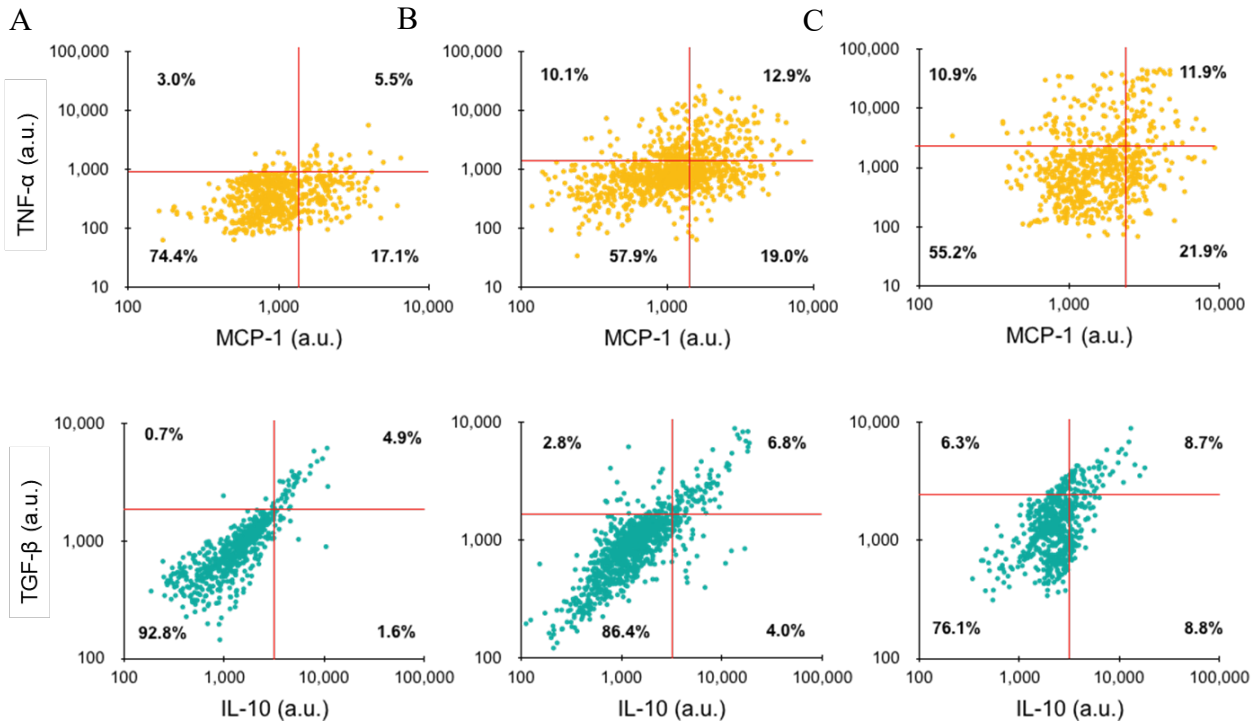

Figure 3.10. Pro-Inflammatory and pro-healing negative and positive secretors. Intensity signal was plotted as pro-inflammatory (Ai, Bi, and Ci) or pro-healing (Aii, Bii, and Cii) secreted proteins for single cells stimulated with (A) no stimulation, (B) LPS only, or (C) LPS and IL4. The cutoff between negative and positive secretors was defined as two standard deviations above the background mean (red solid lines). The four quadrants classify the single cell population as double negative (lower left corner), positive secretor for one protein (upper left and lower right corners), or double positive (upper right corner). The percentage (%) single cell signal that falls in each classification is shown in each quadrant.

higher TNF-α levels (above 60 pM); as well as the single cells that we assumed would be activated by the stimulations, did not activate in the way we expected them to. Another possible explanation could be that IL-10 and TNF-α are inversely correlated, as IL-10 secretion increases, TNF-α secretion decreases; secretion behavior that has been reported previously (Xue, et al; Sci Signal, 2017). We also quantified the percentage of positive single cell protein secretors that secreted protein levels below 60 pM for one protein and secreted the other proteins at any concentration (Table 3.5). Cells that exhibited low MCP-1 and TGF-β secretion did not secrete mostly any other proteins (0%

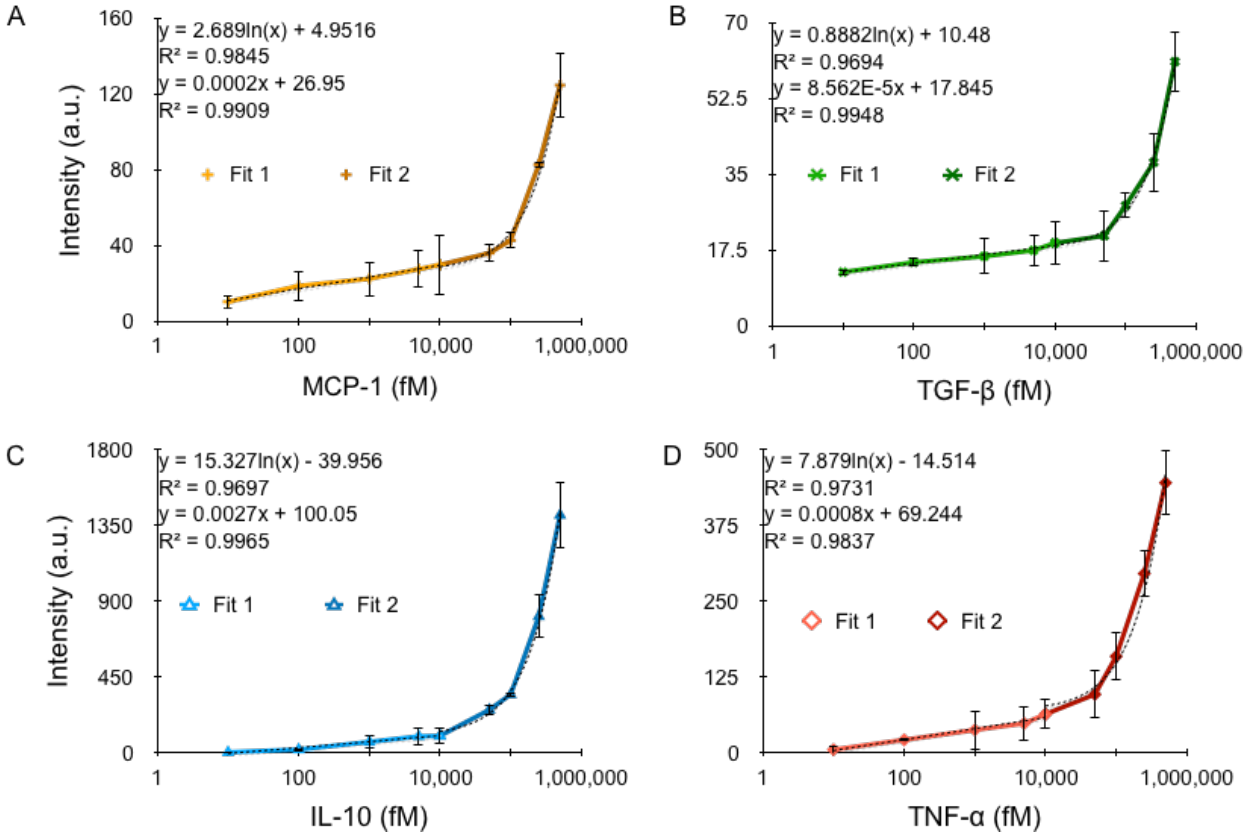

Figure 3.11. Calibrations of proteins for single cell secretion studies. Standard curves obtained for (A) MCP-1/525, (B) TGF-β/565, (C) IL-10/605, and (D) TNF-α QD ICs. The fits used to calibrate concentration in single cell secretion studies are shown in black. Two separate fittings were used to encompass the full dynamic range of the QD IC. The black dashed lines on the curves show the fits used to calibrate concentration in single cells. Error bars represent the standard error from at least three independent experiments.

– 2%), whereas single cells that secreted IL-10 below 60 pM seemed to secrete other proteins, particularly in the LPS and IL-4 condition, where 18% of the positive single cell IL-10 secretor population secreted one other protein besides low levels of IL-10.

Next, we wanted to explore the behavior of other protein secretions when single cells were negative or positive MCP-1 secretors. To do so, we generated 3D scatter plots when the single cells were either negative MCP-1 secretors (Figure 3.13Ai, 3.13Bi, 3.13Ci) or positive MCP-1 secretors (Figure 3.13Aii, 3.13Bii, 3.13Cii) for each stimulation condition, non-stimulated cells (Figure 3.13A), LPS only (Figure 3.13B), and LPS and IL-4 (Figure 3.13C). We see the same overall protein secretion distribution between negative and positive MCP-1 secretors. For the LPS stimulation, TNF-α secretion is mostly expressed at higher concentrations, especially in the positive MCP-1 secretor population (Figure 3.13Bii). TGF-β seems to also be secreted at higher concentrations when MCP-1 is positively secreted (Figure 3.13Bii), whereas IL-10 remains mostly consistent when cells are negative or positive MCP-1 secretors. For the LPS and IL-4 condition, TNF-α secretion remains mostly consistent in negative and positive MCP-1 cell secretors, but TGF-β and IL-10 secretion are expressed at higher levels when single cells secrete MCP-1 protein (Figure 3.13Cii). Overall, the correlation analysis showed a nice representation of the data, but we didn't find any interesting protein interdependence.

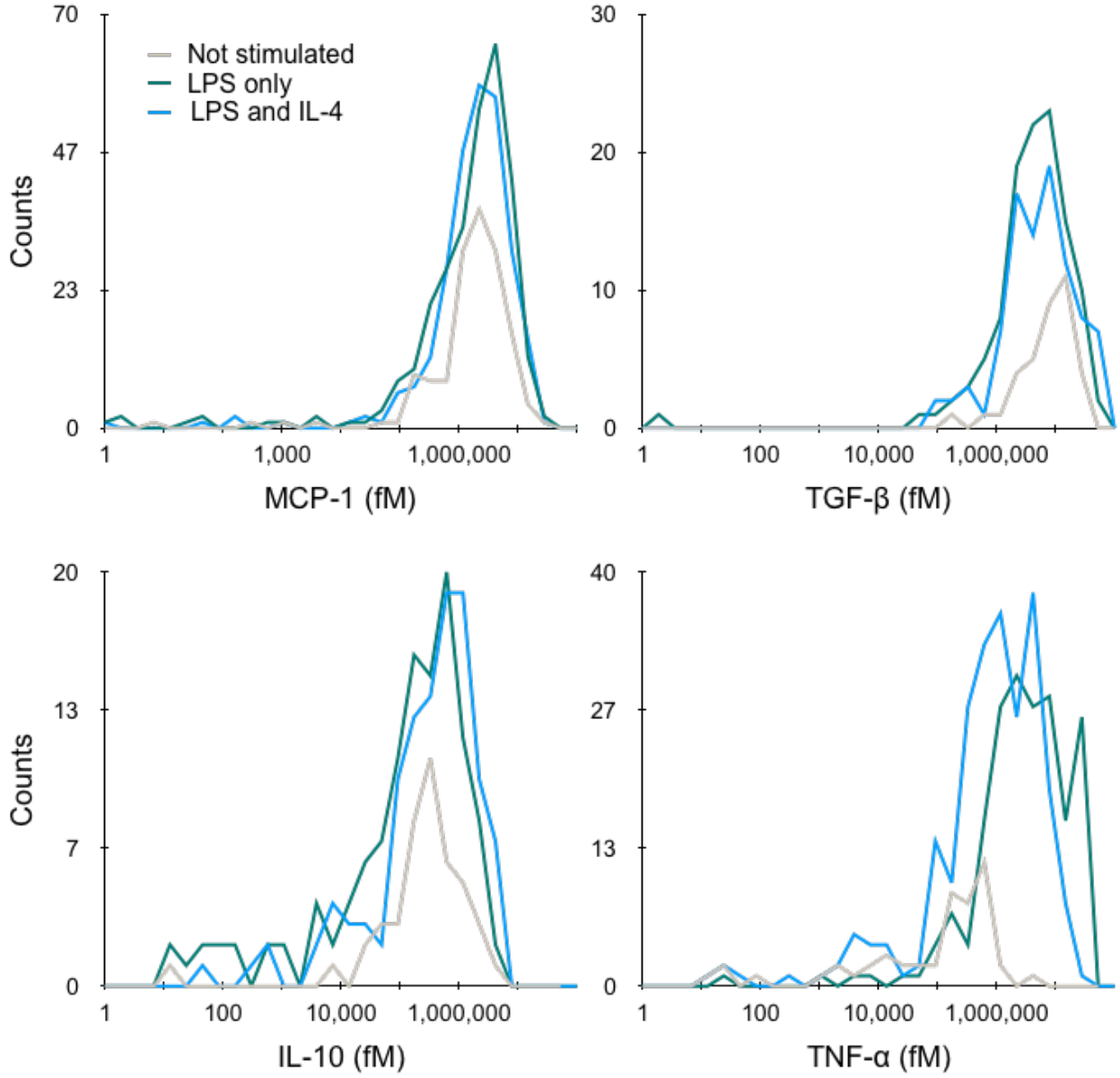

Figure 3.12. Single cell protein secretion dynamics. Histograms showing the calibrated protein distribution from not stimulated, stimulated with LPS only, and stimulated with LPS and IL4 U-937 single cells for (A) MCP-1/525, (B) TGF-β/565, (C) IL-10/605, and (D) TNF-α/655 QD assay detection.

Table 3.4. Single cell protein secretion below 60 pM. Total positive single cell secretion population (%) that secreted less than 60 pM of protein under each cell stimulation condition.

		% Total positive secretors
MCP-1	Non stimulated	4%
	LPS stimulated	4.8%
	LPS & IL4 stimulated	3.4%
TGF-β	Non stimulated	0.1%
	LPS stimulated	1.1%
	LPS & IL4 stimulated	3.5%
IL-10	Non stimulated	11.4%
	LPS stimulated	15.5%
	LPS & IL4 stimulated	25.8%
TNF-α	Non stimulated	31.4%
	LPS stimulated	10.2%
	LPS & IL4 stimulated	3.1%

Table 3.5. Single cell protein secretion behavior in the low secretion range. Percentage (%) of the total positive protein single cell secretors that secreted protein levels below 60 pM for one protein, and secreted proteins at any other concentration for the other proteins.

Secreted < 60 pM		% Total positive secretors
Low MCP-1	Non stimulated	0%
	LPS stimulated	2.4%
	LPS & IL4 stimulated	1.9%
Low TGF-β	Non stimulated	0%
	LPS stimulated	1.1%
	LPS & IL4 stimulated	2.6%
Low IL-10	Non stimulated	6.8%
	LPS stimulated	12.7%
	LPS & IL4 stimulated	17.5%
Low TNF-α	Non stimulated	25.5%
	LPS stimulated	5.1%
	LPS & IL4 stimulated	0.5%

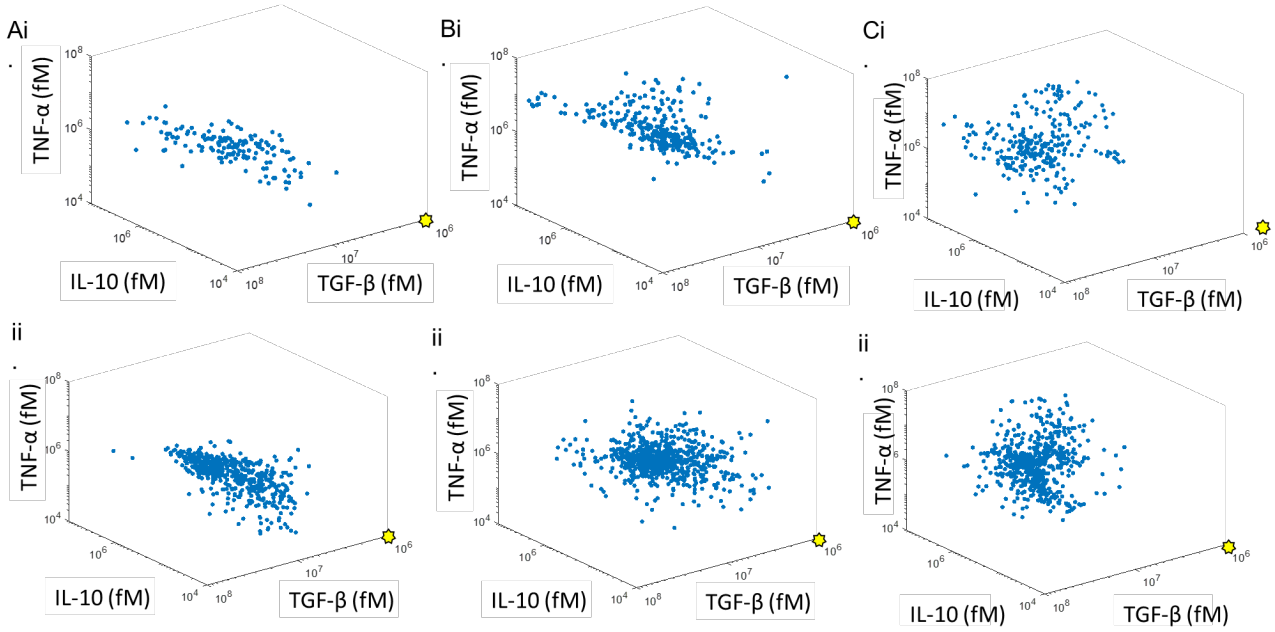

Figure 3.13. Protein secretion behavior based on MCP-1 secretion. Calibrated scatter plot showing the secretion behavior of TGF-β, IL-10, and TNF-α when MCP-1 is both negatively (Ai, Bi, and Ci) and positively (Aii, Bii, and Cii) secreted from single cells when the cells were (Ai and Aii) not stimulated, stimulated with (Bi and Bii) LPS only or (Ci and Cii) LPS and IL4. The yellow dot references the lower secretion of all protein, approaching the origin (0,0,0).

3.4 Conclusion

In this work, we developed a sensitive multiplexing single cell detection assay with a detection threshold of at least 5 fM using multi-color QD sandwich immunoassays and QD imaging. The multiplexing assay retained the sensitivity achieved in our previous work (Chapter 2), as well as maintained additional benefits such as assay speed, simplicity, and spatial resolution. Based on our results, we concluded that spectral overlap or bleed-through remained consistently below 5% across different emission channels, and that QD quenching effects did not significantly affect our intensity signals. In single cell experiments, the multiplexing QD-based detection method was able to assess the protein secretion of the four protein targets, MCP-1,

TGF-β, IL-10, and TNF-α under different microenvironmental stimuli (LPS only and LPS and IL4). We were able to distinguish between negative and positive protein secretors, as well as implement correlation analysis methods to visualize the protein secretion interdependence. Future work will focus in patterning capture antibodies onto antibody barcodes[55,56] to have a more controlled capture antibody distribution on the glass slides.

CHAPTER 4: Exploring fluorescence lifetime properties of quantum dots using fluorescence lifetime imaging microscopy

4.1 Introduction

Fluorescent quantum dots (QDs) are small semiconductor nanocrystals that possess unique luminescent properties. QDs are bright, photostable, display narrow and size-tunable emission spectra, and exhibit long fluorescence lifetimes.[90] These features make QDs ideal candidates to increase protein detection sensitivity in single cell experiments that offer multiplexing capabilities. In chapter 2, we showed that detection sensitivity for soluble proteins can significantly be improved by using QD-based detection instead of organic fluorophores. QD imaging and signal amplification through bioorthogonal chemical reaction were used to lower detection threshold down to 60 aM for TNF-α protein. Unfortunately, homoquenching effects between neighboring QDs were seen with the chemical amplification (ChemAmp) detection. The ChemAmp technique uses a two-step reaction where *trans*-cylooctene (TCO) modified detection antibody is first reacted, followed by tetrazine (Tz) modified QDs. Homoquenching effects are likely seen in this method since multiple, close-proximity QDs can bind per antibody. In previous results, we noted that the complex relationship between intensity and protein concentration using the ChemAmp detection would make it difficult to quantify secretion in single cell experiments. We also proposed solutions to resolve the issue, such as using fluorescence lifetime imaging microscopy (FLIM) to assess and correct quenching, or eliminate quenching completely by encapsulating the QDs in a protective shell. In this chapter, we explored solutions to eliminate homoquenching effects.

The phasor approach to FLIM simplifies lifetime analysis by transforming lifetime decay data into its sine and cosine components for a graphical representation of lifetime.[37,91] Each pixel in the intensity image corresponds to a specific location on the phasor plot; where long lifetimes are depicted on the left side of the phasor and shorter lifetimes on the right side (Figure 1.5, chapter 1). Single exponentials fall somewhere along the universal circle, and multi-exponentials somewhere on the inside. When a pixel has a fractional contribution of two fluorescent species, the location on the phasor would fall somewhere along the line of the location of the pure fluorescent species. This rapid, fit-free method allows for the efficient separation of fluorescent species that have the same emission wavelengths, but different lifetimes. QDs exhibit long fluorescence lifetimes, ranging from 10 to 100 nanoseconds, that can be tuned by varying the material of its core and shell, as well as the shell thickness.[92] As comparison, most organic fluorophores have lifetimes ranging from 2 to 5 nanoseconds. Due to these differences in lifetimes, multiplexed fluorescence imaging in the same emission window using the phasor approach is straightforward. Furthermore, homoquenching effects can be visualized and assessed using the phasor approach. If QD lifetime is affected in any way, its location on the phasor would also change. When QD quenching occurs, QD phasor location will move from the far left to the further right (approaching the origin (0,0)), from the long lifetime location to the shorter lifetime one (Figure 4.2). Using this information, QD homoquenching levels in the sample can be identified from the location on the phasor. Using FLIM analysis, we can also calculate the true QD concentration in the sample, independently of quenching effects.[38]

In this work, we explore the QD lifetime properties using fluorescence lifetime and the phasor approach to FLIM. First, we assessed QD signal changes, potentially quenching levels, in samples containing increasing QD concentrations. We find that QDs have two distinct locations on the phasor, one in the far left for unquenched QDs, and another in the upper right, indicating an interesting configurational change in QD lifetime behavior, potentially QD quenching effects. The location on the phasor changes depending on the fractional contribution of each QD species in the sample; when there is a mixture of both populations, the location on the phasor falls somewhere along the line of the pure species (Figure 4.1). Using this information, we were able to calculate the actual average QD concentration in the sample. By utilizing the phasor approach for FLIM, we were able to successfully compensate for changes in QD lifetime and intensity behavior.

4.2 Methods

4.2.1 Immunoconjugate (QD IC) Conjugations

Amine-terminated quantum dots emitting at 605 nm (Thermo Fisher Scientific) were modified with NHS–tetrazine (Click Chemistry Tools) as described previously in Chapter 2. Briefly, capture antibodies were modified with 5 molar equivalents of sulfo-NHS LC Biotin in PBS containing 10% dimethylformamide (DMF) and 0.1 M $NaHCO_3$ (pH 8.4). Detection antibodies were reacted with 30 molar equivalents of NHS-TCO. Both capture and detection antibodies were purified using Zeba spin desalting columns (Thermo Fisher). Antibody concentrations were determined by absorption measurement using a NanoDrop 2000 spectrophotometer. Amine-terminated quantum dots emitting at

605 nm (Thermo Fisher) were modified with NHS–tetrazine (Click Chemistry Tools) using 0.8 nmoles of amine-QD and 500 molar equivalents of NHS-tetrazine in PBS containing 5% DMF and 0.01 M $NaHCO_3$. Reaction was incubated for 3 h and tetrazine-QD were purified into PBS using an Ultra-4 centrifugal filter with 10 kDa MWCO. QD immunoconjugates (IC) were prepared by reacting 0.15 nmole tetrazine-QD with 200 µg TCO-modified detection antibody in 1 ml of PBS containing PBS+ for 3 h. QD ICs were purified using Sephacryl S-400 (GE Healthcare) gel filtration media on an AKTA Pure FPLC system (GE Healthcare). Final concentrations were determined by absorption measurements and calibration using the QD stock solution.

4.2.2 Prepare slides for FLIM

Standard 25 mm x 75 mm glass microscope slides were cleaned, silanized, and treated with activated neutravidin, as previously described[91]. Briefly, slides were cleaned using Piranha solution (3% H_2O_2 and concentrated H_2SO_4 at 1 : 2 volume ratio) for 30 min, rinsed with double deionized water H_2O (dH_2O), and dried in an oven for 1 h at 100 °C. Slides were then submerged in a solution of 4% (3-mercapto-propyl)trimethoxysilane in 100% ethanol for 1 h, rinsed with ethanol, and dried in the oven for 30 min. Silanized glass slides were stored in a desiccator until later use. The day of the experiment, a 50 microwell silicon gasket (Grace Bio-Labs) was placed onto the silanized glass slide and 5 µl of PBS containing 1 mg/ml maleimide-modified neutravidin was added to each well. After reacting for 2 h at room temperature, wells were washed with PBS+, biotinylated capture antibody (anti-TNF-α) was incubated at 10 µg/ml in PBS+ for 2 h, and wells were blocked with PBS+ for 15 min at room

temperature. Purified protein (TNF-α) was then added at concentrations ranging from 0.01 pg/ml to 125 pg/ml in PBS+ and incubated for 2 h at room temperature. Lastly, anti-TNF-α QD IC detection was incubated at a final concentration of 20 or 50 nM for 30 min at room temperature, washed with PBS+ and silicon gasket removed. Glass slides were sealed with a cover slip in 1X PBS for imaging.

4.2.3 FLIM imaging

For fluorescence and lifetime images were captured using a laser scanning confocal microscope (FV1000, Olympus) with a 60x water immersion objective lens and 20 MHz Fianium laser, at a 20.0 µs/pixel acquisition speed (For QD IC: ex. 470 nm, em. 560 - 660 nm; for silica NPs: ex. 534 nm, em. 560 – 660 nm). Fluorescence images were captured using Fluoview software. FLIM data was acquired using A320 FastFLIM FLIMbox. For each image, 50 frames were collected for FLIM analysis. Rhodamine 110 was used for calibrating the FLIM system with a known lifetime of 4 ns. The lifetime decay was then transformed into phasor space and analyzed using SimFCS software. To calculate QD concentration using the SimFCS software, lifetime characteristics of the 605 nm QD IC were measured in solution at 50 nM.

4.3 Results

4.3.1. Evaluating QD quenching using FLIM

To determine the lifetime properties of QD using FLIM and phasor analysis, glass slide experiments were performed. Glass slides were silanized and neutravidin modified, followed by reaction with biotinylated TNF-α capture antibody and purified

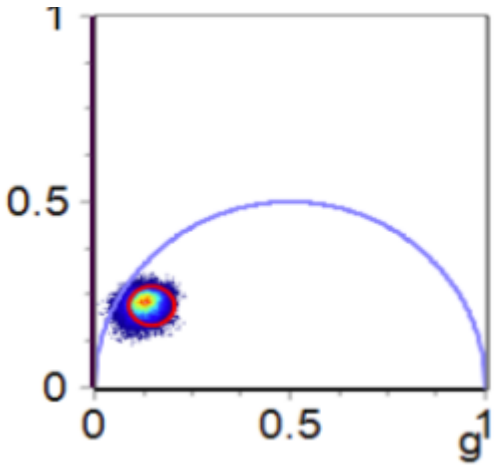

Figure 4.1. Phasor plot location of QD IC in solution.

recombinant TNF-α human protein at concentrations ranging from 0.01 to 125 pg/ml. Lastly, 20 nM or 50 nM of anti-TNF-α QD IC detection antibody was incubated. Slides were imaged using a laser scanning confocal microscope and a FastFLIM FLIMbox, using 470 nm excitation wavelength and emission collection between 560-660 nm. The images in Figure 4.2 show the phasor QD location at increasing protein concentrations. The phasor location of the control (0 pg/ml) sample shows the true QD location, which corresponds to the location of the QD IC in solution (Figure 4.1). As we increased the concentration of soluble TNF-α in our sample, we see a slow shift of the QD location on the phasor; moving from the left or long lifetime location on the phasor to the right or short lifetime position (Figure 4.2). The phasor approach to FLIM follows linear vector math; therefore, pixels on the image that contain two fluorescent species fall somewhere along the line that joins the lifetime location of the two pure species. The precise location depends on the intensity-weighted contribution of each specie. From the phasor plots in Figure 4.2, we can see that as we increase the availability of protein in the sample, the location of the phasor moves to the shorter lifetime position. This shift towards the “new” location is most likely due to the closer proximity of the neighboring QDs in the sample as we increase the protein concentration. Also, this phenomenon is slightly more dramatic when we increase the QD IC concentration from 20 nM to 50 nM;

suggesting that the shift to this new QD specie is driven by the increase of QD density in our sample.

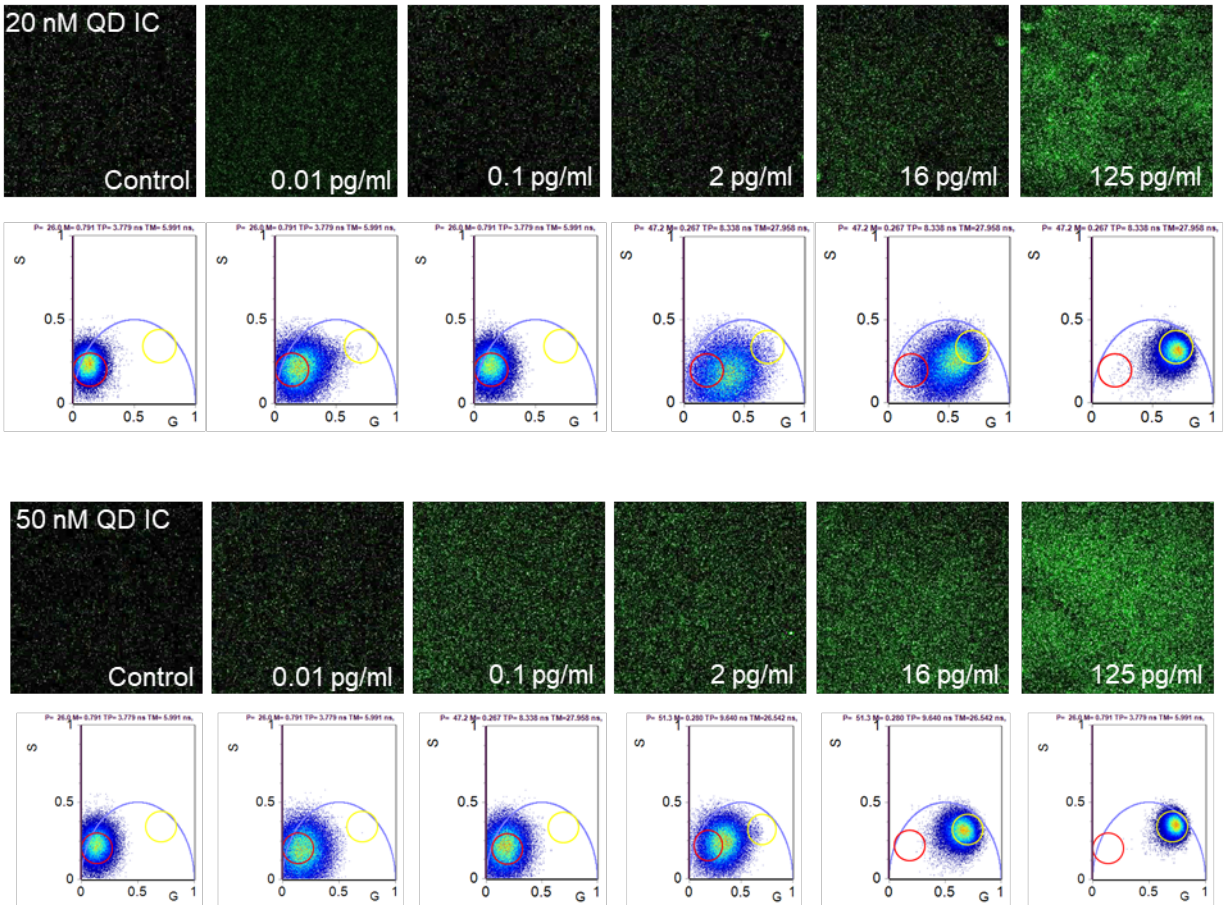

Figure 4.2. QD location on phasor plots at increasing TNF-α concentrations. Fluorescence intensity images and phasor plots for increasing TNF-α concentrations using both 20 nM (top) and 50 nM QD ICs (bottom). Intensity signal increases as protein concentration increases, and at the same time, QD phasor plot location shifts from the long lifetime region on the phasor to the shorter lifetime location. This shifts is more dramatic in the 50 nM QD IC phasors, suggesting that the increase in QD density in the sample promotes this shift.

The gradient phasor plot in Figure 4.3 (top left corner) shows the pixel fractional contribution of the pure QD position, A (red cursor) to the “new” QD position, B (yellow cursor). Pixels that contain only a single lifetime will fall somewhere along the universal circle of the phasor plot, while pixels that have a mixture of lifetimes will appear within the circle. Thus, pixels with a mixture of pure QD and “new” QD species will appear somewhere along the line of the pure QD (red cursor) and “new” QD (yellow cursor)

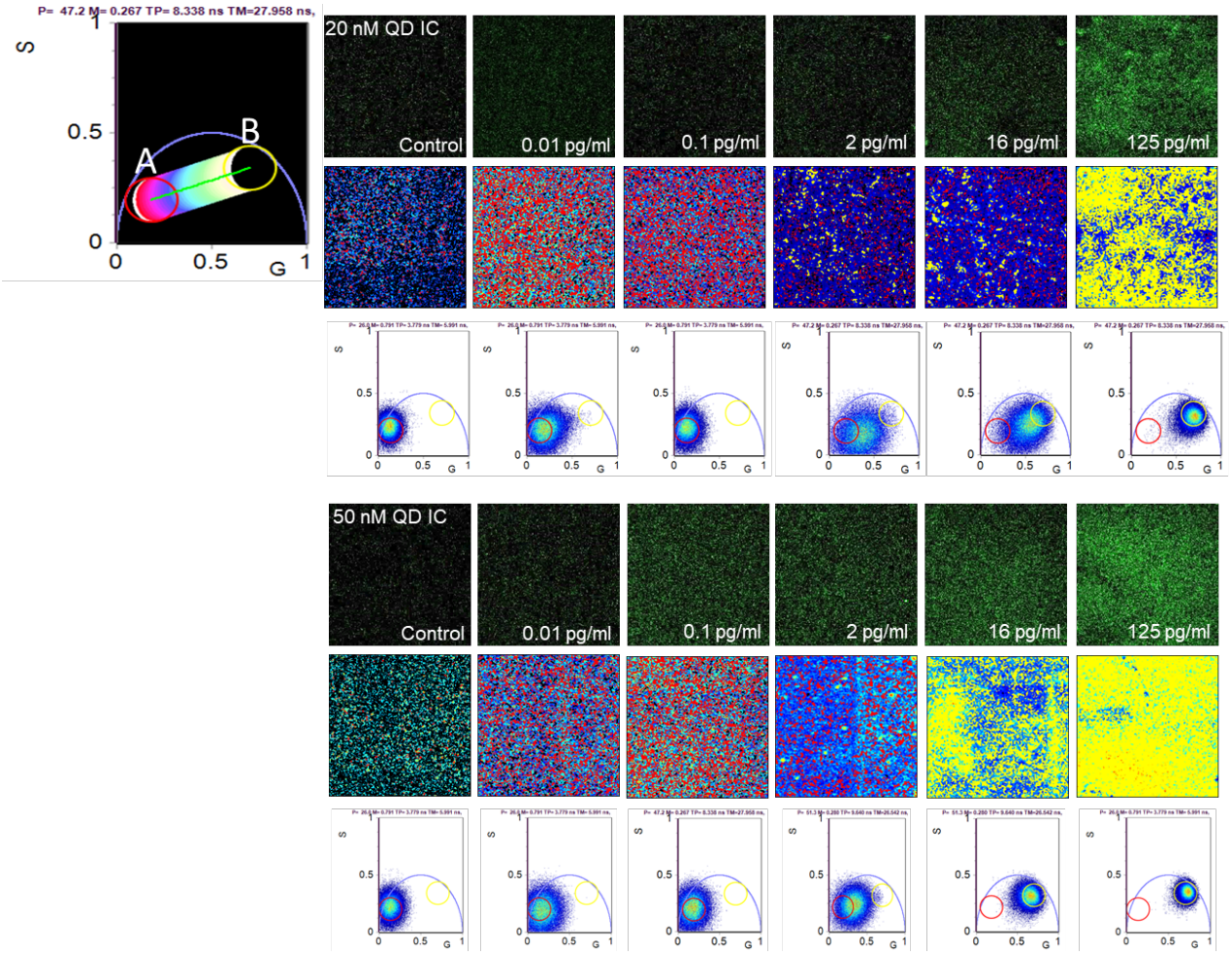

Figure 4.3. QD fraction contributions on phasor plots. Fluorescence intensity images, gradient images, and phasor plots for increasing TNF-α concentrations using both 20 nM (top) and 50 nM QD ICs (bottom). Cursors on gradient phasor plot (top left) show the pure QD location as the red cursor and the “new” QD location as the yellow cursor. As can be seen on the phasor plots, QD phasor plot location shifts from the red cursor (pure QD) to the yellow cursor (“new” QD) as the protein concentration increases in the sample.

species. The precise location along the line depends on the intensity-weighed fraction of each species present. The gradient images (Figure 4.3) show the distribution of pixels, showing first colors pertaining to the A position on the phasor, and gradually increasing to colors defining the B position. Figure 4.4 shows the quantified gradient distribution, shown as a line graph for both 20 nM and 50 nM QD ICs. Interestingly, the pixel fractional contribution of B (yellow cursor, "new" QD specie) increases as we increase the protein concentration; thus, as we increase the TNF-α concentration, we see an increase of "new" QD species.

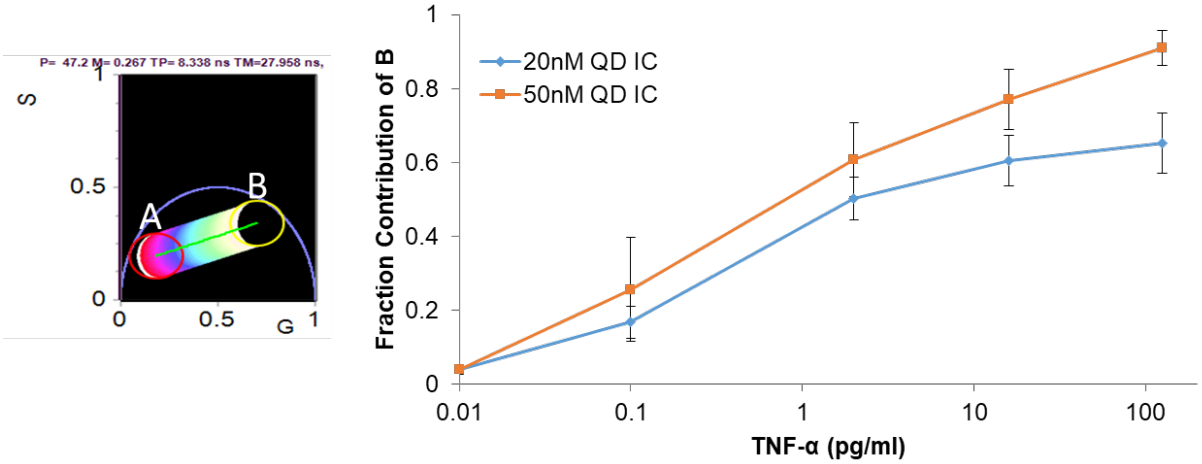

Figure 4.4. Percent fractional contribution of B ("new" QD specie). Based on the QD phasor location and the pixel distribution between cursor A (red, pure QD specie) and cursor B (yellow, "new" QD specie), we can quantify the fraction contribution of pixels located in cursor B as we increase the TNF-α concentration. Error bars represent the standard error from at least three independent experiments.

Furthermore, the concentration of each fluorescent species can also be measured if the relative brightness of the fluorescent specie is known. Therefore, the absolute QD concentration at each pixel can be calculated by using a graphical solution of the changes of the phasor location at each pixel of an image when unmodulated light is added. Using this phasor approach, the absolute concentration can be determined

with a single calibration using a solution of known QD IC concentration (Ma, N. et al, Biomedical Optics Express, 2016). When we used this feature in the SimFCS software, we calculated the absolute QD concentration shown in the line graph on Figure 4.5. As expected, the QD concentration increases as we increase the TNF-α concentration. Based on these findings, we concluded that we can compensate for the "new" QD intensity and lifetime behavior in our samples by using FLIM analytical methods.

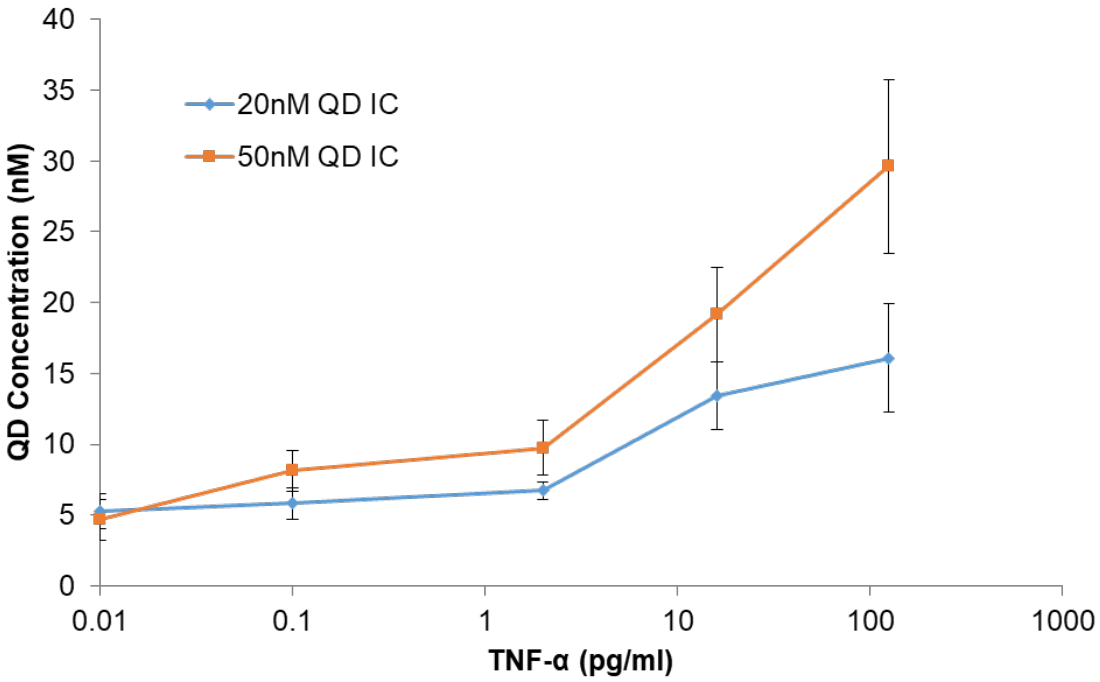

Figure 4.5. Absolute QD Concentration on each pixel. Using the fractional contribution and the intensity of the QD IC in solution, we were able to compensate for the "new" QD specie intensity and lifetime behaviors, which could be QD homoquenching effects. The scatter plot shows how QD concentration increases in the sample as protein concentration increases. This increase is slightly more pronounced for the 50 nM QD IC. Error bars represent the standard error from at least three independent experiments.

4.4 Conclusion

In this chapter, we aimed to visualize and correct unique QD effects in our immunoassays. First, we visualized QD lifetime behavior using the phasor approach to

FLIM analysis. In these phasors, the QD location on the phasor plot shifted as protein concentrations were increased, suggesting that QD can shift to this new state as the QD density increases in the sample. Based on this, we identified two distinct QD locations on the phasor, the pure QD specie situated on the long lifetime region of the phasor and the “new” QD specie located on the short lifetime location. Based on the fractional contribution of each fluorescent specie, as is the case when a pixel has a mixture of both QD populations, the QD phasor location fell somewhere along the line of the pure QD specie or “new QD specie. Using the lifetime and intensity information, actual average QD concentration in the sample was calculated, correcting for QD intensity and lifetime effects, potentially derived from QD quenching. Future work will focus on preventing QD quenching effects by encapsulation QD in silica shells. The silica shell can prevent QD quenching effects by providing a protective shell that minimizes the interaction of neighboring QDs.

CHAPTER 5: Conclusion and future directions

Single cell technologies are becoming increasingly important since understanding how individual cells process information and respond to diverse stimuli could lead to greater insight into cell heterogeneity and population behavior. One area that has received limited attention is the detection of secreted products from single cells. Secreted proteins are crucial for communicating and coordinating the cell population's response to specific biological functions. In the immune system, soluble proteins, such as cytokines, chemokines, and growth factors, are necessary for the cell-to-cell communication and cellular interaction during immune responses. In addition, macrophage activation and differentiation are regulated by distinct soluble proteins at specific protein concentrations. In order to better comprehend macrophage polarization and plasticity, single cell analysis for the identification and quantification of secreted soluble proteins from single cells must be studied further. Also, determining the type and concentration of specific secreted proteins may help explain macrophage activation and differentiation, both before and after immune responses; and furthermore, give deeper insight into macrophages role in diseased microenvironments. Current detection technologies lack spatiotemporal information and have limited multiplexing functionality. Thus, there is a need for novel nanoparticle technologies that possess sensitive and selective detection of secreted proteins from single cells that can additionally have multiplexed capabilities to detect more than one protein concurrently.

The nanoparticle detection platform proposed here tackled these unmet needs by significantly improving protein sensitivity and incorporating multiplexing capabilities. In Chapter 2, we developed QD sandwich immunoassays to enhance the detection limit

for the soluble TNF-α protein using QD imaging as well as signal amplification through bioorthogonal chemical reactions. When compared to traditional organic fluorophores with detection sensitivity of 60 pM, the QD-based method improved detection threshold by several orders of magnitude down to 60 aM and 180 aM for the chemical amplification (ChemAmp) antibody and the QD immunoconjugate (QD IC) antibody, respectively. The QD-based detection technique has the benefits of assay speed, simplicity, large dynamic range, and spatial resolution addressability; all these properties make it an ideal detection platform for detecting secreted proteins from single cells. In single cell experiments, the QD-based detection method increased the number of single cells that could be interrogated by 3-fold compared to detection using organic fluorophores; which lower detection threshold to almost 1 molecule detected per cell. The new detection sensitivity levels using the QD-based detection platform expands the applicability of the assay by enabling interrogation at earlier time points as well as lower secretion rates. Future work will focus on investigating macrophage behavior under different microenvironments, such as pro-healing and pro-inflammatory stimuli and well size, shape, and extracellular matrix. We can also adapt the technique to investigate the secretion in diseased systems, such as solid tumors. Furthermore, we will incorporate multiplexing capabilities enabling the concurrent interrogation of multiple secreted proteins. Finally, we will explore imaging techniques to assess QD quenching.

In Chapter 3, we adapted multiplexing capabilities to the QD-based detection method by using multi-color QD probes for each targeted protein. QD ICs were conjugated with uniquely color QDs for the efficient quantitation of four proteins secreted from single cells, specifically, MCP-1 (green QD, emission 525 nm), TGF-β

(yellow QD, emission 565 nm), IL-10 (orange QD, emission 605 nm), and TNF-α (red QD, emission 655 nm). Detection sensitivity for all QD immunoassays was at least 5 fM, which corresponds to detection of 1-3 molecules per cell in single cell microwells. We also explored the possibility of signal crossover (bleed-through) and QD quenching in our samples. From our experiments, we can conclude that these behaviors did not significantly affect or alter the intensity signal of the QD probes. Lastly, secreted protein behavior from differentiated U-937 single cells stimulated with either pro-healing (LPS and IL-4) or pro-inflammatory (LPS) stimuli were characterized using the four QD IC antibodies. Results showed discrete secretion profile from all four secreted proteins, with higher expression of pro-healing (TGF-β and IL-10) cytokines with pro-healing stimulation and higher expression of pro-inflammatory (MCP-1 and TNF-α) with pro-healing stimulation compared to non-stimulated single cells. Future work will focus on expanding the number of targeted secreted proteins as well as using the multi-color QD probes to also target surface cell receptors from single cells seeded in the microwells. Cell biomarker identification will help distinguish and confirm cell type and cell activation state; thus, allowing for the correlation of cell phenotype to the type and concentration of proteins secreted.

In Chapter 4, we aimed to characterize QD lifetime properties using the phasor approach to fluorescence lifetime imaging microscopy (FLIM). First, QD lifetime behavior was directly visualized on phasors, where the QD location on the phasor plot shifted as protein concentrations were increased. Based on our observations, we concluded that QD can have two distinct locations on the phasor: one in the long lifetime regime on the phasor, and another on the shorter lifetime location. Also, the

location on the phasor was dependent on the fractional contribution of these two species in the sample; when there is a mixture of both populations, the location on the phasor falls somewhere along the line of the pure QD specie or “new” QD specie (Chapter 4, Figure 4.1). Using the available lifetime and intensity information, we were able to quantify the actual average QD concentration in the sample; and as a result, we were able to compensate and correct for QD intensity and lifetime effects, which could potentially be caused by QD quenching. Future work will focus on testing more QD concentrations as well as preventing QD quenching effects altogether by encapsulation QD in silica shells.

Future work will focus on improving the QD-based detection platform by directly patterning capture antibodies onto the glass slide using a microchannel guided flow patterning technique described previously.[55,56] By doing so, we will be able to directly control the type and number of capture antibodies on each region of the glass slide, as well as monitor protein secretion from single cells in a more accurate level. We will also investigate protein secretion under different well shapes, sizes, and extracellular matrix components using the three-component system developed previously.[17] Additionally, we will focus on expanding the number of secreted proteins detected using the QD-based detection immunoassay and develop a technique to prevent QD homoquenching effects when using the ChemAmp detection antibody, to yield the lowest detection threshold possible. A potential route that could address both these goals would be to encapsulate QD in silica nanoparticles. The chemistry of silica is well characterized and widely used; silica has low toxicity, doesn’t affect fluorescence of encapsulated species, and allows for easy particle surface modifications via triethoxy silane molecules.[93,94] The silica shell

can conserve all fluorescence properties, such as lifetime, spectra, and quantum yield. Most importantly, the silica shell can prevent QD quenching effects by providing a protective shell that minimizes the interaction of neighboring QD. Besides protecting QD from quenching each other, silica nanoparticles can be used as new lifetime probes to expand the number of secreted proteins that can be detected by tuning the ratio of QD or mixing QD and fluorophore dyes in the silica nanoparticle. Furthermore, we would like to use our current detection platform to answer biologically relevant questions in healthy and diseased system; especially, the importance of autocrine and paracrine protein secretion in macrophages. In collaboration with other labs, we are currently developing a microwell-based analysis platform that allows for the efficient loading of single cells using electrode traps, assay for both cell surface and secreted protein as end-point response indicators using powerful nano-probes, and releases selected single cells of interested for detailed molecular analysis or in vitro expansion. By using this platform, we can identify and recover unique cells based on the combination of secreted and cell surface proteins. These cells can then be expanded for biotechnology applications, such as immune cell subtypes, hybrodomas, or stem cells, as well as studied further using advanced single cell methods, such as flow cytometry or single cell RNA sequencing.

Overall, this dissertation presents a novel multiplex QD-based detection platform for the sensitive detection of secreted protein from single cells to unveil cell heterogeneity secretion behavior. To achieve these goals, QD imaging and bioorthogonal Tz/TCO chemical amplification techniques were used to significantly improve detection of secreted pro-inflammatory and pro-healing proteins from single

cells using microarrays. MCP-1, TGF-β, IL-10, and TNF-α proteins were detected using multi-color QD IC detection antibodies in single cell experiments. Furthermore, the phasor approach for FLIM was employed to assess and correct for intensity and lifetime effects, which could be reflecting QD homoquenching. The future of this detection platform is extensive, since we can apply it to answer intriguing biological questions as well as couple it with other pre-processing devices, such as tissue dissociation into single cells, or post-analysis strategies, such as single cell RNA sequencing.

REFERENCES

1. Epelman, S. *et al.* Origin and functions of tissue macrophages. *Immunity* **41**, 21–35 (2014).

2. Wynn, T. A., Chawla, A. & Pollard, J. W. Macrophage biology in development, homeostasis and disease. *Nature* **496**, (2013).

3. Mantovani, A., Sozzani, S., Locati, M., Allavena, P. & Sica, A. Macrophage polarization: tumor-associated macrophages as a paradigm for polarized M2 mononuclear phagocytes. *Trends Immunol.* **23**, 549–55 (2002).

4. Murray, P. J. *et al.* Macrophage activation and polarization: nomenclature and experimental guidelines. *Immunity* **41**, 14–20 (2014).

5. Italiani, P. & Boraschi, D. From Monocytes to M1/M2 Macrophages: Phenotypical vs. Functional Differentiation. *Front. Immunol.* **5**, 514 (2014).

6. Martinez, F. O. & Gordon, S. The M1 and M2 paradigm of macrophage activation: time for reassessment. *F1000Prime Rep.* **6**, 13 (2014).

7. Herderschee, J., Fenwick, C., Pantaleo, G., Roger, T. & Calandra, T. Emerging single-cell technologies in immunology. *J. Leukoc. Biol.* **98**, 23–32 (2015).

8. Lindström, S. & Andersson-Svahn, H. *Miniaturization of biological assays - Overview on microwell devices for single-cell analyses*. *Biochimica et Biophysica Acta - General Subjects* **1810**, 308–16 (2011).

9. Wang, D. & Bodovitz, S. Single cell analysis: the new frontier in ‘omics’. *Trends Biotechnol.* **28**, 281–290 (2010).

10. Blake, W. J., KÆrn, M., Cantor, C. R. & Collins, J. J. Noise in eukaryotic gene

expression. *Nature* **422**, 633–637 (2003).

11. Elowitz, M. B., Levine, A. J., Siggia, E. D. & Swain, P. S. Stochastic Gene Expression in a Single Cell. *Science (80-.).* **297**, (2002).

12. Seder R Darrah P Roederer M, Seder, R. A., Darrah, P. A. & Roederer, M. T-cell quality in memory and protection- implications for vaccine design. *Nat. Rev. Immunol.* **8**, 247–258 (2008).

13. Proserpio, V. & Mahata, B. Single-cell technologies to study the immune system. *Immunology* (2016). doi:10.1111/imm.12553

14. Proserpio, V. & Lönnberg, T. Single-cell technologies are revolutionizing the approach to rare cells. *Immunol. Cell Biol.* **94**, 225–229 (2015).

15. Navin, N. E. The first five years of single-cell cancer genomics and beyond. *Genome Res.* **25**, 1499–1507 (2015).

16. Love, J. C., Ronan, J. L., Grotenbreg, G. M., van der Veen, A. G. & Ploegh, H. L. A microengraving method for rapid selection of single cells producing antigen-specific antibodies. *Nat. Biotechnol.* **24**, 703–707 (2006).

17. McWhorter, F. Y. *et al.* Macrophage secretion heterogeneity in engineered microenvironments revealed using a microwell platform. *Integr. Biol.* **8**, 751–760 (2016).

18. Han, Q. *et al.* Polyfunctional responses by human T cells result from sequential release of cytokines. *Proc. Natl. Acad. Sci. U. S. A.* **109**, 1607–12 (2012).

19. Yamanaka, Y. J. *et al.* Single-cell analysis of the dynamics and functional outcomes of interactions between human natural killer cells and target cells.

Integr. Biol. **4**, 1175 (2012).

20. Zhao, J. L. *et al.* Conversion of danger signals into cytokine signals by hematopoietic stem and progenitor cells for regulation of stress-induced hematopoiesis. *Cell Stem Cell* **14**, 445–459 (2014).

21. Lepone, L. *et al.* Monofunctional and polyfunctional CD8+ T cell responses to human herpesvirus 8 lytic and latency proteins. *Clin. Vaccine Immunol.* **17**, 1507–16 (2010).

22. Minchin, R. F. & Martin, D. J. Minireview: Nanoparticles for Molecular Imaging—An Overview. *Endocrinology* **151**, 474–481 (2010).

23. Nune, S. K. *et al.* Nanoparticles for biomedical imaging. *Expert Opin Drug Deliv* **6**, 1175–1194 (2009).

24. Giljohann, D. A. & Mirkin, C. A. Drivers of biodiagnostic development. *Nature* **462**, 461–464 (2009).

25. Chinen, A. B. *et al. Nanoparticle Probes for the Detection of Cancer Biomarkers, Cells, and Tissues by Fluorescence*. *Chemical Reviews* **115**, 10530–10574 (American Chemical Society, 2015).

26. Wang, D. & Bodovitz, S. *Single cell analysis: The new frontier in 'omics'*. *Trends in Biotechnology* **28**, 281–90 (2010).

27. Medintz, I. L. *et al.* Quantum dot bioconjugates for imaging, labelling and sensing. *Nat. Mater.* **4**, 435–446 (2005).

28. Stoeva, S. I., Lee, J.-S. S., Smith, J. E., Rosen, S. T. & Mirkin, C. A. Multiplexed Detection of Protein Cancer Markers with Biobarcoded Nanoparticle Probes. *J.*

Am. Chem. Soc. **128**, 8378–8379 (2006).

29. Alivisatos, A. P., Gu, W. & Larabell, C. No Title. **7**, 55–76 (2005).

30. Rahim, M. K., Kota, R., Lee, S. & Haun, J. B. *Bioorthogonal chemistries for nanomaterial conjugation and targeting*. *Nanotechnology Reviews* **2**, 215–227 (2013).

31. Haun, J. B., Devaraj, N. K., Hilderbrand, S. A., Lee, H. & Weissleder, R. Bioorthogonal chemistry amplifies nanoparticle binding and enhances the sensitivity of cell detection. *Nat. Nanotechnol.* **5**, 660–665 (2010).

32. Rahim, M. K., Kota, R. & Haun, J. B. Enhancing Reactivity for Bioorthogonal Pretargeting by Unmasking Antibody-Conjugated *trans* -Cyclooctenes. *Bioconjug. Chem.* **26**, 352–360 (2015).

33. McGlynn, S. P. Fluorescence and Phosphorescence Analysis. Principles and Applications. *J. Am. Chem. Soc.* **88**, 5688–5688 (1966).

34. Time-Domain Lifetime Measurements. in *Principles of Fluorescence Spectroscopy* 97–155 (Springer US, 2006). doi:10.1007/978-0-387-46312-4_4

35. Gratton, E. Measurements of Fluorescence Decay Time by the Frequency Domain Method. in 67–80 (Springer, Cham, 2016). doi:10.1007/4243_2016_15

36. Digman, M. A., Caiolfa, V. R., Zamai, M. & Gratton, E. The Phasor Approach to Fluorescence Lifetime Imaging Analysis. doi:10.1529/biophysj.107.120154

37. Stringari, C. *et al.* Phasor approach to fluorescence lifetime microscopy distinguishes different metabolic states of germ cells in a live tissue. *Proc. Natl. Acad. Sci.* **108**, 13582–13587 (2011).

38. Ma, N., Digman, M. A., Malacrida, L. & Gratton, E. Measurements of absolute concentrations of NADH in cells using the phasor FLIM method. *Biomed. Opt. Express* **7**, 2441–52 (2016).

39. Altschuler, S. J. & Wu, L. F. Cellular heterogeneity: do differences make a difference? *Cell* **141**, 559–63 (2010).

40. Chattopadhyay, P. K., Gierahn, T. M., Roederer, M. & Love, J. C. Single-cell technologies for monitoring immune systems. *Nat. Immunol.* **15**, 128–135 (2014).

41. Gawad, C., Koh, W. & Quake, S. R. Single-cell genome sequencing: current state of the science. *Nat. Rev Genet.* **17**, 175–188 (2016).

42. Heath, J. R., Ribas, A. & Mischel, P. S. Single-cell analysis tools for drug discovery and development. *Nat. Rev. Drug Discov.* **15**, 204–216 (2016).

43. Neu, K. E., Tang, Q., Wilson, P. C. & Khan, A. A. Single-Cell Genomics: Approaches and Utility in Immunology. *Trends Immunol.* **38**, 140–149 (2017).

44. Taniguchi, Y. *et al.* Quantifying E. coli Proteome and Transcriptome with Single-Molecule Sensitivity in Single Cells. *Science (80-.).* **329**, (2010).

45. Ramsköld, D. *et al.* Full-length mRNA-Seq from single-cell levels of RNA and individual circulating tumor cells. *Nat. Biotechnol.* **30**, 777–782 (2012).

46. Patel, A. P. *et al.* Single-cell RNA-seq highlights intratumoral heterogeneity in primary glioblastoma. *Science (80-.).* **344**, 1396–1401 (2014).

47. Lawson, D. A. *et al.* Single-cell analysis reveals a stem-cell program in human metastatic breast cancer cells. *Nature* **526**, 131–135 (2015).

48. Tirosh, I. *et al.* Dissecting the multicellular ecosystem of metastatic melanoma by

single-cell RNA-seq. *Science* **352**, 189–96 (2016).

49. Wei, W. *et al.* Single-Cell Phosphoproteomics Resolves Adaptive Signaling Dynamics and Informs Targeted Combination Therapy in Glioblastoma. *Cancer Cell* **29**, 563–573 (2016).

50. Li, H. *et al.* Reference component analysis of single-cell transcriptomes elucidates cellular heterogeneity in human colorectal tumors. *Nat. Genet.* **49**, 708–718 (2017).

51. Su, Y. *et al.* Single-cell analysis resolves the cell state transition and signaling dynamics associated with melanoma drug-induced resistance. *Proc. Natl. Acad. Sci.* **114**, 13679–13684 (2017).

52. Pilbrough, W., Munro, T. P. & Gray, P. Intraclonal Protein Expression Heterogeneity in Recombinant CHO Cells. *PLoS One* **4**, e8432 (2009).

53. Yalçın, A., Yamanaka, Y. J. & Love, J. C. Analytical Technologies for Integrated Single-Cell Analysis of Human Immune Responses. in 211–235 (Humana Press, 2012). doi:10.1007/978-1-61779-567-1_16

54. Ma, C. *et al.* A clinical microchip for evaluation of single immune cells reveals high functional heterogeneity in phenotypically similar T cells. *Nat. Med.* **17**, 738–743 (2011).

55. Lu, Y. *et al.* High-Throughput Secretomic Analysis of Single Cells to Assess Functional Cellular Heterogeneity. *Anal. Chem.* **85**, 2548–2556 (2013).

56. Lu, Y. *et al.* Highly multiplexed profiling of single-cell effector functions reveals deep functional heterogeneity in response to pathogenic ligands. *Proc. Natl.*

Acad. Sci. U. S. A. **112**, E607-15 (2015).

57. Han, Q., Bradshaw, E. M., Nilsson, B., Hafler, D. A. & Love, J. C. Multidimensional analysis of the frequencies and rates of cytokine secretion from single cells by quantitative microengraving. *Lab Chip* **10**, 1391 (2010).

58. Adalsteinsson, V. A. *et al.* Single cells from human primary colorectal tumors exhibit polyfunctional heterogeneity in secretions of ELR+ CXC chemokines. *Integr. Biol.* **5**, 1272 (2013).

59. Ma, C., Fan, R. & Elitas, M. Single Cell Functional Proteomics for Assessing Immune Response in Cancer Therapy: Technology, Methods, and Applications. *Front. Oncol.* **3**, 133 (2013).

60. Liao, M.-C. M.-C. *et al.* Single-Cell Detection of Secreted A and sAPP from Human IPSC-Derived Neurons and Astrocytes. *J. Neurosci.* **36**, 1730–1746 (2016).

61. Rissin, D. M. *et al.* Single-molecule enzyme-linked immunosorbent assay detects serum proteins at subfemtomolar concentrations. *Nat. Biotechnol.* **28**, 595–599 (2010).

62. Li, J. *et al.* Dramatic enhancement of the detection limits of bioassays via ultrafast deposition of polydopamine. *Nat. Biomed. Eng.* **1**, 0082 (2017).

63. Alivisatos, P. The use of nanocrystals in biological detection. *Nat. Biotechnol.* **22**, 47–52 (2004).

64. Anker, J. N. *et al.* Biosensing with plasmonic nanosensors. *Nat. Mater.* **7**, 442–453 (2008).

65. Haun, J. B., Yoon, T.-J., Lee, H. & Weissleder, R. Magnetic nanoparticle biosensors. *Wiley Interdiscip. Rev. Nanomedicine Nanobiotechnology* **2**, 291–304 (2010).

66. Decrop, D. *et al.* Single-Step Imprinting of Femtoliter Microwell Arrays Allows Digital Bioassays with Attomolar Limit of Detection. *ACS Appl. Mater. Interfaces* **9**, 10418–10426 (2017).

67. Nam, Jwa-Min, Thaxton, C. Shad, and Mirkin, C. A. Nanoparticle-Based Bio-Bar codes for the ultrasensitive deteciton of proteins. *Science (80-.).* **301**, 1884–1886 (2003).

68. Li, D., Wang, C., Sun, G., Senapati, S. & Chang, H. C. A shear-enhanced CNT-assembly nanosensor platform for ultra-sensitive and selective protein detection. *Biosens. Bioelectron.* **97**, 143–149 (2017).

69. Kerman, K. *et al.* Quantum dot-based immunosensor for the detection of prostate-specific antigen using fluorescence microscopy. *Talanta* **71**, 1494–1499 (2007).

70. Yan, J. *et al.* A nano- and micro- integrated protein chip based on quantum dot probes and a microfluidic network. *Nano Res.* **1**, 490–496 (2008).

71. Mukundan, H. *et al.* Optimizing a Waveguide-Based Sandwich Immunoassay for Tumor Biomarkers: Evaluating Fluorescent Labels and Functional Surfaces. *Bioconjug. Chem.* **20**, 222–230 (2009).

72. Hu, M. *et al.* Ultrasensitive, Multiplexed Detection of Cancer Biomarkers Directly in Serum by Using a Quantum Dot-Based Microfluidic Protein Chip. *ACS Nano* **4**, 488–494 (2010).

73. Dahan, M. *et al.* Diffusion Dynamics of Glycine Receptors Revealed by Single-Quantum Dot Tracking. *Science (80-.).* **302**, 442–445 (2003).

74. Pinaud, F., Clarke, S., Sittner, A. & Dahan, M. Probing cellular events, one quantum dot at a time. *Nat. Methods* **7**, 275–285 (2010).

75. Haun, J. B., Devaraj, N. K., Marinelli, B. S., Lee, H. & Weissleder, R. Probing Intracellular Biomarkers and Mediators of Cell Activation Using Nanosensors and Bioorthogonal Chemistry. *ACS Nano* **5**, 3204–3213 (2011).

76. Haun, J. B. *et al.* Micro-NMR for Rapid Molecular Analysis of Human Tumor Samples. *Sci. Transl. Med.* **3**, 71ra16-71ra16 (2011).

77. Corti, A., Fassina, G., Marcucci, F., Barbanti, E. & Cassani, G. Oligomeric tumour necrosis factor alpha slowly converts into inactive forms at bioactive levels. *Biochem. J.* **284 (Pt 3)**, 905–10 (1992).

78. Patil, S. *et al.* Single-cell analysis shows that paracrine signaling by first responder cells shapes the interferon-β response to viral infection. *Sci. Signal.* **8**, ra16 (2015).

79. Xue, Q. *et al.* Analysis of single-cell cytokine secretion reveals a role for paracrine signaling in coordinating macrophage responses to TLR4 stimulation HHS Public Access. (2017). doi:10.1126/scisignal.aaa2155

80. Niepel, M., Spencer, S. L. & Sorger, P. K. Non-genetic cell-to-cell variability and the consequences for pharmacology. *Curr. Opin. Chem. Biol.* **13**, 556–561 (2009).

81. Zullo, J., Matsumoto, K., Xavier, S., Ratliff, B. & Goligorsky, M. S. The cell secretome, a mediator of cell-to-cell communication. *Prostaglandins Other Lipid*

Mediat. **120**, 17–20 (2015).

82. Karulin, A. Y., Megyesi, Z., Caspell, R., Hanson, J. & Lehmann, P. V. Multiplexing T- and B-Cell FLUOROSPOT Assays: Experimental Validation of the Multi-Color ImmunoSpot® Software Based on Center of Mass Distance Algorithm. in 95–113 (2018). doi:10.1007/978-1-4939-8567-8_9

83. Darrah, P. A. *et al.* Multifunctional TH1 cells define a correlate of vaccine-mediated protection against Leishmania major. *Nat. Med.* **13**, 843–850 (2007).

84. Zhu, H. *et al.* Detecting Cytokine Release from Single T-cells. *Anal. Chem.* **81**, 8150–8156 (2009).

85. Sasuga, Y. *et al.* Single-Cell Chemical Lysis Method for Analyses of Intracellular Molecules Using an Array of Picoliter-Scale Microwells. *Anal. Chem.* **80**, 9141–9149 (2008).

86. Rowat, A. C., Bird, J. C., Agresti, J. J., Rando, O. J. & Weitz, D. A. Tracking lineages of single cells in lines using a microfluidic device. *Proc. Natl. Acad. Sci.* **106**, 18149–18154 (2009).

87. Resch-Genger, U., Grabolle, M., Cavaliere-Jaricot, S., Nitschke, R. & Nann, T. Quantum dots versus organic dyes as fluorescent labels. *Nat. Methods* **5**, 763–775 (2008).

88. Lee-Montiel, F. T., Li, P. & Imoukhuede, P. I. Quantum dot multiplexing for the profiling of cellular receptors. *Nanoscale* **7**, 18504–18514 (2015).

89. Herrera, V. *et al.* Pushing the limits of detection for proteins secreted from single cells using quantum dots. *Analyst* **144**, 980–989 (2019).

90. Chou, K. & Dennis, A. Förster Resonance Energy Transfer between Quantum Dot Donors and Quantum Dot Acceptors. *Sensors* **15**, 13288–13325 (2015).

91. Digman, M. A., Caiolfa, V. R., Zamai, M. & Gratton, E. The Phasor Approach to Fluorescence Lifetime Imaging Analysis. *Biophys. J.* **94**, L14–L16 (2008).

92. Hemdana, I., Mahdouani, M. & Bourguiga, R. Investigation of the radiative lifetime in core–shell CdSe/ZnS and CdSe/ZnSe quantum dots. *Phys. B Condens. Matter* **407**, 3313–3319 (2012).

93. Bruchez, M., Moronne, M., Gin, P., Weiss, S. & Alivisatos, A. P. Semiconductor nanocrystals as fluorescent biological labels. *Science* **281**, 2013–6 (1998).

94. Mehmood, A., Ghafar, H., Yaqoob, S., Gohar, U. F. & Ahmad, B. Mesoporous Silica Nanoparticles: A Review. *J. Dev. Drugs* **06**, (2017).